

## **General Disclaimer**

### **One or more of the Following Statements may affect this Document**

- This document has been reproduced from the best copy furnished by the organizational source. It is being released in the interest of making available as much information as possible.
- This document may contain data, which exceeds the sheet parameters. It was furnished in this condition by the organizational source and is the best copy available.
- This document may contain tone-on-tone or color graphs, charts and/or pictures, which have been reproduced in black and white.
- This document is paginated as submitted by the original source.
- Portions of this document are not fully legible due to the historical nature of some of the material. However, it is the best reproduction available from the original submission.

# ANALYSIS OF CRACK PROPAGATION AS AN ENERGY ABSORPTION MECHANISM IN METAL MATRIX COMPOSITES



Donald F. Adams  
Daniel P. Murphy

February 1981

TECHNICAL REPORT  
NASA-Lewis Research Center  
Grant No. NSG-3217

Approved for Public Release: Distribution Unlimited

(NASA-CR-165051) ANALYSIS OF CRACK  
PROPAGATION AS AN ENERGY ABSORPTION  
MECHANISM IN METAL MATRIX COMPOSITES  
Interim Report, Sep. 1979 - Dec. 1980  
(Wyoming Univ.) 159 p HC A08/MF A01

N82-14288

Unclass  
G3/24 42059

**COMPOSITE MATERIALS RESEARCH GROUP**  
**DEPARTMENT of MECHANICAL ENGINEERING**  
**University of Wyoming** **Laramie, Wyoming 82071**

ANALYSIS OF CRACK PROPAGATION AS AN ENERGY  
ABSORPTION MECHANISM IN METAL MATRIX COMPOSITES

DONALD F. ADAMS  
DANIEL P. MURPHY

FEBRUARY 1981

ANNUAL TECHNICAL REPORT  
NASA-LEWIS RESEARCH CENTER  
GRANT NO. NSG-3217

COMPOSITE MATERIALS RESEARCH GROUP  
MECHANICAL ENGINEERING DEPARTMENT  
UNIVERSITY OF WYOMING  
LARAMIE, WYOMING 82071

APPROVED FOR PUBLIC RELEASE: DISTRIBUTION UNLIMITED

1 Report No		2 Government Accession No		3 Recipient's Catalog No	
4 Title and Subtitle  Analysis of Crack Propagation as an Energy Absorption Mechanism in Metal Matrix Composites				5 Report Date <b>February 1981</b>	
				6 Performing Organization Code	
7 Author(s)  Donald F. Adams and Daniel P. Murphy				8 Performing Organization Report No  UWME-DR-101-102-1	
9 Performing Organization Name and Address  Composite Materials Research Group Mechanical Engineering Department University of Wyoming, Laramie, Wyoming 82071				10 Work Unit No	
				11 Contract or Grant No  NSG-3217	
12 Sponsoring Agency Name and Address  NASA-Lewis Research Center 21000 Brookpark Road Cleveland, Ohio 44135				13 Type of Report and Period Covered  Interim Report Sept. 1979-Dec. 1980	
				14 Sponsoring Agency Code	
15 Supplementary Notes  Program Monitor: Dr. J. A. DiCarlo Materials Science Branch					
16 Abstract  During this second-year effort, emphasis has been on the completion of the crack initiation and crack propagation addition to the previously developed generalized plane strain, finite element micromechanics analysis. Also, a new axisymmetric analysis has been developed, which contains all of the general features of the plane analysis, including elastoplastic material behavior, temperature-dependent material properties, and crack propagation.  These analyses have been used to generate various example problems demonstrating the inelastic response of, and crack initiation and propagation in, a boron/aluminum composite.					
17 Key Words (Suggested by Author(s))  Boron/Aluminum Composites Metal Matrix Composites Micromechanics Analysis Energy Absorption Crack Propagation				18 Distribution Statement  Unclassified, Unlimited	
19 Security Classif (of this report)  Unclassified		20 Security Classif (of this page)  Unclassified		21 No. of Pages  143	
				22 Price*	

For sale by the National Technical Information Service, Springfield, Virginia 22161



## PREFACE

This Annual Technical Report presents research performed during the second year of NASA-Lewis Grant NSG-3217. The NASA-Lewis Technical Monitor since the inception of this grant has been Dr. J.A. DiCarlo of the Materials Science Branch.

This study is being performed within the Composite Materials Research Group at the University of Wyoming. The Principal Investigator is Dr. Donald F. Adams, Professor of Mechanical Engineering. Mr. Daniel P. Murphy, former graduate student in Mechanical Engineering, performed the work contained herein, as a M.S. thesis under the direction of the Principal Investigator.

The contributions of Mr. David A. Crane and Mr. Brent G. Schaffer, graduate students in Mechanical Engineering, are also gratefully acknowledged.

## TABLE OF CONTENTS

Section	Page
1. Introduction . . . . .	1
2. Summary. . . . .	3
3. Generalized Plane Strain Analysis Method . . . . .	5
4. Axisymmetric Analysis Method . . . . .	9
4.1. Purpose of the Axisymmetric Formulation . . . . .	9
4.2. The Axisymmetric Finite Element. . . . .	12
4.2.1. Basic Axisymmetric Relationships . . . . .	12
4.2.2. Approximate Axisymmetric Element Stiffness Formulation .	15
4.2.3. Exact Axisymmetric Element Formulation . . . . .	19
4.2.3.1. Strain - Displacement Relationships. . . . .	19
5. Material Properties. . . . .	33
6. Numerical Results. . . . .	35
6.1. Generalized Plane Strain Analysis Models . . . . .	36
6.1.1. Development of the Broken Fiber, Longitudinal Section Models . . . . .	36
6.1.2. Development of the Transverse Section Models . . . . .	45
6.2. Axisymmetric Analysis Models . . . . .	45
6.3. Axial Loading of Longitudinal Models With 33 Percent Discontinuous Fibers . . . . .	49
6.3.1. Crack Initiation and Propagation in the 45° Section Longitudinal Model . . . . .	49
6.3.2. Crack Initiation and Propagation in the 90° Section Longitudinal Model . . . . .	54
6.4. Axial Loading of Longitudinal Models with 12.5 Percent Discontinuous Fibers . . . . .	59
6.4.1. Crack Initiation and Propagation in the 45° Section Longitudinal Model . . . . .	59

## TABLE OF CONTENTS (continued)

Section	Page
6.4.2. Crack Initiation and Propagation in the 90° Section Longitudinal Model . . . . .	83
6.5. Crack Initiation and Propagation in the Transverse Section Model, Loaded Transversely . . . . .	104
6.6. Axial Loading of the Axisymmetric Longitudinal Model . . .	112
7. Conclusions and Future Work. . . . .	124
References . . . . .	127
Appendices . . . . .	129
A. Evaluation of Integral Coefficients for the Generalized Axisymmetric Element Stiffness Matrix . . . . .	129
B. Numerical Difficulties with Special Geometrical Configura- tions of the Axisymmetric Element. . . . .	134
B.1. One Node Point Radius Equal to Zero . . . . .	134
B.2. Two Node Point Radii Equal but Nonzero . . . . .	135
B.3. Two Node Point Radii Equal to Zero . . . . .	135
C. Load Application in the Displacement Formulation of the Finite Element Analysis. . . . .	140

## LIST OF FIGURES

Figures	Page
1. Region of Interest for the Axisymmetric Analysis . . . . .	11
2. Solid Axisymmetric Triangular Element, Polar Coordinates . . .	13
3. Finite Element i in the r-z Plane . . . . .	15
4. Typical Full Range Stress-Strain Curve for 6061-T6 Aluminum Alloy at Room Temperature [14] . . . . .	34
5. Cross Section of a Square Array of Fibers, 55 Percent Fiber by Volume. . . . .	37
6. 45° Section Longitudinal Model with 33.3 Percent Discontinuous Fibers . . . . .	38
7. Finite Element Representation of the Local Region Around the Broken Fiber End in Figure 6 . . . . .	40
8. 90° Section Longitudinal Model with 33.3 Percent Discontinuous Fibers . . . . .	41
9. Refined 45° Section Longitudinal Model with 12.5 Percent Discontinuous Fibers, 8.2 Fiber Diameters in Length. . . . .	43
10. Refined 90° Section Longitudinal Model with 12.5 Percent Discontinuous Fibers, 8.2 Fiber Diameters in Length. . . . .	44
11. Transverse Section Finite Element Model of a Square Array of Unflawed Fibers, 55 Percent Fiber by Volume. . . . .	46
12. Transverse Section Finite Element Model of a Repeating Square Array of Four Fibers, 55 Percent Fiber by Volume . . . . .	47
13. Axisymmetric Finite Element Model Representation of the Maximum Fiber Spacing in a 55 Percent Fiber Volume, Square Array, Unidirectional Composite ( $r_f/r_m = 0.424$ ). Model Length is 5.5 Fiber Diameters. . . . .	48
14. Extent of Crack Growth and Plastic Deformation at an Average Applied Stress of 107.2 ksi, 45° Section Longitudinal Model. Crack Initiation Occurred at 64.1 ksi. . . . .	51
15. Plot of Applied Stress versus Composite Strain for the 45° Section Longitudinal Model, 33.3 Percent Discontinuous Fibers . . . . .	53

# LIST OF FIGURES (continued)

Figures	Page
16. Extent of Crack Growth and Plastic Deformation at an Average Applied Stress of $\bar{\sigma}_x = 84.0$ ksi, 90° Section Longitudinal Model. Crack Initiation Occurred at $\bar{\sigma}_x = 37.1$ ksi. . . . .	55
17. Subsequent Crack Growth and Plastic Deformation at an Average Applied Stress of $\bar{\sigma}_x = 94$ ksi, 90° Section Longitudinal Model . . . . .	57
18. Plot of Applied Stress versus Composite Strain for the 90° Section Longitudinal Model, 33.3 Percent Discontinuous Fibers. . . . .	53
19. Contours of Constant Octahedral Shear Stress, Normalized by Dividing by the Matrix Yield Value of 17 ksi. Average Applied Stress, $\bar{\sigma}_x = 75.1$ ksi. 45° Section Longitudinal Model . . . . .	60
20. Contours of Constant Octahedral Shear Strain ( $10^{-3}$ in/in), Average Applied Stress, $\bar{\sigma}_x = 75.1$ ksi, 45° Section Longitudinal Model . . . . .	61
21. Contours of Constant Maximum Principal Stress (ksi), Average Applied Stress, $\bar{\sigma}_x = 75.1$ ksi, 45° Section Longitudinal Model . . . . .	62
22. Contours of Constant In-Plane Shear Stress (ksi), Average Applied Stress, $\bar{\sigma}_x = 75.1$ ksi, 45° Section Longitudinal Model . . . . .	63
23. Fiber Loadings versus Distance from Plane of Fiber Break, Average Applied Stress, $\bar{\sigma}_x = 75.1$ ksi, 45° Section Longitudinal Model . . . . .	65
24. Contours of Constant Octahedral Shear Stress, Normalized by Dividing by the Matrix Yield Value of 17 ksi. Average Applied Stress, $\bar{\sigma}_x = 76.0$ ksi, 45° Section Longitudinal Model . . . . .	66
25. Contours of Constant Octahedral Shear Strain ( $10^{-3}$ in/in), Average Applied Stress, $\bar{\sigma}_x = 76.0$ ksi, 45° Section Longitudinal Model . . . . .	67
26. Contours of Constant Maximum Principal Stress (ksi), Average Applied Stress, $\bar{\sigma}_x = 76.0$ ksi, 45° Section Longitudinal Model . . . . .	68

# LIST OF FIGURES (continued)

Figures	Page
27. Contours of Constant In-Plane Shear Stress (ksi), Average Applied Stress, $\bar{\sigma}_x = 76.0$ ksi, 45° Section Longitudinal Model . . . . .	69
28. Fiber Loadings versus Distance from Plane of Fiber Break, Average Applied Stress, $\bar{\sigma}_x = 76.0$ ksi, 45° Section Longitudinal Model . . . . .	70
29. Contours of Constant Octahedral Shear Stress, Normalized by Dividing by the Matrix Yield Value of 17 ksi. Average Applied Stress, $\bar{\sigma}_x = 97.4$ ksi, 45° Section Longitudinal Model . . . . .	72
30. Contours of Constant Octahedral Shear Strain ( $10^{-3}$ in/in), Average Applied Stress, $\bar{\sigma}_x = 97.4$ ksi, 45° Section Longitudinal Model . . . . .	73
31. Contours of Constant Maximum Principal Stress (ksi), Average Applied Stress, $\bar{\sigma}_x = 97.4$ ksi, 45° Section Longitudinal Model . . . . .	74
32. Contours of Constant In-Plane Shear Stress (ksi), Average Applied Stress, $\bar{\sigma}_x = 97.4$ ksi, 45° Section Longitudinal Model . . . . .	75
33. Fiber Loadings versus Distance from Plane of Fiber Break, Average Applied Stress, $\bar{\sigma}_x = 97.4$ ksi, 45° Section Longitudinal Model . . . . .	76
34. Contours of Constant Octahedral Shear Stress, Normalized by Dividing by the Matrix Yield Value of 17 ksi, Average Applied Stress, $\bar{\sigma}_x = 183$ ksi, 45° Section Longitudinal Model . . . . .	77
35. Contours of Constant Octahedral Shear Strain ( $10^{-3}$ in/in), Average Applied Stress, $\bar{\sigma}_x = 183$ ksi, 45° Section Longitudinal Model . . . . .	78
36. Contours of Constant Maximum Principal Stress (ksi), Average Applied Stress, $\bar{\sigma}_x = 183$ ksi, 45° Section Longitudinal Model . . . . .	79
37. Contours of Constant In-Plane Shear Stress (ksi), Average Applied Stress, $\bar{\sigma}_x = 183$ ksi, 45° Section Longitudinal Model . . . . .	80
38. Fiber Loadings versus Distance from Plane of Fiber Break, Average Applied Stress, $\bar{\sigma}_x = 183$ ksi, 45° Section Longitudinal Model . . . . .	81

# LIST OF FIGURES (continued)

Figures	Page
39. Plot of Applied Stress versus Composite Strain for the 45° Section Longitudinal Model, 12.5 Percent Discontinuous Fibers . . . . .	82
40. Contours of Constant Octahedral Shear Stress, Normalized by Dividing by the Matrix Yield Value of 17 ksi, Average Applied Stress, $\bar{\sigma}_x = 24.9$ ksi, 90° Section Longitudinal Model . . . .	85
41. Contours of Constant Octahedral Shear Strain ( $10^{-3}$ in/in), Average Applied Stress, $\bar{\sigma}_x = 24.9$ ksi, 90° Section Longitudinal Model . . . . .	86
42. Contours of Constant Maximum Principal Stress (ksi), Average Applied Stress, $\bar{\sigma}_x = 24.9$ ksi, 90° Section Longitudinal Model . . . . .	87
43. Contours of Constant In-Plane Shear Stress (ksi), Average Applied Stress, $\bar{\sigma}_x = 24.9$ ksi, 90° Section Longitudinal Model . . . . .	88
44. Contours of Constant Octahedral Shear Stress, Normalized by Dividing by the Matrix Yield Value of 17 ksi, Average Applied Stress, $\bar{\sigma}_x = 84$ ksi, 90° Section Longitudinal Model . . . . .	89
45. Contours of Constant Octahedral Shear Strain ( $10^{-3}$ in/in), Average Applied Stress, $\bar{\sigma}_x = 84$ ksi, 90° Section Longitudinal Model . . . . .	90
46. Contours of Constant Maximum Principal Stress (ksi), Average Applied Stress, $\bar{\sigma}_x = 84$ ksi, 90° Section Longitudinal Model . . . . .	91
47. Contours of Constant In-Plane Shear Stress (ksi), Average Applied Stress, $\bar{\sigma}_x = 84$ ksi, 90° Section Longitudinal Model . . . . .	92
48. Fiber Loadings versus Distance from Plane of Fiber Break, Average Applied Stress, $\bar{\sigma}_x = 84$ ksi, 90° Section Longitudinal Model . . . . .	93
49. Contours of Constant Octahedral Shear Stress, Normalized by Dividing by the Matrix Yield Value of 17 ksi, Average Applied Stress, $\bar{\sigma}_x = 85.4$ ksi, 90° Section Longitudinal Model . . . . .	95

# LIST OF FIGURES (continued)

Figures	Page
50. Contours of Constant Octahedral Shear Strain ( $10^{-3}$ in/in), Average Applied Stress, $\bar{\sigma}_x = 85.4$ ksi, $90^\circ$ Section Longitudinal Model . . . . .	96
51. Contours of Constant Maximum Principal Stress (ksi), Average Applied Stress, $\bar{\sigma}_x = 85.4$ ksi, $90^\circ$ Section Longitudinal Model . . . . .	97
52. Contours of Constant In-Plane Shear Stress (ksi), Average Applied Stress, $\bar{\sigma}_x = 85.4$ ksi, $90^\circ$ Section Longitudinal Model . . . . .	98
53. Fiber Loadings versus Distance from Plane of Fiber Break, Average Applied Stress, $\bar{\sigma}_x = 85.4$ ksi, $90^\circ$ Section Longitudinal Model . . . . .	99
54. Contours of Constant Octahedral Shear Stress, Normalized by Dividing by the Matrix Yield Value of 17 ksi, Average Applied Stress, $\bar{\sigma}_x = 145.4$ ksi, $90^\circ$ Section Longitudinal Model . . . . .	100
55. Contours of Constant Octahedral Shear Strain ( $10^{-3}$ in/in), Average Applied Stress, $\bar{\sigma}_x = 145.4$ ksi, $90^\circ$ Section Longitudinal Model . . . . .	101
56. Contours of Constant Maximum Principal Stress (ksi), Average Applied Stress, $\bar{\sigma}_x = 145.4$ ksi, $90^\circ$ Section Longitudinal Model . . . . .	102
57. Fiber Loadings versus Distance from Plane of Fiber Break, Average Applied Stress, $\bar{\sigma}_x = 145.4$ ksi, $90^\circ$ Section Longitudinal Model . . . . .	103
58. Contours of Constant Octahedral Shear Stress, Normalized by Dividing by the Matrix Yield Value of 17 ksi, Average Applied Stress, $\bar{\sigma}_x = 146.8$ ksi, $90^\circ$ Section Longitudinal Model . . . . .	105
59. Fiber Loading versus Distance from Plane of Fiber Break, Average Applied Stress, $\bar{\sigma}_x = 146.8$ ksi, $90^\circ$ Section Longitudinal Model . . . . .	106
60. Contours of Constant Octahedral Shear Stress, Normalized by Dividing by the Matrix Yield Value of 17 ksi, Average Applied Stress, $\bar{\sigma}_x = 193.3$ ksi, $90^\circ$ Section Longitudinal Model . . . . .	107



# LIST OF FIGURES (continued)

Figures	Page
61. Contours of Constant Octahedral Shear Strain ( $10^{-3}$ in/in), Average Applied Stress, $\bar{\sigma}_x = 193.3$ ksi, $90^\circ$ Section Longitudinal Model . . . . .	108
62. Contours of Constant Maximum Principal Stress (ksi), Average Applied Stress, $\bar{\sigma}_x = 193.3$ ksi, $90^\circ$ Section Longitudinal Model . . . . .	109
63. Contours of Constant In-Plane Shear Stress (ksi), Average Applied Stress, $\bar{\sigma}_x = 193.3$ ksi, $90^\circ$ Section Longitudinal Model . . . . .	110
64. Plot of Applied Stress versus Composite Strain for the $90^\circ$ Section Longitudinal Model, 12.5 Percent Discontinuous Fibers . . . . .	111
65. Crack Propagation in the Transverse Section Model at an Average Applied Stress, $\bar{\sigma}_x = 58.4$ ksi. . . . .	113
66. Contours of Constant Octahedral Shear Stress (Normalized by Dividing by the Matrix Yield Value of 17 ksi) and Octahedral Shear Strain, Minimum Fiber Spacing Model ( $r_f/r_m = 0.714$ ), Average Applied Stress, $\bar{\sigma}_z = 17.4$ ksi. . . . .	115
67. Contours of Constant Maximum Principal Stress and In-Plane Shear Stress, Minimum Fiber Spacing Model ( $r_f/r_m = 0.714$ ), Average Applied Stress, $\bar{\sigma}_z = 17.4$ ksi. . . . .	116
68. Contours of Constant Octahedral Shear Stress (Normalized by Dividing by the Matrix Yield Value of 17 ksi) and Octahedral Shear Strain, Maximum Fiber Spacing Model ( $r_f/r_m = 0.424$ ), Average Applied Stress, $\bar{\sigma}_z = 32$ ksi. . . . .	118
69. Contours of Constant Maximum Principal Stress and In-Plane Shear Stress, Maximum Fiber Spacing Model ( $r_f/r_m = 0.424$ ), Average Applied Stress, $\bar{\sigma}_z = 32$ ksi. . . . .	119
70. Contours of Constant Octahedral Shear Stress (Normalized by Dividing by the Matrix Yield Value of 17 ksi) and Octahedral Shear Strain, $1\frac{1}{2}$ Maximum Fiber Spacing Model ( $r_f/r_m = 0.330$ ), Average Applied Stress, $\bar{\sigma}_z = 37.2$ ksi . . .	121
71. Contours of Constant Maximum Principal Stress and In-Plane Shear Stress, $1\frac{1}{2}$ Maximum Fiber Spacing Model ( $r_f/r_m = 0.330$ ), Average Applied Stress, $\bar{\sigma}_z = 37.2$ ksi. . . . .	122
72. Plot of Broken Fiber Surface Displacement versus Applied Stress, Axisymmetric Model . . . . .	123

# LIST OF SYMBOLS

<u>Symbol</u>	<u>Meaning</u>
$b_{ij}$	z-intercept of the line connecting nodes i and j of an element
E	Elastic modulus for isotropic materials
E'	Elastic modulus in the axial direction for a transversely isotropic material
$\bar{E}$	Octahedral shear stress-octahedral shear strain initial modulus
$\bar{E}_T$	Octahedral shear stress-octahedral shear strain tangent modulus
$f_{ij}^x$	Statically equivalent element force between node points i and j, applied in the x-direction
$\bar{F}_r$	Applied boundary force in the r-direction
$\bar{F}_x$	Applied boundary force in the x-direction
$\bar{F}_y$	Applied boundary force in the y-direction
$\bar{F}_z$	Applied boundary force in the z-direction
I	Integral coefficient
i, j, k, o, p, q	Indexing parameters
$m_{ij}$	Slope of a line connecting node points i and j of an element
n	Octahedral shear stress-octahedral shear strain parameter
$2M_T$	Octahedral shear stress-plastic octahedral shear strain tangent modulus
r, z, $\theta$	Polar coordinate directions
$\bar{r}, \bar{z}$	Polar coordinates of an element's centroid
$S_{ij}$	Stress deviator component
$\Delta U_i$	Strain energy density
$\delta(\Delta U)_i$	Change in strain energy density

**Symbol****Meaning**

$u,v,w$	Node point displacement components in the $x,y,z$ directions for Cartesian coordinates, in the $r,\theta,z$ directions for polar coordinates
$x,y,z$	Cartesian coordinate directions
$x_{ij},y_{ij}$	Distance between nodes $i$ and $j$ in the $x$ and $y$ directions, respectively
Dot over symbol (') Denotes incremental value	

**Vector Symbol**

$\{F\}_i$	Element node point force vector
$\{F\}$	Global node point force vector
$\{F_{\epsilon_0}\}$	Element dilatational strain-induced node point force vector
$\{R\}_i$	Reaction node point force vector representing the unloading of a failed element
$\{\delta\}_i$	Element node point displacement vector
$\{\epsilon\}$	Strain vector
$\{\epsilon_0\}$	Hygrothermal dilatational strain vector
$\{\sigma\}$	Stress vector
$\{\xi\}$	Vector of generalized element coordinates

**Matrix Symbols**

$[A]_i$	Element strain-displacement matrix
$[B]_i$	Element shape matrix, global coordinates
$[C]_i$	Element shape matrix, generalized coordinates
$[H]$	Material properties matrix
$[k]_i$	Element stiffness matrix, global coordinates
$[\bar{k}]_i$	Element stiffness matrix, generalized coordinates
$[K]$	Global stiffness matrix
$[T]$	Transformation matrix relating generalized to global coordinates

Greek SymbolsMeaning

$\alpha$	Coefficient of thermal expansion
$\beta$	Coefficient of moisture dilatation
$\delta_{ij}$	Kronecker delta
$\delta^*$	Virtual displacement
$\Delta$	Element cross-sectional area
$\epsilon_x, \epsilon_y, \epsilon_z$	Normal strain components, Cartesian coordinates
$\epsilon_r, \epsilon_z, \epsilon_\theta$	Normal strain components, polar coordinates
$\gamma_{xy}, \gamma_{xz}, \gamma_{yz}$	Shear strain components, Cartesian coordinates
$\gamma_{rz}, \gamma_{r\theta}, \gamma_{\theta z}$	Shear strain components, polar coordinates
$\gamma_o$	Octahedral shear strain
$\kappa$	Constant denoting strain in the z-direction
$\nu$	Poisson's ratio for an isotropic material
$\nu'$	Major Poisson's ratio for a transversely isotropic material
$\sum_c$	Indicates that a cyclic permutation of indices is required
$\sigma_x, \sigma_y, \sigma_z$	Normal stress components, Cartesian coordinates
$\bar{\sigma}_x, \bar{\sigma}_y, \bar{\sigma}_z$	Average applied normal stresses, Cartesian coordinates
$\sigma_r, \sigma_z, \sigma_\theta$	Normal stress components, polar coordinates
$\bar{\sigma}_r, \bar{\sigma}_z$	Average applied normal stresses, polar coordinates
$\tau_{xy}, \tau_{xz}, \tau_{yz}$	Shear stress components, Cartesian coordinates
$\tau_{rz}, \tau_{r\theta}, \tau_{\theta z}$	Shear stress components, polar coordinates
$\tau_o$	Octahedral shear stress

## SECTION 1

### INTRODUCTION

The present report includes work performed during the second year of a NASA-Lewis grant to study the energy absorption mechanisms during crack propagation in metal matrix composites. The first-year work was reported in Reference [1]. This previous report contains a literature review of micromechanics analyses of unidirectional composites, and a discussion of the relation of these prior studies to the present problem.

During the first year, an existing elastoplastic, finite element analysis and associated computer program [2,3] was used to predict the response of a unidirectional boron/aluminum composite to axial loading. For this purpose, a longitudinal section model was constructed. This model permitted the study of the influence of a broken fiber on the load distribution in adjacent unbroken fibers one and two fiber spacings away. It also permitted the determination of the rate of reloading of the broken fiber away from the site of the break. The influence of plastic deformation of the aluminum matrix on the stress distributions was of special interest. The addition of a crack initiation and propagation capability was initiated, but minor programming difficulties prevented results being presented in the first-year report.

The goal of the second-year study was to complete the crack propagation addition and generate detailed numerical results. Also, it was desired to construct larger longitudinal section models, to determine stress redistributions and influences of a broken fiber beyond the second adjacent fiber, and to determine the extent of influence of boundary loading

conditions. In addition, the existing generalized plane strain analysis was to be converted to an axisymmetric analysis, to permit the study of the response of a single fiber embedded in a cylindrical sheath of matrix material.

These second-year goals were achieved, as summarized in the next section, and described in detail in the remainder of this report.

## SECTION 2

### SUMMARY

The crack initiation and propagation capability became operational early in the second-year study. The entire analysis was then converted from a Sigma 7 computer system to the University's new CDC Cyber 730/760 computer, which had just been installed. The much greater capacity and speed of this new system made it practical to analyze much larger finite element grid arrays. Thus, new models were constructed, involving a greater number of fibers adjacent to the broken fiber, and greater lengths along the fiber axes. The results obtained using these larger models were then compared with previous results. The results of the first-year study were also extended beyond first failure, to analyze crack propagation behavior.

In addition to the longitudinal section models, transverse section models were also constructed and analyzed. These included arrays of unbroken fibers, and also a single broken fiber surrounded by unbroken fibers. Although axial loading was of primary interest, transverse loading was also studied. This permitted the comparison of results with other transverse loading results available in the literature [4-6], for verification purposes.

The crack propagation capability of the micromechanics analysis was found to perform very well, and is now considered to be fully operational.

The conversion of the generalized plane strain micromechanics analysis to an axisymmetric formulation proved to be more difficult than anticipated. The difficulty was not in the basic reformulation, but in the detailed modifications required in the associated computer program. Ultimately a second program was developed, as a more practical approach than attempting

to make the axisymmetric formulation an option in the original program. The axisymmetric analysis and associated computer program is now operational. Several example problems are presented in this report to demonstrate its capabilities.

While minor improvements will undoubtedly be incorporated into each of the now operational computer programs during the third-year effort, they are essentially complete. Attention will thus be focused on correlating predictions with available experimental data, and making parametric studies of the influences of various experimental variables, such as fiber volume, matrix properties, locations of fiber breaks, etc. Also, use will be made of a new three-dimensional finite element analysis recently completed as part of another study [7], to examine further the three-dimensional nature of stress states around broken fibers. This analysis will be useful directly in analyzing practical problems, and also for verification purposes in establishing the limits of applicability of the two-dimensional generalized plane strain and axisymmetric analyses, which are more economical to utilize.

It is anticipated that NASA-Lewis will be generating specialized and carefully controlled supporting experimental data also, primarily using single fiber specimens, to study fiber fracture and matrix deformations. The various analyses will be correlated with these experimental data.



### SECTION 3

#### GENERALIZED PLANE STRAIN ANALYSIS METHOD

The analysis formulation was presented in detail in the first-year report [1]. This has not changed, the governing equations and the flow chart which defines the operational features of the computer program modified to implement the analysis, which were presented in References [1], remain valid. Thus, only a brief summary need be given here.

The primary analytical tool used in the present study has been the micromechanics finite element analysis program developed by Miller and Adams [2,3]. This analysis was developed to investigate the microstress state in unidirectional composite materials subjected to axial and transverse mechanical loads, thermal gradients, and dilatational stresses due to moisture absorption by polymeric matrix materials. Among the special features of this prior University of Wyoming analysis are its ability to model the elastoplastic stress-strain response of the isotropic matrix material, and in concert with the determination of thermal and moisture dilatational stresses, the functional dependence of the matrix material properties on temperature and moisture content. In other words, the elastic or plastic properties of any matrix material finite element are automatically computed to reflect the state of stress and the environmental conditions of temperature and humidity. The adjustment of material properties is incorporated with the incremental loading technique that is employed in this program. Once the initial temperature, moisture content, and/or elastic stress level for the continuum have been specified, additional loads, be they mechanical or environmental, are introduced in increments

small enough to permit close approximation of the nonlinear matrix material properties by small linear segments. A detailed description of this technique is presented in References [1,2,3].

The bulk of the elastoplastic formulation in the present analysis program stems from previous work done by Adams [4-6,8,9]. The development of a generalized plane strain formulation, incorporation of the Branca solution technique [10], hygrothermal loading, and material properties dependence on temperature and moisture was the subject of Miller's Ph.D. research [2], while the addition of crack initiation and crack propagation capability follows the approach developed by Adams [4-6]. The analysis incorporates standard finite element techniques (see, among many other similar sources, References [11,12]). In fact, the primary organization and flow of the original computer program closely followed the suggestions of Appendix A of Reference [12]. This flow and organization has subsequently been rather severely altered to include crack propagation capability.

The finite element used in this study is a modified version of the familiar constant strain or simplex triangle. For this element, a linear displacement field within each element is assumed, to arrive at a functional representation of the potential energy of the system. The constant strain triangular element has some well-known limitations, but for the purposes of micromechanics analyses, it has proven to be an accurate, economical, and versatile tool. The trade-offs involved in the choice of the constant strain triangular element instead of one of the higher order finite elements is covered quite well by Miller and Adams in Chapter 3 of Reference [2].

A primary purpose of the present study was to investigate the affects of flaws in unidirectional boron/aluminum composites, with the eventual

goal of predicting the strength of such composites given a certain statistical distribution of internal flaws. These defects manifest themselves in two forms: a discontinuity in one or more boron fibers, or a localized void in the aluminum matrix. The loading condition of primary interest is that of tension applied parallel to the fiber axes. With suitable modification, a so-called longitudinal model was analyzed with the micromechanics program in its original form to investigate the problems of modeling a flaw, generally a fiber discontinuity, and to evaluate the resulting localized stress concentration and the local plastic deformation it caused. The redistribution of the load to the broken fiber could also be characterized, but only up to the point at which a matrix element failed (crack initiation). For further study of the load capability of the flawed composite, a crack propagation scheme is required. This capability permits a characterization of the energy required to isolate the defect in a "zone" of plastically deformed matrix material, or alternatively, the total energy capacity of the system at the point of catastrophic failure.

The approach to crack initiation and propagation taken here is known as the "failed element" approximation as employed by Adams [4-6]. When an element in an area of high stress exhausts its strain energy capacity, it fails. From this, we assume that a "crack" has formed and has the dimensions of the failed element. This approximation has two implications, the most important of which is that a finite amount of material is removed from the system, which in an actual material is not the case. The other is that the crack is not likely to close up on itself in subsequent loading because of its exaggerated width. These effects can be minimized to a practical

degree by making the finite element grid very fine and uniform in the area of anticipated crack initiation.

It is not enough to simply delete an element from the finite element grid when it reaches its ultimate stress. The finite element method involves the maintenance of force equilibrium at every node point in the array, as discussed in Appendix A of the first-year report [1]. This equilibrium must be maintained when an element fails or unloads. Thus, to represent the unloading due to element failure, node point forces which are equal and opposite in sense to those equivalent to the state of stress within the element at its failure level must be applied at its node points. In addition, the failed element's material properties must be set to zero, so that the element makes no further contribution to the global stiffness matrix, and all of its computed values of stress and strain are set to zero. This insures that the element is completely unloaded and that no stresses will be developed in it in subsequent load increments.

In the present analysis, element failure can occur in one of two modes: when both the computed octahedral shear stress and the plastic octahedral shear strain reach their maximum allowable values (maximum distortional energy criterion), or when the hydrostatic tensile stress in an element exceeds the tensile ultimate strength of the material. This second failure criterion is also known as failure due to ultimate cleavage, and failure occurs whenever a tensile principal stress exceeds the ultimate tensile strength. Complete details are given in Reference [1].

## SECTION 4

### AXISYMMETRIC ANALYSIS METHOD

#### 4.1. Purpose of the Axisymmetric Formulation

The development of an axisymmetric triangular finite element for the micromechanics analysis program was first proposed after the preliminary results of crack propagation studies using two-dimensional, generalized plane strain models had been examined. The difficulties and uncertainties of representing longitudinal loading of a square array of boron fibers embedded in an isotropic matrix led to the finite element models to be discussed in Section 6. As will also be discussed in considerable detail in Section 6, the effect of fiber spacing on the state of stress and the pattern of crack growth around an internal flaw is quite significant. It was thought that an axisymmetric formulation, allowing a fiber of circular cross section to be modeled, together with possible experimental correlation, might lead to the development of guidelines for the employment of the much more versatile generalized plane strain analysis. The parameter that is sought is an "effective" fiber spacing, that will accurately represent the relative affect of intact fibers surrounding a broken fiber, fibers that are, in general, not all equidistant from the flawed fiber.

The axisymmetric finite element model provides a correct representation of a single boron fiber in an annular sheath of aluminum matrix, as illustrated in Figure 1. The thickness of the annular sheath of aluminum can be changed quite readily, allowing the stress distribution around fiber flaws to be studied for various apparent fiber spacing conditions, with the circular cross section of the fiber being accounted for. It is proposed that a test specimen resembling this configuration be fabricated, and the

amount of displacement between the broken ends of the boron fiber at a specified load level be measured. This displacement could then be compared to the fiber displacement predicted by the micromechanics analysis, and used to confirm its validity. In addition, by careful correlation of these results, including the state of stress predicted by the axisymmetric formulation, to the strain and fiber displacement measurements of test specimens containing an arbitrary number of continuous fibers surrounding one discontinuous fiber, an effective fiber spacing could be arrived at for use in the two-dimensional generalized plane strain analysis. The ultimate objective, of course, is to verify the limits of accuracy of the two-dimensional analysis, and so avoid to the extent possible the much greater expense and complexity associated with using the three-dimensional formulation now available [7].

Initially, the implementation of an axisymmetric formulation was envisioned to be a relatively simple task. However, due to the special nature of the existing micromechanics computer program and the requirement for maximum accuracy throughout the region being analyzed, the development of an axisymmetric element proved to be considerably more complicated than was anticipated. Specifically, the manner in which boundary conditions and loading conditions are combined to allow a unique solution technique necessitated the complete rewriting of these routines for use in the axisymmetric computer program. In addition, since the material lying on the axis of radial symmetry (the  $z$ -axis in Figure 1) must necessarily be included in the analysis, the familiar approximate form of the axisymmetric element stiffness matrix [12] was found to be unacceptably inaccurate. In the subsections that follow, the development of an exact axisymmetric triangular element is presented and the reasons for its special form are discussed.

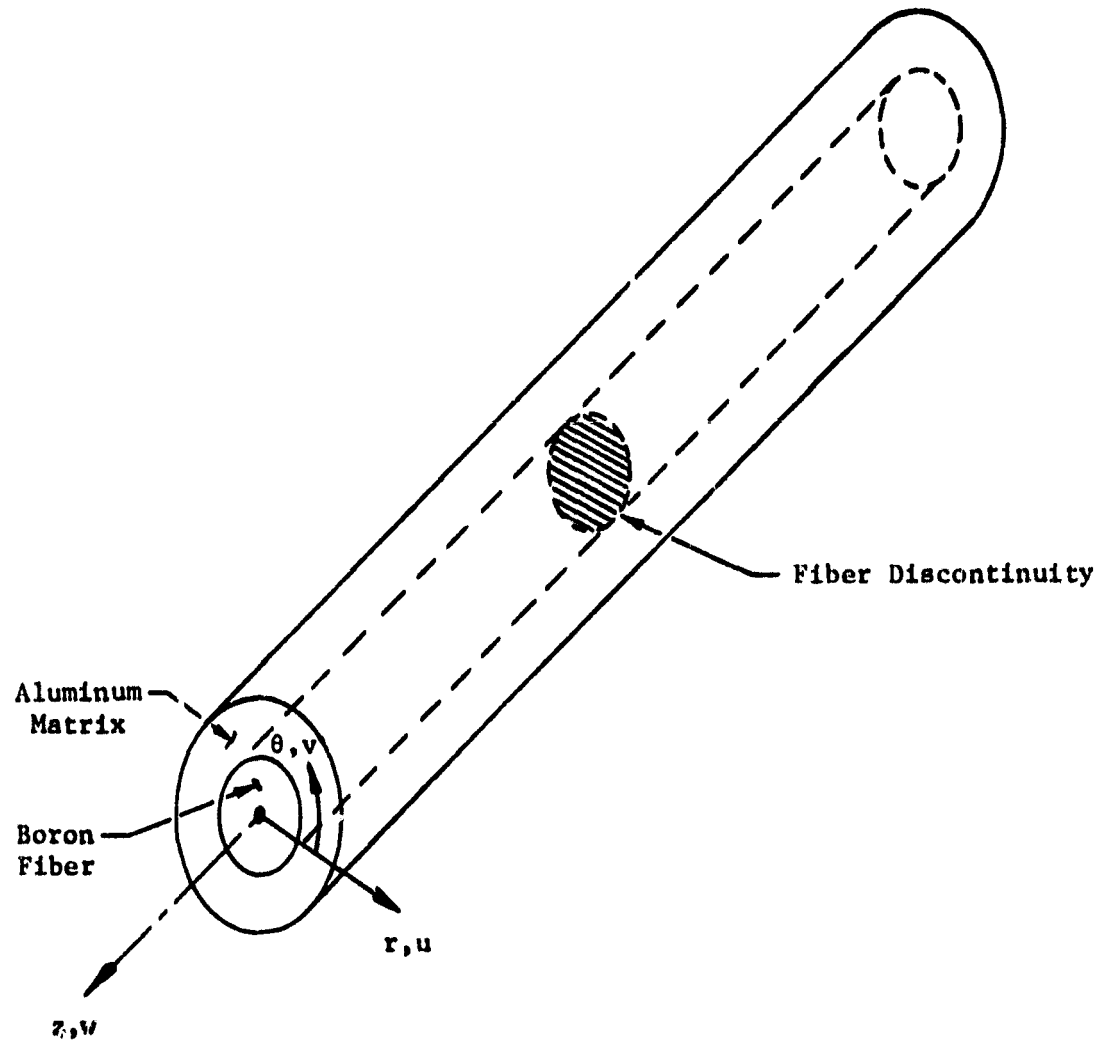


Figure 1. Region of Interest for the Axisymmetric Analysis

## 4.2. The Axisymmetric Finite Element

### 4.2.1. Basic Axisymmetric Relationships

The problem of analyzing a single fiber encased in an annular sheath of matrix material, and subjected to axial and radial tractions plus hygro-thermal gradients, falls into the class of problems known as torsionless axially symmetric states. These problems are generally defined relative to cylindrical coordinates  $(r, \theta, z)$ , and can be compared to the class of plane strain problems defined relative to Cartesian coordinates  $(x, y, z)$ , as follows:

- o The in-plane stress components of the cylindrical system,  $\sigma_r$  and  $\sigma_z$ , correspond to  $\sigma_x$  and  $\sigma_y$  of the plane strain formulation, while  $\sigma_\theta$  is the out-of-plane stress component, corresponding to  $\sigma_z$  of the Cartesian system.
- o The displacement components  $(u, v, w)$ , corresponding to the  $(r, \theta, z)$  coordinates are such that  $(u, v)$  are independent of the polar angle, and the out-of-plane displacement component,  $w$ , vanishes. That is,  $u = f(r, z)$ ,  $w = f(r, z)$ , and  $v = 0$ .

When the strain-displacement relations and the stress-strain relations of the theory of elasticity are applied to this state of torsionless axial symmetry, it is found that  $\tau_{\theta z} = \tau_{r\theta} = 0$ , and the stress components  $\sigma_r$ ,  $\sigma_\theta$ ,  $\sigma_z$  and  $\tau_{rz}$  are functions of coordinates  $(r, z)$  only.

An axisymmetric finite element is in the form of a toroidal ring of constant cross section, as illustrated in Figure 2. The node points of such an element are in fact nodal circles, and the volume of such an element is dependent on both its cross-sectional area and the radii of these



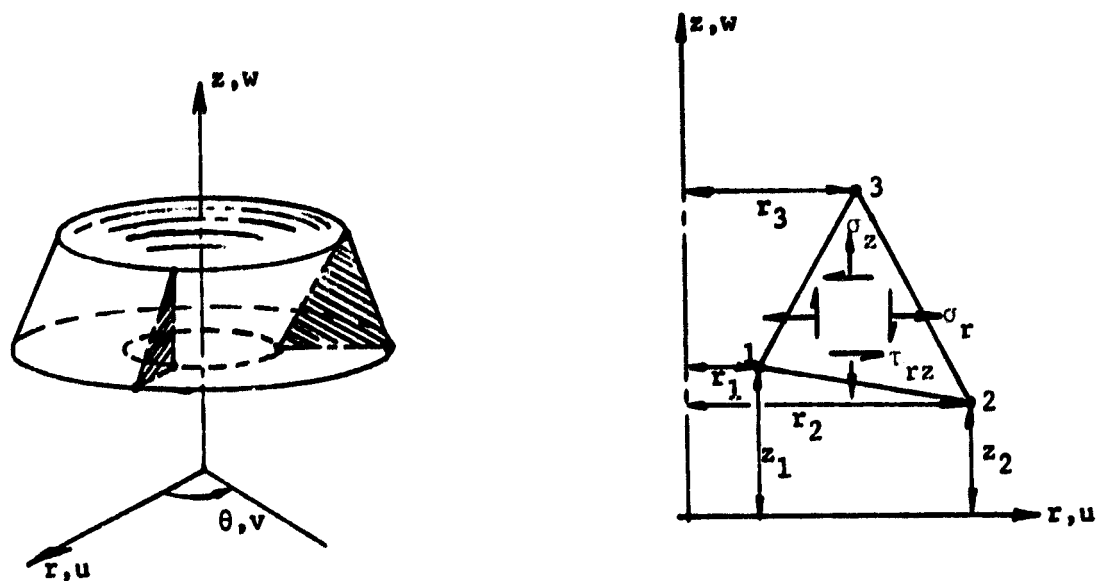


FIGURE 2. Solid Axisymmetric Triangular Element, Polar Coordinates

nodal circles. In addition, nodal loads are a function of node point radii and the load per unit of circumference. The stress and strain vectors pertinent to Figure 14, as well as the strain-displacement relations, are shown below. Note that the out-of-plane strain at a point,  $\epsilon_\theta$ , is a

$$\{\sigma\}_1 = \begin{Bmatrix} \sigma_r \\ \sigma_z \\ \tau_{rz} \\ \sigma_\theta \end{Bmatrix}_1 \quad (1)$$

$$\{\epsilon\}_1 = \begin{Bmatrix} \epsilon_r \\ \epsilon_z \\ \gamma_{rz} \\ \epsilon_\theta \end{Bmatrix}_1 \quad (2)$$

$$\begin{aligned}
\epsilon_r &= \frac{\partial u}{\partial r} \\
\epsilon_z &= \frac{\partial w}{\partial z} \\
\gamma_{rz} &= \frac{\partial u}{\partial z} + \frac{\partial w}{\partial r} \\
\epsilon_\theta &= \frac{u}{r}
\end{aligned} \tag{3}$$

function only of the radial displacement,  $u$ , and the radial coordinate,  $r$ . Stresses and strains are related by a material properties matrix,  $[H]$ , forming the following constitutive equation for any given element:

$$\{\sigma\}_1 = [H]_1 \{\epsilon\}_1 \tag{4}$$

The material properties matrices are given in Appendix A for isotropic elastic and transversely isotropic elastic materials, and for isotropic materials in the plastic range. In general, the forms of the material properties matrices for axially symmetric conditions are identical to those found in the case of generalized plane strain, in that the coefficients relating the various corresponding stress and strain components are identical. However, most texts dealing with axially symmetric problems arrange the components of the stress, strain, and material properties tensors in an order different from that presented here. To have employed the more generally accepted sequence of arranging these tensor components would have made it necessary to rewrite all of those routines in the computer program in which stresses, strains, failure modes, and crack propagation are determined. To avoid this difficulty, all relationships are derived here with the stress and strain components arranged in the same order as found in the generalized plane strain relationships presented in Reference [1].

#### 4.2.2. Approximate Axisymmetric Element Stiffness Formulation

As is the case with the generalized plane strain triangular element [1], a constant strain field is assumed to exist within each element, which leads to the derivation of a shape matrix relating element strains to nodal displacements. While this derivation is much like that for a plane strain triangular element, the presence of the  $r$ -coordinate in the denominator of several of the terms leads to considerable difficulty in evaluating the coefficients of the element stiffness matrix. The procedure is briefly outlined below, with Figure 3 provided as a visual aid in understanding the problem.

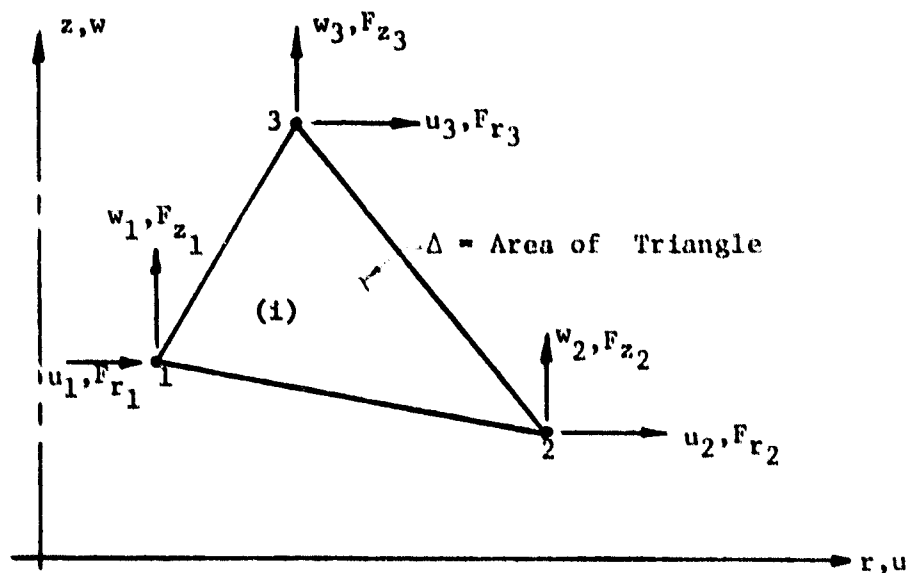


FIGURE 3. Finite Element i in the  $r$ - $z$  Plane

By choosing a displacement field in the simplest linear form (see Eq. A-12 and the related discussion in Appendix A of Reference [1]), we arrive at the following relationship,

$$\begin{Bmatrix} u \\ w \end{Bmatrix}_i = \begin{bmatrix} N_1 & 0 & N_2 & 0 & N_3 & 0 \\ 0 & N_1 & 0 & N_2 & 0 & N_3 \end{bmatrix} \begin{Bmatrix} u_1 \\ w_1 \\ u_2 \\ w_2 \\ u_3 \\ w_3 \end{Bmatrix} \quad (5)$$

where

$$\begin{aligned} N_1 &= \frac{1}{2\Delta} [a_1 + b_1 r + c_1 z] \\ N_2 &= \frac{1}{2\Delta} [a_2 + b_2 r + c_2 z] \\ N_3 &= \frac{1}{2\Delta} [a_3 + b_3 r + c_3 z] \end{aligned} \quad (6)$$

Differentiating Eq. (5) and applying Eqs. (3) we have:

$$\begin{Bmatrix} \epsilon_{rr} \\ \epsilon_{zz} \\ \gamma_{rz} \\ \epsilon_{\theta\theta} \end{Bmatrix} = \frac{1}{2\Delta} \begin{bmatrix} b_1 & 0 & b_2 & 0 & b_3 & 0 \\ 0 & c_1 & 0 & c_2 & 0 & c_3 \\ \frac{2\Delta N_1}{r} & 0 & \frac{2\Delta N_2}{r} & 0 & \frac{2\Delta N_3}{r} & 0 \\ c_1 & b_1 & c_2 & b_2 & c_3 & b_3 \end{bmatrix} \begin{Bmatrix} u_1 \\ w_1 \\ u_2 \\ w_2 \\ u_3 \\ w_3 \end{Bmatrix} \quad (7)$$

in which

$$\begin{aligned}
 a_1 &= r_2 z_3 - r_3 z_2 & a_2 &= r_3 z_1 - r_1 z_3 & a_3 &= r_1 z_2 - r_2 z_1 \\
 b_1 &= z_2 - z_3 & b_2 &= z_3 - z_1 & b_3 &= z_1 - z_2 \\
 c_1 &= r_3 - r_2 & c_2 &= r_1 - r_3 & c_3 &= r_2 - r_1
 \end{aligned} \tag{8}$$

the 4 x 6 rectangular matrix in Eq. (7) is the "shape matrix," [B], for the axisymmetric triangular element, and can be used to form the element stiffness matrix for individual elements. Note that the equation for the shear strain,  $\gamma_{rz}$ , has coefficients with  $r$  terms in the denominator. When a node (or nodes) of any element lies on the axis of rotation, i.e.,  $r = 0$ , singularities in the shape matrix result. In addition, when one considers the operation of forming the element stiffness matrix,

$$[k]_i = \int_{Vol} [B]^T [H] [B] d(Vol) \tag{9}$$

and the form of the shape matrix, [B], in Eq. (7), it is obvious that a term-by-term integration involving the  $r$  and  $z$  coordinates of the node points is necessary. The  $r$  terms that appear in many of these expressions result in some rather tedious calculations, and lead to logarithmic terms which can also result in singularities in the stiffness matrix. In the case of a plane strain or generalized plane strain element, the volume integral required by Eq. (9) is simply equal to the cross-sectional area of the element times its thickness, as described, for example, in References [11,12]. To avoid the difficulties presented by the  $r$  terms in the denominator of the shape matrix terms, an average shape matrix,  $[\bar{B}]$

can be formed, using the coordinates of the centroidal point of the triangle as the element's coordinates, and an element stiffness matrix can be calculated directly, i.e.,

$$[k]_1 = 2\pi[\bar{B}]^T[H][\bar{B}]\bar{r}\Delta \quad (10)$$

where

$$\bar{r} = (r_1 + r_2 + r_3)/3 \quad (11)$$

and

$$\bar{z} = (z_1 + z_2 + z_3)/3 \quad (12)$$

Solutions using the approximate element stiffness matrix of Eq. (10) have been found to be quite acceptable as long as the planar dimensions of the individual elements are small compared to their radial coordinates, say on the order of 10 to 1. In particular, hollow cylindrical bodies can be very adequately analyzed using the element stiffness formulation of Eq. (10). However, when the cylindrical body is solid, or possesses a very thick wall, large numerical errors are encountered when the approximate element stiffness matrix is used. In the present analysis, the axis of rotation is necessarily part of the region of investigation, and being composed of the very stiff boron fiber, carries a significant portion of any applied axial loads. Trial analyses using the approximate centroidal formulation of Eq. (10) indicated that very large numerical errors, on the order of 15 to 20 percent, were present in stress components that were normal to the direction of the applied axial load. After examining these numerical errors for several loading situations, and considering the need for the precision required if the objectives of the axisymmetric analysis were to be met, it was decided to formulate an exact axisymmetric element stiffness matrix, i.e., to perform the integrations indicated in Eq. (9).

#### 4.2.3. Exact Axisymmetric Element Formulation

In this section, a fairly thorough description of the derivation of the integral form of the axisymmetric triangular element is presented. In order to maintain the flow of the derivation, some of the more involved mathematical procedures have been placed in appendices, while the results of the procedures are used directly.

##### 4.2.3.1. Strain - Displacement Relationships

As is the case for planar, constant strain finite elements, a simple linear displacement field is chosen for the axisymmetric triangular element. This classifies it as a "simplex" element, but unlike the planar, or unit thickness, elements, it is derived in terms of the element's generalized coordinates,  $\{\xi\}$ . Planar elements, with their simpler strain-displacement relationships, allow direct evaluation of the shape function coefficients in terms of the finite element model's global coordinates. The displacement field relating the displacements of a point in the region of analysis to its generalized coordinates for a polar problem can be expressed as,

$$\begin{Bmatrix} u \\ w \end{Bmatrix}_1 = \begin{bmatrix} 1 & r & z & 0 & 0 & 0 \\ 0 & 0 & 0 & 1 & r & z \end{bmatrix} \{\xi\}_1 \quad (13)$$

This relationship can be shown to meet convergence criteria for conforming finite element displacement fields [10]. Substituting the nodal coordinates of an element such as that shown in Figure 3 into Eq. (13) yields

$$\begin{Bmatrix} u_1 \\ w_1 \\ u_2 \\ w_2 \\ u_3 \\ w_3 \end{Bmatrix} = \begin{bmatrix} 1 & r_1 & z_1 & 0 & 0 & 0 \\ 0 & 0 & 0 & 1 & r_1 & z_1 \\ 1 & r_2 & z_2 & 0 & 0 & 0 \\ 0 & 0 & 0 & 1 & r_2 & z_2 \\ 1 & r_3 & z_3 & 0 & 0 & 0 \\ 0 & 0 & 0 & 1 & r_3 & z_3 \end{bmatrix} \begin{Bmatrix} \xi_1 \\ \xi_2 \\ \xi_3 \\ \xi_4 \\ \xi_5 \\ \xi_6 \end{Bmatrix} \quad (14)$$

or

$$\{\delta\}_i = [T]_i \{\xi\}_i \quad (15)$$

where  $\{\delta\}_i$  is the element nodal displacement matrix,  $\{\xi\}_i$  is the element generalized coordinates matrix, and  $[T]_i$  is the element transformation matrix that relates the two. By examining the transformation matrix in Eq. (14), it can be seen that only translations are involved. In other words, the element is not derived with respect to a "natural" coordinate system, as in the case of a beam or isoparametric element. However, due to the need to evaluate specific integral coefficients, the terms  $\xi_1$  through  $\xi_6$  cannot be evaluated directly in terms of the global coordinates, as is the case for a plane strain simplex triangle. Solving Eq. (15) for  $\{\xi\}_i$  we obtain an equation relating the generalized coordinates to the nodal displacements,

$$\{\xi\}_i = [T]_i^{-1} \{\delta\}_i \quad (16)$$

where the inverse of  $[T]_i$  can be shown to be [3]



$$[T]^{-1}_i = \frac{1}{2\Delta} \begin{bmatrix} a_1 & 0 & a_2 & 0 & a_3 & 0 \\ b_1 & 0 & b_2 & 0 & b_3 & 0 \\ c_1 & 0 & c_2 & 0 & c_3 & 0 \\ 0 & a_1 & 0 & a_2 & 0 & a_3 \\ 0 & b_1 & 0 & b_2 & 0 & b_3 \\ 0 & c_1 & 0 & c_2 & 0 & c_3 \end{bmatrix}$$

in which  $\Delta$  equals the triangular cross-sectional area of the element, and the coefficients  $a_i$ ,  $b_i$  and  $c_i$  are as defined in Eq. (7).

Substitution of the assumed displacement field relationships, Eq. (14), into the definition of the strain components, Eq. (2), leads to

$$\begin{Bmatrix} \epsilon_{rr} \\ \epsilon_{zz} \\ \gamma_{rz} \\ \epsilon_{\theta\theta} \end{Bmatrix} = \begin{bmatrix} 0 & 1 & 0 & 0 & 0 & 0 \\ 0 & 0 & 0 & 0 & 0 & 1 \\ 0 & 0 & 1 & 0 & 1 & 0 \\ \frac{1}{r} & 1 & \frac{z}{r} & 0 & 0 & 0 \end{bmatrix} \begin{Bmatrix} \xi_1 \\ \xi_2 \\ \xi_3 \\ \xi_4 \\ \xi_5 \\ \xi_6 \end{Bmatrix} \quad (17)$$

or in matrix notation,

$$\{\epsilon\}_i = [C]_i \{\xi\}_i \quad (18)$$

where  $[C]_i$  is the shape matrix in terms of the element generalized coordinates. For global coordinates and displacements, we combine Eq. (16) and Eq. (17) to obtain

$$\{\epsilon\}_i = [C]_i [T]^{-1}_i \{\xi\}_i \quad (19)$$

which is the desired strain-displacement relationship.

#### 4.2.3.2. Element Stiffness Matrices

For the analysis of highly stressed, fiber-reinforced, metal matrix composites, three distinct element stiffness matrices are required; one to model an isotropic matrix material which is loaded below its elastic limit, another to model the fibers, which may be transversely isotropic, and a third to describe the behavior of the isotropic matrix when it is loaded into the plastic region. These three classes of material response are discussed in detail in Appendix A of Reference [1]. These same relationships are used to derive the required axisymmetric element stiffness matrices.

In general, a stiffness matrix relates nodal forces to nodal displacements. With the forces as known quantities, this allows the nodal displacements throughout the region of analysis to be solved for, and stress components can then be "backed out" of these displacements. The integration of the product of the shape matrix,  $[C]_1$ , and the stress-strain matrix,  $[H]_1$ , over the volume of an element yields its element stiffness matrix, i.e.,

$$[k]_1 = \int_{Vol} [B]_1^T [H]_1 [B]_1 d(Vol) \quad (20)$$

or, for an element stiffness expressed in generalized coordinates,

$$[\bar{k}]_1 = \int_{Vol} [C]_1^T [H]_1 [C]_1 d(Vol) \quad (21)$$

For an elastic, isotropic material, after substituting Eq. (17) and Eq. (A-14) of Reference [1] into Eq. (20) and performing the indicated matrix multiplications we have, after integrating with respect to  $\theta$ ,

$$[\bar{k}]_1 = \frac{2\pi E}{(1+\nu)(1-2\nu)} \left[ \begin{array}{cccccc} \frac{1-\nu}{r^2} & \frac{1}{r} & \frac{z(1-\nu)}{r^2} & 0 & 0 & \frac{\nu}{r} \\ & 2 & \frac{z}{r} & 0 & 0 & zv \\ & & \frac{(1-2\nu)}{2} + \frac{z^2(1-\nu)}{r^2} & 0 & \frac{1-2\nu}{2} & \frac{zv}{r} \\ & & & 0 & 0 & 0 \\ & & & & \frac{1-2\nu}{2} & 0 \\ & & & & & (1-\nu) \end{array} \right] r dr dz \quad (22)$$

SYMMETRIC

Integrating Eq. (22) with respect to r,

$$[\bar{k}]_1 = \frac{2\pi E}{(1+\nu)(1-2\nu)} \left[ \begin{array}{cccccc} (1-\nu)I_4 & I_2 & (1-\nu)I_5 & 0 & 0 & \nu I_2 \\ & 2I_1 & I_3 & 0 & 0 & 2\nu I_1 \\ & & (\frac{1}{2}-\nu)I_1 + (1-\nu)I_6 & 0 & (\frac{1}{2}-\nu)I_1 & \nu I_3 \\ & & & 0 & 0 & 0 \\ & & & & (\frac{1}{2}-\nu)I_1 & 0 \\ & & & & & (1-\nu)I_1 \end{array} \right] \quad (23)$$

SYMMETRIC

where E = Modulus of elasticity

$\nu$  = Poisson's ratio

and the integrals are represented as

$$\begin{aligned}
I_1 &= \int_r \int_z r dr dz & I_4 &= \int_r \int_z \frac{1}{r} dr dz \\
I_2 &= \int_r \int_z dr dz & I_5 &= \int_r \int_z \frac{z}{r} dr dz \\
I_3 &= \int_r \int_z z dr dz & I_6 &= \int_r \int_z \frac{z^2}{r} dr dz
\end{aligned} \tag{24}$$

The first three integrals are easily evaluated, and are defined in several finite element analysis texts, e.g., Reference [11]. They are

$$\begin{aligned}
I_1 &= \frac{(r_1+r_2+r_3)[r_1(z_2-z_3)+r_2(z_3-z_1)+r_3(z_1-z_2)]}{6} = \frac{\Delta(r_1+r_2+r_3)}{3} \\
I_2 &= \frac{[r_1(z_2-z_3)+r_2(z_3-z_1)+r_3(z_1-z_2)]}{2} = \Delta \\
I_3 &= \frac{(z_1+z_2+z_3)[r_1(z_2-z_3)+r_2(z_3-z_1)+r_3(z_1-z_2)]}{6} = \frac{\Delta(z_1+z_2+z_3)}{3}
\end{aligned} \tag{25}$$

The integrands of  $I_4$ ,  $I_5$  and  $I_6$  contain a  $(\frac{1}{r})$  term, and are considerably more difficult to evaluate.

In addition, when  $r_1$ ,  $r_2$  or  $r_3$  lie on the  $z$ -axis, the integrand becomes singular and special procedures must be employed to evaluate these terms. The procedure for evaluating these integrals is presented in Appendix A, and the manner in which singularities in the integrands are dealt with is described in Appendix B. For the most general case, however, the expressions for these integrals are presented below. For

each integral, the symbol  $\sum_c$  is used [11] to indicate that a cyclic permutation of the indices is necessary to obtain the full expression, i.e.,

$$\begin{aligned}
 I_4 &= \sum_c \frac{r_1 z_2 - r_2 z_1}{r_1 - r_2} \ln \frac{r_1}{r_2} \\
 &= \frac{r_1 z_2 - r_2 z_1}{r_1 - r_2} \ln \frac{r_1}{r_2} + \frac{r_2 z_3 - r_3 z_2}{r_2 - r_3} \ln \frac{r_2}{r_3} + \frac{r_3 z_1 - r_1 z_3}{r_3 - r_1} \ln \frac{r_3}{r_2}
 \end{aligned} \tag{26}$$

In a similar manner,

$$I_5 = \sum_c \frac{-(z_1 - z_2)}{4(r_1 - r_2)} [z_1(3r_2 - r_1) - z(3r_1 - r_2)] + \frac{1}{2} \left( \frac{r_1 z_2 - r_2 z_1}{r_1 - r_2} \right)^2 \ln \frac{r_1}{r_2} \tag{27}$$

and,

$$\begin{aligned}
 I_6 &= \sum_c \frac{(z_1 - z_2)}{18(r_1 - r_2)^2} [z_2^2(11r_1^2 - 7r_1 r_2 + 2r_2^2) + 2z_1 z_2 \left( \frac{5}{2}r_1^2 - 11r_1 r_2 + \frac{5}{2}r_2^2 \right) \\
 &\quad + z_1^2(11r_2^2 - 7r_1 r_2 + 2r_1^2)] + \frac{1}{3} \left( \frac{r_1 z_2 - r_2 z_1}{r_1 - r_2} \right)^3 \ln \frac{r_1}{r_2}
 \end{aligned} \tag{28}$$

The element stiffness matrix for the transversely isotropic (fiber) case is obtained in exactly the same manner as for the isotropic elastic case, except that the material properties matrix presented in Eq. (A-16) of Reference [1] is substituted into Eq. (20). This leads to the following transversely isotropic, generalized, element stiffness matrix,

$$[\bar{k}]_1 = \frac{2\pi E}{Q} \begin{bmatrix} (1-T)I_4 & (1-T+F)I_2 & (1-T)I_5 & 0 & 0 & FI_2 \\ & 2(1-T-F)I_1 & (1-T+F)I_3 & 0 & 0 & (+T+F)I_1 \\ & & \frac{Q}{2(1+\nu)}I_1 + (1-T)I_6 & 0 & \frac{Q}{2(1+\nu)}I_1 & I_3 \\ & & & 0 & 0 & 0 \\ & & & & \frac{Q}{2(1+\nu)}I_1 & 0 \\ & & & & & (1-T)I_1 \end{bmatrix} \quad (29)$$

SYMMETRIC

$$\text{where } Q = (1+\nu)(1-\nu - \frac{2E\nu'^2}{E'})$$

$$T = \frac{E\nu'^2}{E'}$$

$$F = \nu'(1+\nu)$$

$E'$  = Elastic modulus in the direction perpendicular to the plane of isotropy

$\nu'$  = Poisson's ratio representing a strain in the plane of isotropy due to a normal stress in the direction perpendicular to that plane.

For the element stiffness matrix of an isotropic material in the plastic range, the material properties matrix presented as Eq. (A-32) in Reference [1] is used in Eq. (20). After performing the required multiplications and integrations, we have, in terms of generalized coordinates, the isotropic, plastic element stiffness matrix. This expression is shown in Eq. (30).

The  $S_{ij}$  terms are components of the deviatoric stress tensor,  $\tau_0$  is the

$$[\bar{k}]_I = \left( \frac{2\tau E}{1+\nu} \right)$$

$(A - \frac{S_{33}^2}{B}) I_4$	$(2A - \frac{S_{33}^2 + S_{11}S_{33}}{B}) I_2$	$(A - \frac{S_{33}^2}{B}) I_5 - \frac{S_{12}S_{33}}{B} I_2$	0	$-\frac{S_{12}S_{33}}{B} I_2$	$(A - \frac{S_{22}S_{33}}{B}) I_2$
$[4A - (\frac{2S_{11}S_{33} + S_{11}^2 + S_{33}^2}{B})] I_1$	$[2A - (\frac{S_{33}^2 + S_{11}S_{33}}{B})] I_3$	0	0	$-\frac{S_{22}S_{11} - S_{12}S_{33}}{B} I_1$	$\frac{[A+A']}{S_{11}S_{12} + S_{22}S_{33}} I_1$
	$-\frac{S_{12}S_{11} + S_{12}S_{33}}{B} I_1$				
	$(\frac{1}{2} - \frac{S_{12}^2}{B}) I_1 + (A - \frac{S_{33}^2}{B}) I_6$	0		$(\frac{1}{2} - \frac{S_{12}^2}{B}) I_1$	$(A - \frac{S_{22}S_{33}}{B}) I_3$
	$-2 \frac{S_{12}S_{33}}{B} I_3$			$-\frac{S_{12}S_{33}}{B} I_3$	$-\frac{S_{12}S_{22}}{B} I_1$
		0	0	0	0
				$(\frac{1}{2} - \frac{S_{12}^2}{B}) I_1$	$-\frac{S_{22}S_{12}}{B} I_1$
					$(A - \frac{S_{22}^2}{B}) I_1$

SYMMETRIC

where  $A = (\frac{1-\nu}{1-2\nu})$

$A' = (\frac{\nu}{1-2\nu})$

(30)

$B = 3\tau_0^2 [1 + (1+\nu)] \frac{2M_T}{E}$

octahedral shear stress and  $2M_T$  is the tangent modulus of the octahedral shear stress-octahedral plastic shear strain curve, all of which are discussed in detail in Appendix A of Reference [1].

Each of the element stiffness matrices given by Eqs. (23), (29), and (30) must be expressed in terms of the global coordinates of the finite element model before they can be used to assemble the global stiffness matrix. This is accomplished by evaluating the inverse of the transformation matrix for each element, as defined in Eq. (16), and using the following relationship:

$$[k]_1 = ([T]^{-1})_1^T [\bar{k}]_1 [T]_1^{-1} \quad (31)$$

The global stiffness matrix,  $[K]$ , is assembled, element by element, by a subroutine which also imposes the boundary conditions required for the specialized loading technique (see Appendix A-4 of Reference [1]). In this subroutine, each element in the model is examined to determine whether it is fiber or matrix, elastic or plastic, and the appropriate element stiffness subroutine is called. In these element stiffness subroutines, the strain-displacement matrix and the stress-back substitution matrix for each element is evaluated and stored on a peripheral device. These are required to obtain element strains and stresses from the nodal displacements that the finite element solution provides. In general,

$$\{\sigma\}_1 = [H]_1 [C]_1 [T]_1^{-1} \{\delta\}_1 = [H]_1 [A]_1 \{\delta\}_1 = [B]_1 \{\delta\}_1 \quad (32)$$

where  $[A]_1$  is the strain-displacement matrix and  $[B]_1$  is the stress-back substitution matrix.

These matrices have to be evaluated for each of the three material conditions. The most general form of the  $[A]_1$  and  $[B]_1$  matrices are shown



below, and specialized forms are presented in Appendix B. For the elastic isotropic case,

$$[B]_i = \frac{E}{(1+\nu)(1-2\nu)} \begin{bmatrix} \frac{\nu}{r} & 1 & \frac{z}{r} & 0 & 0 & \nu \\ \frac{\nu}{r} & 2\nu & \frac{\nu z}{r} & 0 & 0 & (1-\nu) \\ 0 & 0 & (\frac{1}{2} - \nu) & 0 & (\frac{1}{2} - \nu) & 0 \\ \frac{(1-\nu)}{r} & 1 & (1-\nu)\frac{z}{r} & 0 & 0 & \nu \end{bmatrix} [T]^{-1} \quad (33)$$

For the elastic, transversely isotropic case,

$$[B]_i = \frac{E}{Q} \begin{bmatrix} \frac{F}{r} & (1+F-T) & F\frac{z}{r} & 0 & 0 & (\nu+T) \\ \frac{F}{r} & (\nu+T) & F\frac{z}{r} & 0 & 0 & (1-T) \\ 0 & 0 & \frac{Q}{2(1+\nu)} & 0 & \frac{Q}{2(1+\nu)} & 0 \\ \frac{(1-T)}{r} & (1+F-T) & (1-T)\frac{z}{r} & 0 & 0 & F \end{bmatrix} [T]^{-1} \quad (34)$$

where  $T$ ,  $F$ , and  $Q$  are as defined in Eq. (29). The stress-back substitution matrix for a plastic isotropic material is as shown in Eq. (35) on the next page, with the terms  $A$ ,  $A'$ ,  $B$ , and  $S_{ij}$  as defined in Eq. (30). It is interesting to compare the elastic and plastic cases, especially in the terms that are zero for the elastic  $[B]$  matrix and negative for the plastic matrix. As is also the case for the plastic element stiffness matrix versus the elastic form, the negative sense of the additional terms is

a reflection of the reduced modulus of most elastic-plastic materials when in the plastic range.

The strain-displacement matrix, being a function of element geometry only, is the same for all three material conditions, i.e.,

$$[A]_1 = \begin{bmatrix} 0 & 1 & 0 & 0 & 0 & 0 \\ 0 & 0 & 0 & 0 & 0 & 1 \\ 0 & 0 & 1 & 0 & 1 & 0 \\ \frac{1}{r} & 1 & \frac{z}{r} & 0 & 0 & 0 \end{bmatrix} [T]^{-1} \quad (36)$$

It is important to note that for a given set of nodal displacements, Eqs. (33), (34), and (35) describe the variation of stresses within the element as a function of the  $r$  and  $z$  coordinates. In other words, using these relationships, the exact state of stress at any point in the plane of the element can be obtained. In this study, the centroid location of each element has been programmed in as the element point of interest.

This concludes the description of the exact, triangular, constant strain axisymmetric element. It is important to realize that those elements that have a node point or a side coincident with the axis of rotation, sometimes referred to as "core" elements [12], require special treatment. Elements having one side parallel to the  $z$ -axis also lead to singularities. These special cases, described in detail in Appendix B, make the computer implementation of this formulation particularly complicated, as the strain-displacement and back substitution matrices must also be modified. Comparison of the exact formulation of the element to the approximate form

$$\begin{aligned}
 [B]_1 \frac{E}{1+\nu} &= \begin{bmatrix} \frac{1}{r} \left( A - \frac{S_{11} S_{33}}{B} \right) & \frac{S_{11}^2 + S_{11} S_{33}}{B} & \frac{S_{11} S_{33}}{r} & \frac{S_{11} S_{12}}{B} \\ \frac{1}{r} \left( A - \frac{S_{22} S_{33}}{B} \right) & \frac{S_{11} S_{22} + S_{22} S_{33}}{B} & \frac{S_{22} S_{33}}{r} & \frac{S_{22} S_{12}}{B} \\ - \frac{S_{12} S_{33}}{2r} & - \frac{S_{11} S_{12} - S_{12} S_{33}}{B} & \frac{S_{12} S_{33}}{2} + \left( \frac{1}{2} - \frac{S_{12}^2}{B} \right) & - \frac{S_{22} S_{12}}{B} \\ \left( A - \frac{S_{33}}{B} \right) \frac{1}{r} & \frac{S_{11} S_{33} + S_{33}^2}{B} & \frac{S_{12} S_{33}}{r} & \frac{S_{22} S_{33}}{B} \end{bmatrix} \begin{bmatrix} \frac{S_{11} S_{12}}{B} \\ \frac{S_{22}^2}{B} \\ - \frac{S_{22} S_{12}}{B} \\ \frac{S_{22} S_{33}}{B} \end{bmatrix} \\
 & \quad \quad \quad [\tau^{-1}] \quad (35)
 \end{aligned}$$

indicates that the additional effort necessary to develop and implement the integral form is justified. For axial loads applied to a model of "core" elements, the error in  $\sigma_r$  stresses is on the order of 14 percent for the approximate formulation. The error in  $\sigma_0$  stresses is on the order of 18 percent. For radial or combined loads, the error observed in the approximate element formulation is even larger.

## SECTION 5

### MATERIAL PROPERTIES

In modeling the boron/aluminum composite, the boron fibers have been treated as brittle, linearly elastic materials with isotropic strength and stiffness properties. The aluminum matrix has also been considered to be isotropic, but is modeled as an elastoplastic material. To accomplish this, the actual stress-strain curve of the aluminum alloy selected is input to the analysis by curve fitting via a Richard-Blacklock two-parameter equation [13], as discussed in Appendix A-5 of Reference [1]. Thus, at any load level the tangent modulus for any given element can be computed. This makes possible an accurate representation of the plastic deformation of the matrix.

Although the nonlinear material properties of any matrix material, e.g., another aluminum alloy, can readily be incorporated in the analyses, a 6061-T6 aluminum alloy at 75°F was used in obtaining the present results. The material properties shown in Table 1 were obtained from Reference [14]; the full range stress-strain curve for determining the curve fit parameters used is shown in Figure 4.

TABLE 1

#### Aluminum Matrix Material Properties - 6061-6 Alloy [14]

Young's Modulus	E	= $10.0 \times 10^6$ psi
Poisson's Ratio	$\nu$	= 0.33
Tensile Yield Strength	$F_{ty}$	= 36000 psi
Tensile Ultimate Strength	$F_{tu}$	= 45000 psi
Coefficient of Thermal Expansion	$\alpha$	= $13.0 \times 10^{-6}/^{\circ}\text{F}$

The boron fiber properties indicated in Table 2 were obtained from Reference [15].

TABLE 2  
Boron Fiber Material Properties [15]

Young's Modulus	$E = 60.5 \times 10^6 \text{ psi}$
Poisson's Ratio	$\nu = 0.130$
Tensile Ultimate Strength	$F_{tu} = F_{ty} = 500,000 \text{ psi}$
Ultimate Strain	$\epsilon_{tu} = \frac{F_{tu}}{E} = 8.264 \times 10^{-3} \text{ in./in.}$
Coefficient of Thermal Expansion	$\alpha = 9.0 \times 10^{-6}/^\circ\text{F}$

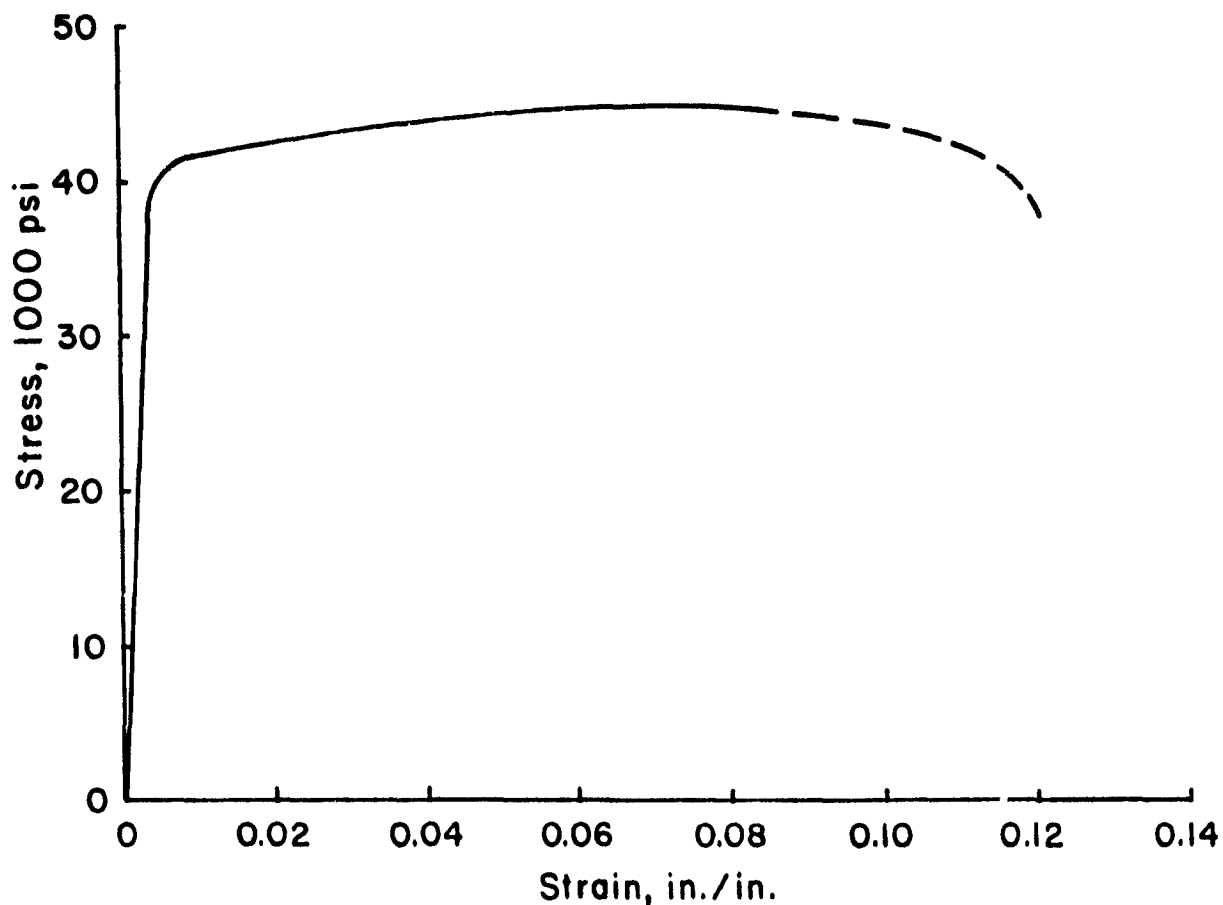


Figure 4. Typical Full Range Stress-Strain Curve for 6061-T6 Aluminum Alloy at Room Temperature [14]

## SECTION 6

### NUMERICAL RESULTS

In this section, the finite element analysis methods discussed in Sections 3 and 4 are applied to a variety of finite element models.

In Sections 6.1 and 6.2, the development of the various finite element models is discussed, for use with the generalized plane strain analysis (described in Section 3) and the axisymmetric analysis (described in Section 4), respectively.

In Sections 6.3 and 6.4, numerical results are presented for axial loading of the longitudinal section models, while axial loading of the transverse section models is presented in Section 6.5. Transverse loading of the transverse section model is discussed in Section 6.6.

In Section 6.3, the results of the axial loading of models representing a condition of 33 percent discontinuous fibers are discussed. At the time these results were generated, early in the present second-year study, the basic computer program, developed during the first-year study [1], was still in a somewhat unrefined condition; nearly all the reduction of output data had to be done by hand. With the conversion of the computer program to the larger, faster Control Data Corporation Cyber 730/760 computer system, installed at the University of Wyoming in early 1980, a post-processing package was added which is capable of drawing the material interfaces of the finite element model, the outline of any crack that might be present, and a variety of stress and strain contours, as specified by the user. The results of the analysis of the considerably larger and more complex models then possible are discussed in Section 6.4.

Sections 6.5 and 6.6 deal with the mechanical loading of transverse section finite element models. As a result of these studies, transverse section models have been found to be incapable of adequately representing stress concentrations due to material defects when loaded in the direction of the fiber axes. However, they are especially useful in studying the effects of transverse mechanical loads and hygrothermal loads.

Preliminary results of the newly developed axisymmetric analysis are presented in Section 6.7. These results demonstrate the capability of the analysis; more investigation remains to be done.

#### 6.1. Generalized Plane Strain Analysis Models

##### 6.1.1. Development of the Broken Fiber, Longitudinal Section Models

There are two primary reasons for the development of a longitudinal section model. One is to permit study of localized stress concentrations, the resulting elastoplastic behavior of the aluminum matrix, and subsequent crack propagation in the area of fiber flaws. Another is to characterize the load carrying capability of a flawed fiber as a function of distance from the location of the fiber flaw.

These two considerations lead to the most important aspects of designing the longitudinal section models, i.e., geometry, finite element grid resolution, boundary conditions in the vicinity of a flaw, and spacing of the boron fibers in the model. The problem of fiber spacing will be discussed first.

A typical cross section of a unidirectional, square array, boron/aluminum composite as shown in Figure 5, the section being perpendicular to the fiber axes. A longitudinal section finite element model attempts



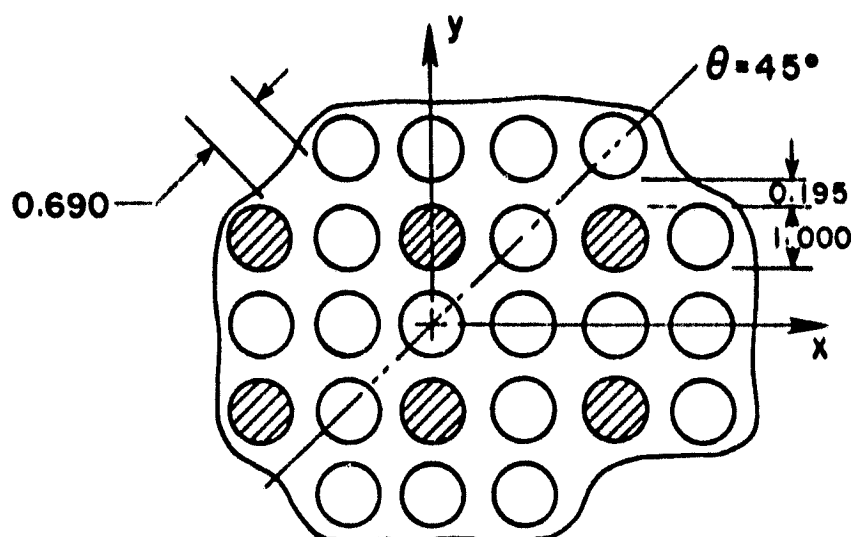


FIGURE 5. Cross Section of a Square Array of Fibers, 55 Percent Fiber by Volume

to represent the composite in a plane oriented perpendicular to this section. A longitudinal model of a section parallel to the x or y axes, through the centers of the fibers, would be representative of the minimum distance between fibers. A section cut at  $45^\circ$  to the x-axis and through the fiber centers would depict a maximum fiber spacing situation. When one of these fibers is broken, the load it carries decays to zero at the broken surface, assuming that the boron-aluminum interface remains intact. At the flaw site, the fibers adjacent to the broken fiber, and to some extent the surrounding aluminum matrix, must absorb the load that the broken fiber would have otherwise carried. The aluminum transfers this excess load back into the broken fiber via a shear mechanism so that at some distance from the fiber break, that fiber is again fully effective in carrying load. It is logical to presume that the amount of aluminum between the boron fibers will have an effect on this load transfer mechanism. To characterize the effects of variation in fiber spacing, two longitudinal models were studied, one representing a  $90^\circ$  section cut of the transverse cross section, and another representing a  $45^\circ$  section cut. A  $45^\circ$  section model is shown in Figure 6,

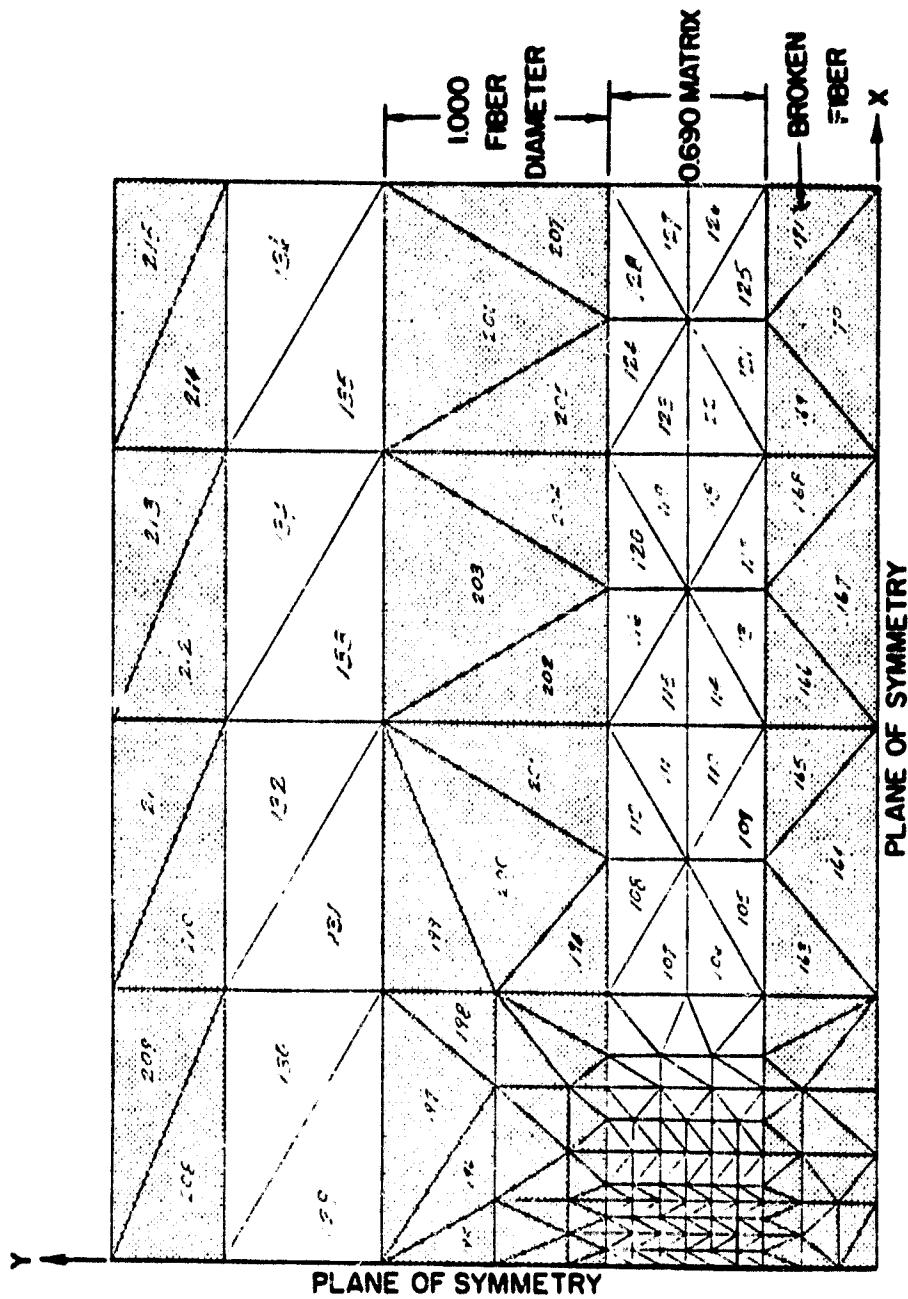


FIGURE 6. 45° Section Longitudinal Model with 33.3 Percent Discontinuous Fibers

the element numbers being indicated. The region in the lower left corner, with unnumbered elements, is the region in the vicinity of the broken fiber end. This local region is shown in the expanded view in Figure 7, the element numbers being given here. A  $90^\circ$  section model is shown in Figure 8. Note that the fiber diameter dimensions have been normalized to unity. In Figure 8 the effect of the  $90^\circ$  section cut in diminishing the amount of local aluminum matrix is shown quite clearly. The size and aspect ratios of the fiber elements are exactly the same as those of Figure 6, but the aluminum elements of the  $90^\circ$  section model are so compressed that the element numbers, which are identical to those of Figure 6, have been eliminated for clarity.

The second problem that must be solved in the finite element modeling of a broken fiber in a composite is the geometry in the area of the fiber discontinuity-matrix interface. The efforts of the present investigators to resolve this problem have been evolutionary in nature and many models were developed and discarded in the process. It will be noted, for example, that the models of Figures 6 through 8 are slightly different in the region of the broken fiber end than the models presented in Figures 3.6 through 3.8 in Reference [1].

As the longitudinal finite element models evolved, the problem of computer capacity came to be a limiting factor. The models shown in Figures 6 through 8 yielded generally favorable results, but represented the limits of the capability of the Xerox Sigma 7 computer then being used. After study of the numerical results obtained using these models, it was decided that they were limited in three important areas. The first was the modeling of the region in which crack growth is expected to occur.

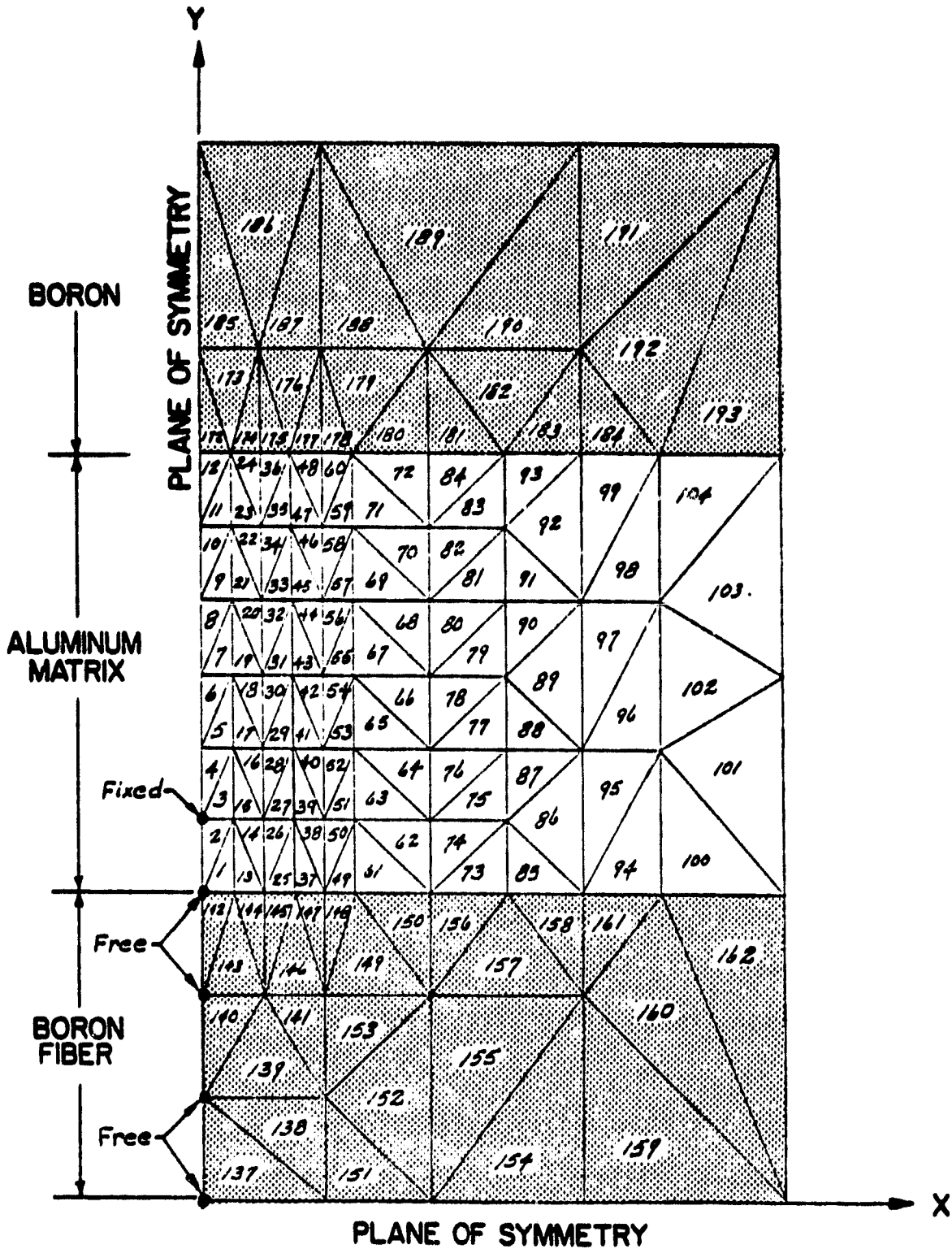


FIGURE 7. Finite Element Representation of the Local Region Around the Broken Fiber End in Figure 6.

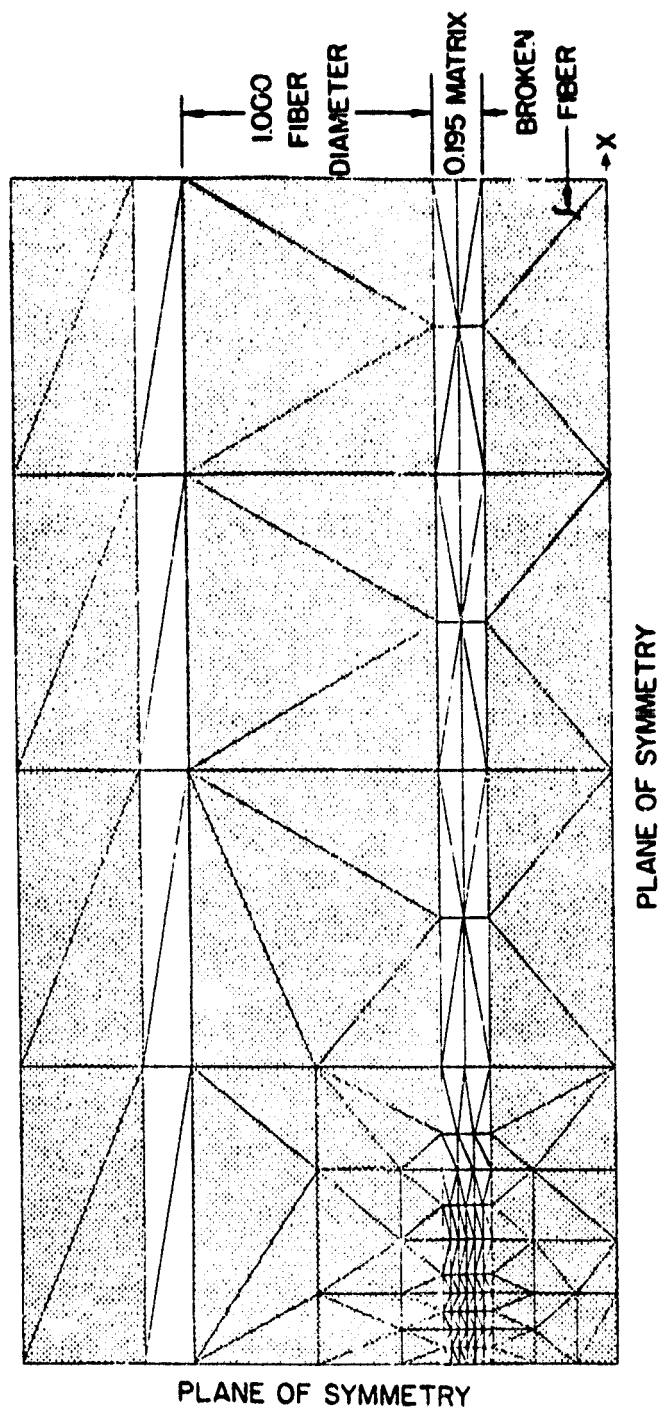


FIGURE 8. 90° Section Longitudinal Model with 33.3 Percent Discontinuous Fibers

Ideally, this region should contain an extensive area of uniform elements of approximately the same size as the elements forming the initial crack. This is due to the fact that when a significantly larger element is encountered by the growing crack, propagation ceases until this larger element and its neighbors have been strained to their ultimate value. When such a large element fails, the released energy is to be redistributed among the surrounding elements is considerable, and the result is that many more elements fail in the process. This also dictates the formation of a fairly large cavity within the model, which may affect the pattern of subsequent crack propagation in an unrealistic manner. This was particularly noticeable in the case of the  $90^\circ$  section model. A second limitation of a small model is that it represents a situation in which fully one-third of the fibers are broken. In other words, the effects of a broken fiber on the loading of more remote intact fibers cannot be studied; fibers which may have a considerable affect on the pattern and extent of crack growth. Finally, the limited axial length of the small models of Figures 6 and 8 was thought to be an unfavorable influence in terms of end effects. As will be discussed, this limitation prevented the loading of the material being modeled to its full capacity due to the arrival of the crack front at the right boundary of the model.

With the acquisition of the much larger and faster CDC Cyber 760 computing facility, larger and more complex models could subsequently be studied. The two larger finite element models created for this purpose are presented in Figures 9 and 10, representing  $45^\circ$  section and  $90^\circ$  section longitudinal models, respectively. In them, 12.5 percent of the fibers are discontinuous. It will be noted that, in addition to an extensive

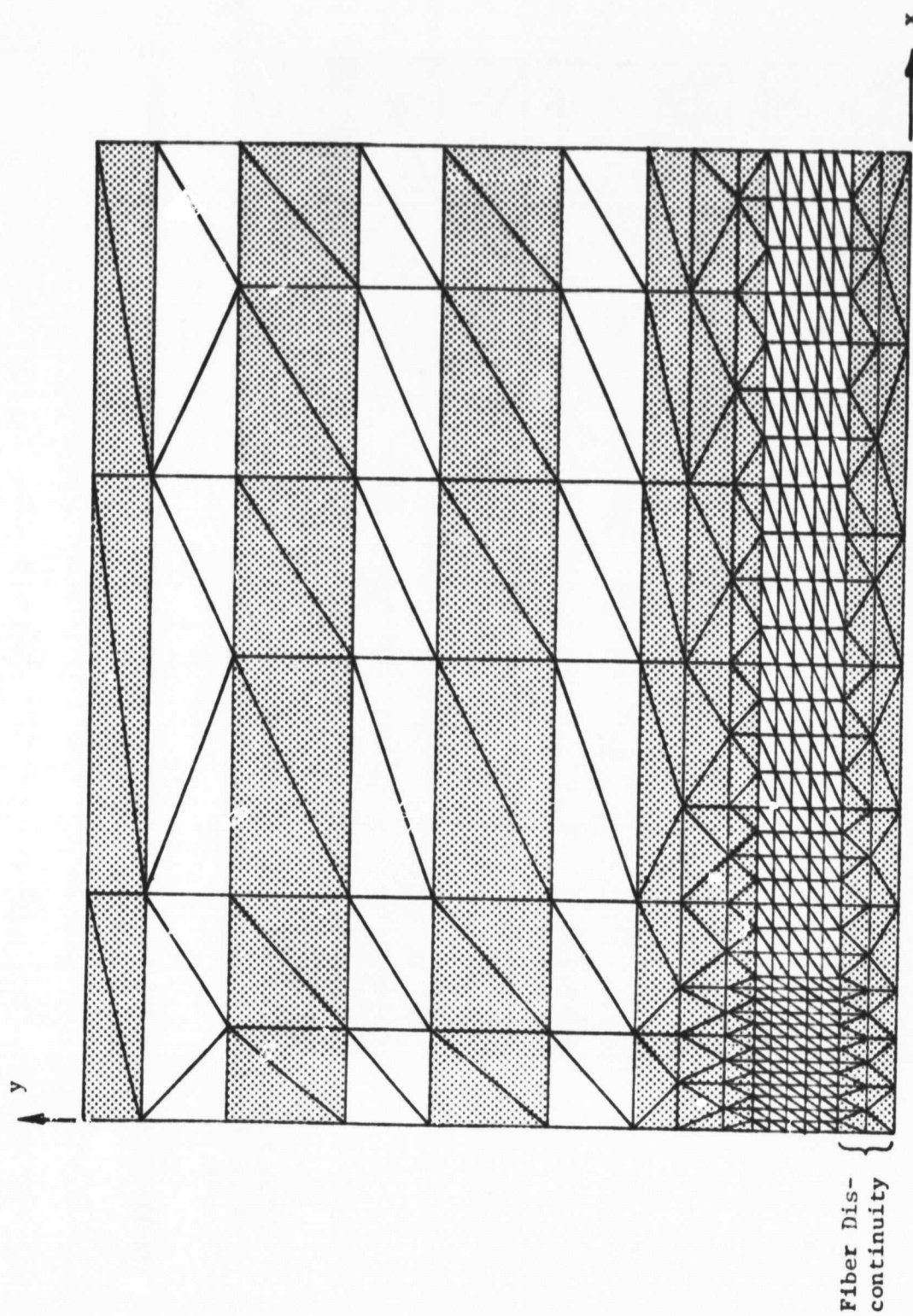


FIGURE 9. Refined 45° Section Longitudinal Model with 12.5 Percent Discontinuous Fibers, 8.2 Fiber Diameters in Length.

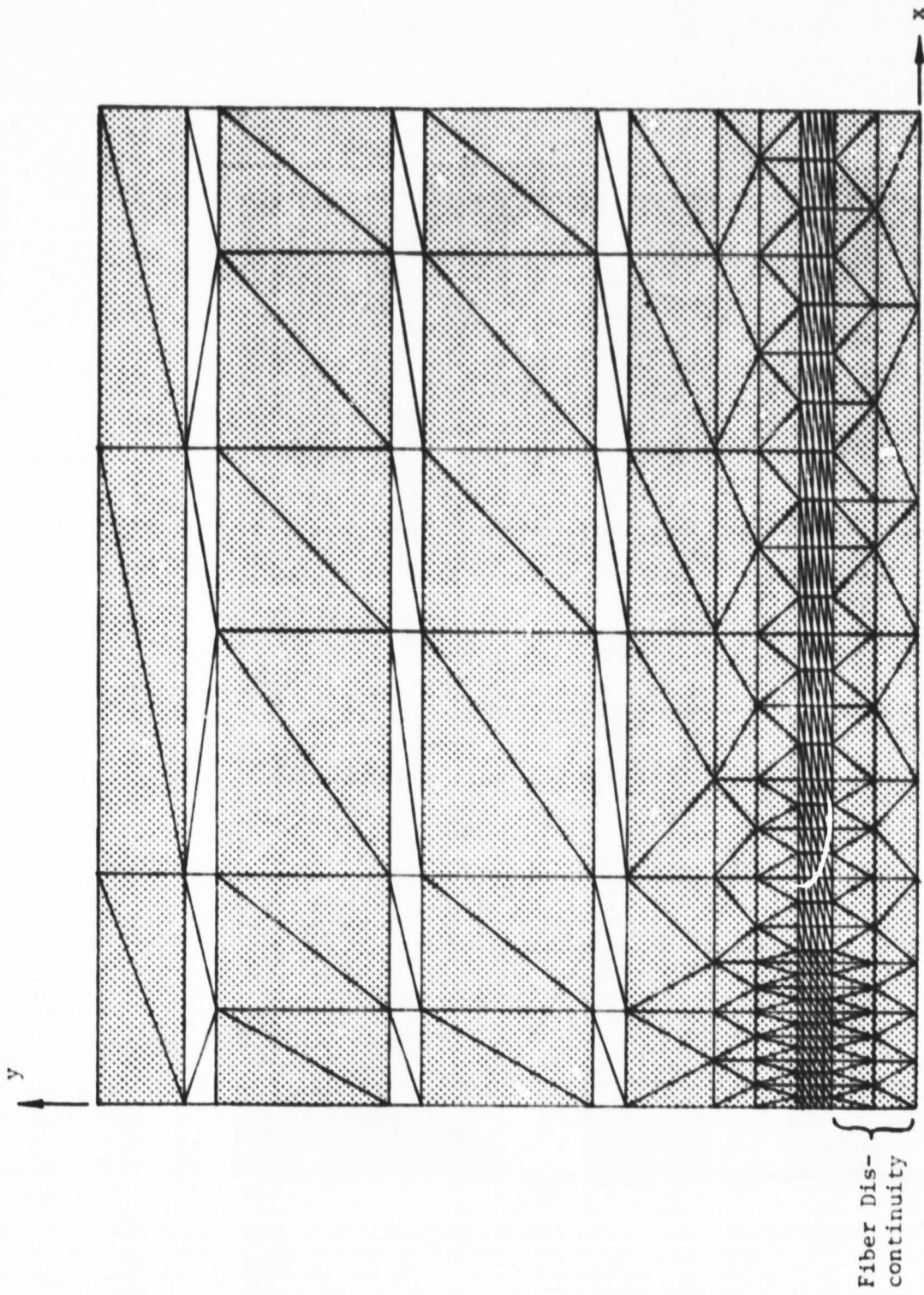


FIGURE 10. Refined 90° Section Longitudinal Model with 12.5 Percent Discontinuous Fibers, 8.2 Fiber Diameter in Length.



region of uniform matrix elements adjacent to the fiber discontinuity, many rows of elements are retained in the region between this fiber and its neighbor, along the full length of the model.

#### 6.1.2. Development of the Transverse Section Models

Finite element modeling of a transverse section of a unidirectional boron/aluminum composite is fairly straightforward [4-6,8,9]. A typical transverse section model is shown in Figure 11. This model will be used here to demonstrate crack propagation in an unflawed composite subjected to a transverse normal loading. However, the need to study the influence of a reduced load capacity in one fiber on its neighboring fibers requires that a minimum section model such as that shown in Figure 12 be employed. This model represents the first quadrant of a repeating square array of four fibers. If the fiber centered at the origin is assumed to be a flawed fiber, it will be surrounded by eight other (unflawed) fibers in the array. A model of this type can easily lead to a great number of finite elements, and attempting to increase the resolution of the grid at selected locations often results in a very large bandwidth of the overall stiffness matrix for the finite element model.

#### 6.2. Axisymmetric Analysis Models

The finite element model used for the preliminary studies using the axisymmetric element formulation is shown in Figure 13. In this model, the horizontal axis is the r-axis, while the vertical axis is defined as the z-axis, or axis of rotation. The fiber elements are located along the z-axis and extend radially outward for three "bays" of elements. The fiber discontinuity is modeled by freeing the first four node points at the lower

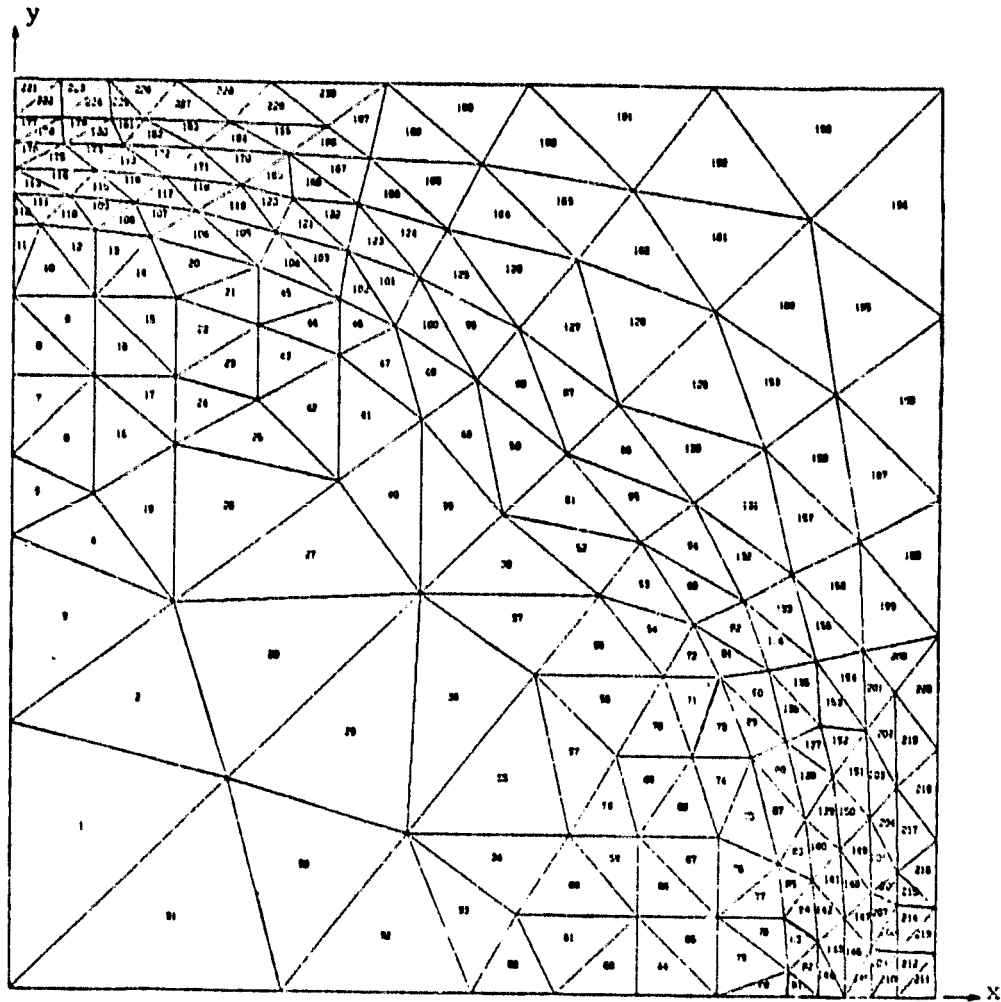


FIGURE 11. Transverse Section Finite Element Model of a Square Array of Unflawed Fibers, 55 Percent Fiber by Volume.

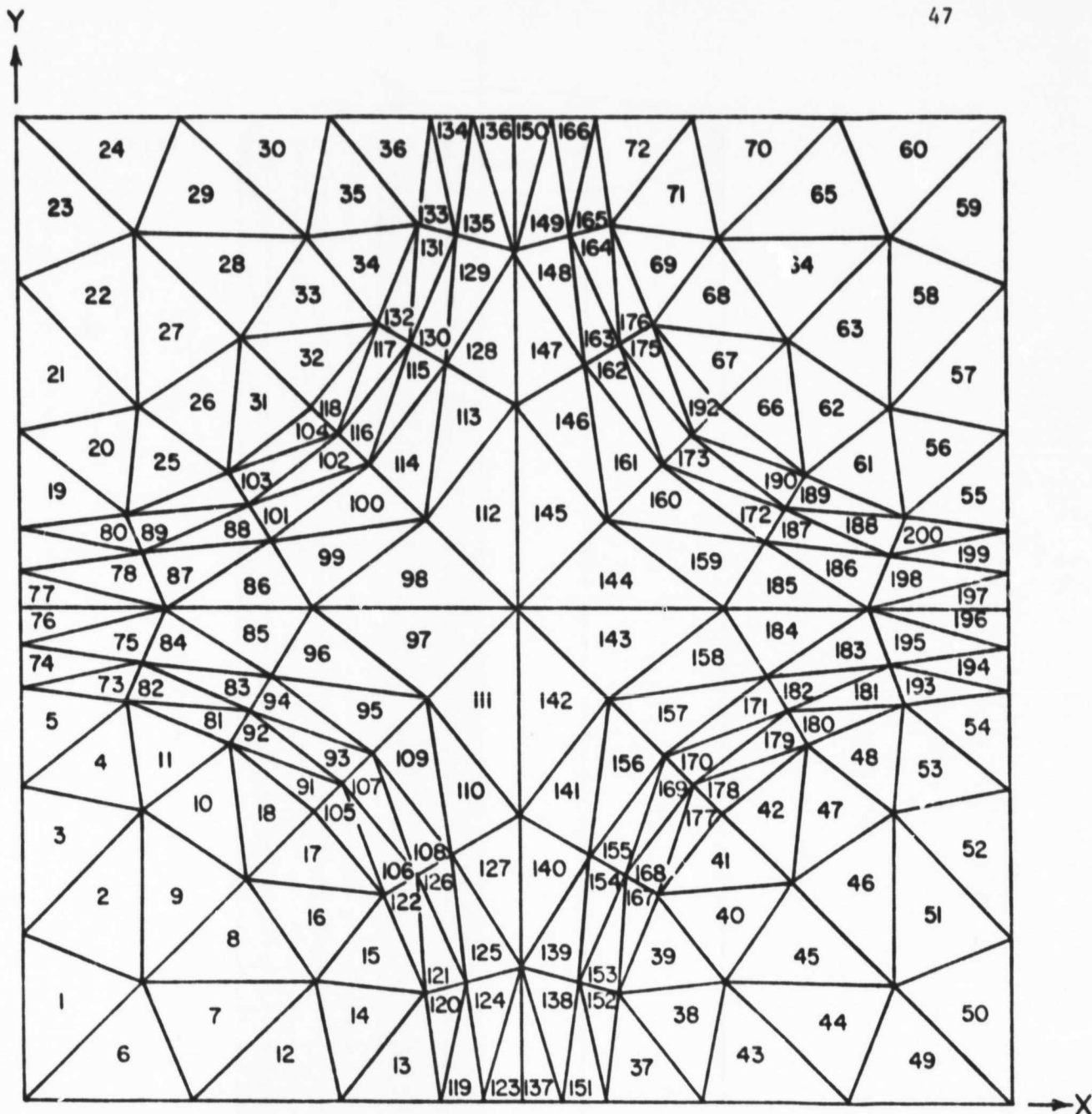


FIGURE 12. Transverse Section Finite Element Model of a Repeating Square Array of Four Fibers, 55 Percent Fiber by Volume.

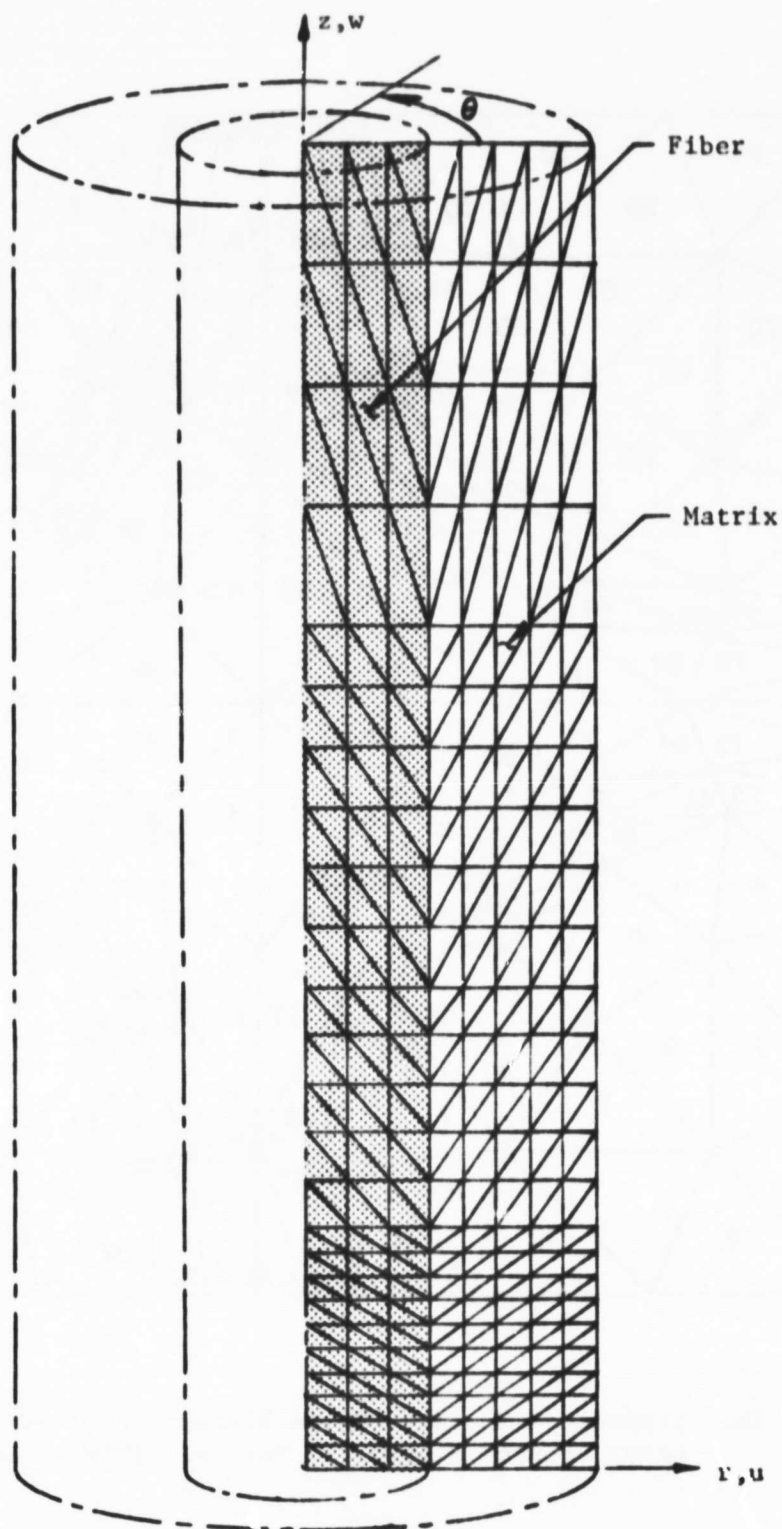


FIGURE 13. Axisymmetric Finite Element Model Representation of the Maximum Fiber Spacing in a 55 Percent Fiber Volume, Square Array, Unidirectional Composite ( $r_f/r_m = 0.424$ ). Model Length is 5.5 Fiber Diameters.

left corner of the model, extending radially outward. The philosophy in creating this model is similar to that followed in the specification of the generalized plane strain models of Section 6.1, i.e., maximum element resolution in areas of high stress gradients. Minimum stiffness matrix bandwidth is achieved by maintaining continuous node point numbering from one end of the model to the other in at least one coordinate direction. This can lead to a few more elements than are required in some cases, but it has been found that the savings in computer core space due to a reduced bandwidth far outweigh the cost of a few superfluous elements. In addition, the dimensions and matrix thickness of this model are very easily changed, making it particularly useful for parametric studies of the effects of fiber volume on the response of this particular configuration.

### 6.3. Axial Loading of Longitudinal Models With 33 Percent Discontinuous Fibers

#### 6.3.1. Crack Initiation and Propagation in the 45° Section Longitudinal Model

The 45° section longitudinal model was loaded axially with one boron fiber treated as discontinuous, the broken ends being in contact when loading was initiated. Crack initiation occurred with the failure in octahedral shear stress of Element No. 2 (see Figure 7) at an average applied stress of 64.1 ksi. The release of energy caused by the failure of Element No. 2 resulted in the failure of seven additional elements, Nos. 1, 3, 4, 13, 14, 15, and 26. With the stiffness capacity of these elements deleted from the analysis and their strain energy redistributed to the remaining model, 13 more elements failed. This process of crack growth at constant stress continued in a regular pattern until the "crack" had

progressed to the point shown in Figure 14. The elements that have failed are blacked out.

After crack growth had ceased, monotonic loading of the composite was continued to an average applied stress level of 107.2 ksi without further element failures. As loading progressed, the aluminum matrix elements adjacent to the fiber nearest the discontinuous fiber experienced increasing amounts of plastic straining. The shaded elements in Figure 14 are those in the plastic stress range at an average applied stress level of 107.2 ksi. An examination of the in-plane components of stress for these elements revealed that in the elements nearest the crack tip, shear stress was of the greatest magnitude. In the plastically strained elements farthest from the crack tip, tensile stress, parallel to the fiber axes, was again the major stress component, although the shear stress level was still high.

As the crack formed and grew, the load level in the broken fiber decreased relative to that of the intact fibers, as expected. The pattern of crack growth exhibited by this analysis, and the manner in which each element was deformed and failed primarily by shear stress, is very similar to experimental results obtained by Awerbuch and Hahn [16]. In their study, center-notched tension specimens of unidirectional boron/aluminum were tested. Microscopic examination of the failed test specimens revealed crack growth in the aluminum matrix adjacent to the last cut boron fiber on either side of the notch. These cracks appeared to propagate parallel to the fiber axes, and were accompanied by long zones of plastic shear deformation in the matrix, also running parallel to the fiber axes.

At an average applied stress of 107.2 ksi, Element No. 136, located between the two continuous fibers (see Figure 6), failed in hydrostatic

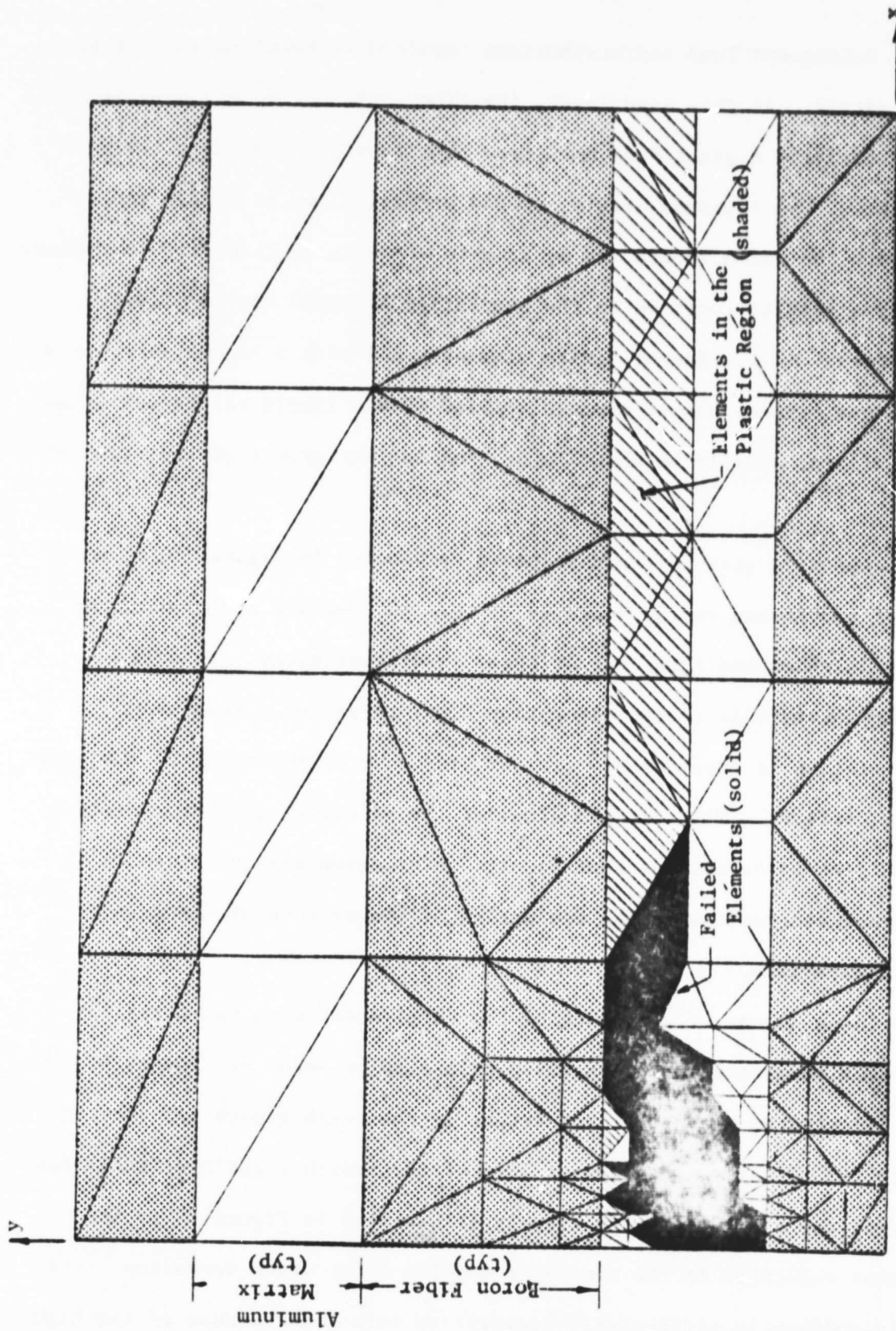


FIGURE 14. Extent of Crack Growth and Plastic Deformation at an Average Applied Stress of 107.2 ksi, 45° Section Longitudinal Model. Crack Initiation Occurred at 64.1 ksi.

tension. Subsequent load redistributions resulted in total failure of the aluminum matrix. At this load level, the fiber adjacent to the discontinuous fiber was carrying a great deal more load than it would have were there no broken fiber. The aluminum matrix, loaded primarily due to strain compatibility with the boron fibers and by Poisson effects, is predicted to rupture when the analysis is confined to the boundaries of these smaller finite element models. For a longer finite element model with a higher percentage of continuous fibers, higher average applied stress levels can be sustained without failure, as will be shown later, and further growth of the crack will occur.

The composite stress-strain response is plotted in Figure 15, as a measure of the strain energy capacity of this 45° section boron/aluminum composite in which one fiber out of three is discontinuous. It will be noted that the rate of energy absorption with increasing stress after crack initiation is considerably greater than that exhibited up to the point of initial failure. That is, the slope of the stress-strain curve is less. From this plot it is obvious that plastic deformation and crack growth are important considerations in the evaluation of the effects of flaws in composite materials.

The large amount of straining of the total model that takes place during crack formation and propagation will also be noted in Figure 15. This further illustrates the effect and extent of the crack growth illustrated by Figure 14. Finally, the loss of some of the broken fiber's effectiveness in carrying the applied load is clearly illustrated in Figure 15 by the significant reduction in the composite modulus after crack formation. This change in modulus is particularly dramatic in this case because of the high



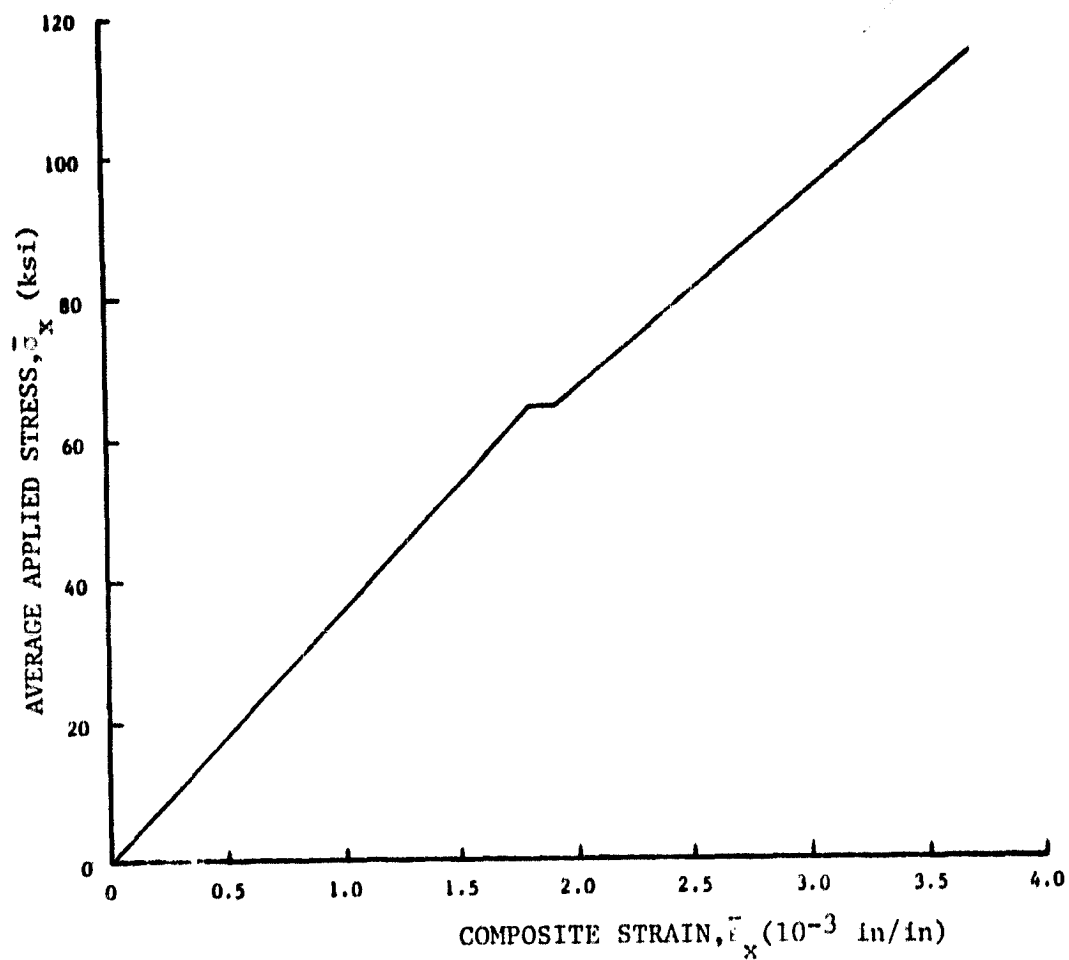


FIGURE 15. Plot of Applied Stress versus Composite Strain for the 45° Section Longitudinal Model, 33.3 Percent Discontinuous Fibers

percentage (33 percent) of discontinuous fibers, the extent of crack propagation, and the relatively short axial dimension of the model being investigated.

### 6.3.2. Crack Initiation and Propagation in the 90° Section Longitudinal Model

When the 90° section longitudinal model was loaded in a direction parallel to the fiber axes, with one fiber broken, a large stress concentration occurred at the crack tip, as was the case with the 45° section longitudinal model. However, the composite axial stiffness of the 90° section model is considerably greater than that of the 45° section model, due to the larger fiber volume fraction of the 90° model.

The closer proximity of an intact fiber with the broken one in the 90° model results in a greater shear stress gradient at the end of the broken fiber than was seen in the 45° model. As a result, crack initiation occurred at an average applied stress level of 37.1 ksi, due to the failure of Element No. 2, as defined in Figure 7. Subsequent load redistributions resulted in a series of single element failures, until finally the failure of Element No. 42 triggered the failure of Element Nos. 53, 54, and 55, with Element Nos. 65, 66, and 67 failing after that. At this point, crack propagation ceased, with plastic deformation around the crack tip and along the fiber progressing as the load level was increased to 84.0 ksi. Figure 16 illustrates the pattern of crack growth and plastic deformation at this level of applied stress.

In comparing Figure 16 with Figure 14, the difference in the shape and extent of the crack is as obvious as the difference in load level. The higher shear stress gradient brought about by the closer fiber spacing

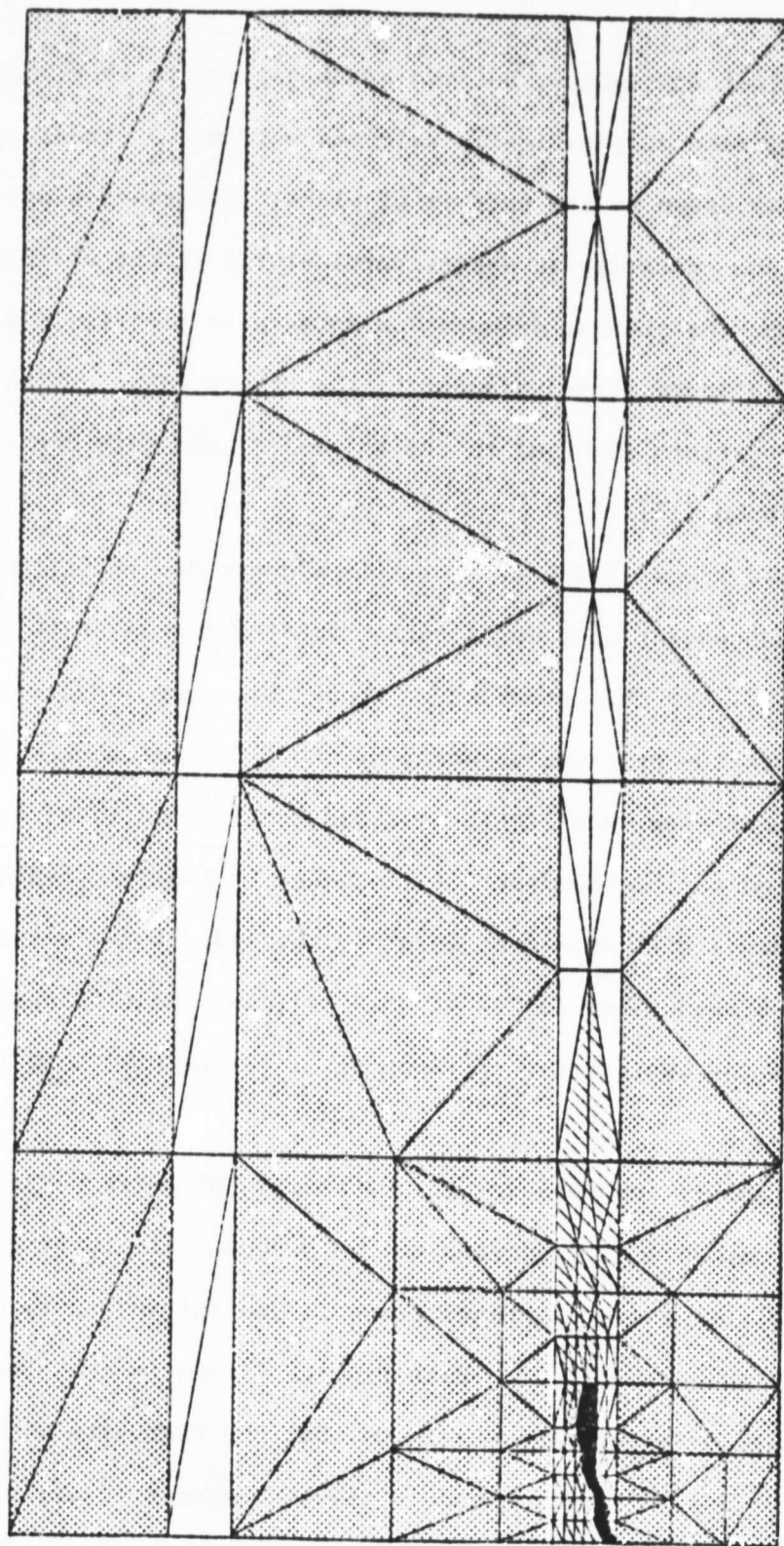


FIGURE 16. Extent of Crack Growth and Plastic Deformation at an Average Applied Stress of  $\bar{\sigma} = 84.0$  ksi,  $90^\circ$  Section Longitudinal Model. Crack Initiation Occurred at  $\bar{\sigma}_x = 37.1$  ksi.

causes earlier crack initiation, but the crack appears to be promptly contained by a large zone of plastically deformed matrix. A strong similarity between the two is shown by the pattern of plastic deformation and in the fact that it is due primarily to shear, particularly in the vicinity of the crack tip. Again, the plastic deformation appears to progress down the boundary of the unflawed fiber adjacent to the broken fiber, which is consistent with the pattern observed in the  $45^\circ$  model, and with the experiments of Awerbuch and Hahn [16].

At an average stress level of 84.1 ksi, Element No. 78 failed (see Figure 7), and subsequent element failures resulted in the crack pattern shown in Figure 17. At this point, the "crack" was over 5 fiber diameters long, extending to the opposite boundary of the finite element model. The broken fiber is carrying very little load under this condition, as it is now only connected to the remainder of the model by a single node point at the right boundary. With continued loading, the last of the matrix elements adjacent to the broken fiber failed at 98.0 ksi, and their release of energy triggered the rupturing of Element No. 134 (see Figure 6) by hydrostatic tension.

The energy absorption capacity of the flawed  $90^\circ$  section model of a boron/aluminum composite is indicated by the stress-strain plot of Figure 18. Very little pure straining takes place in the initial stage of crack growth, as depicted by Figure 16. Both Figures 15 and 18 are plotted to the same scales of stress and strain so that the composite axial stiffnesses of the  $45^\circ$  and  $90^\circ$  section models may be compared visually. As was the case with the  $45^\circ$  section model, the  $90^\circ$  section model exhibits a reduction of stiffness after crack initiation and propagation, due to a

ORIGINAL PAGE IS  
OF POOR QUALITY

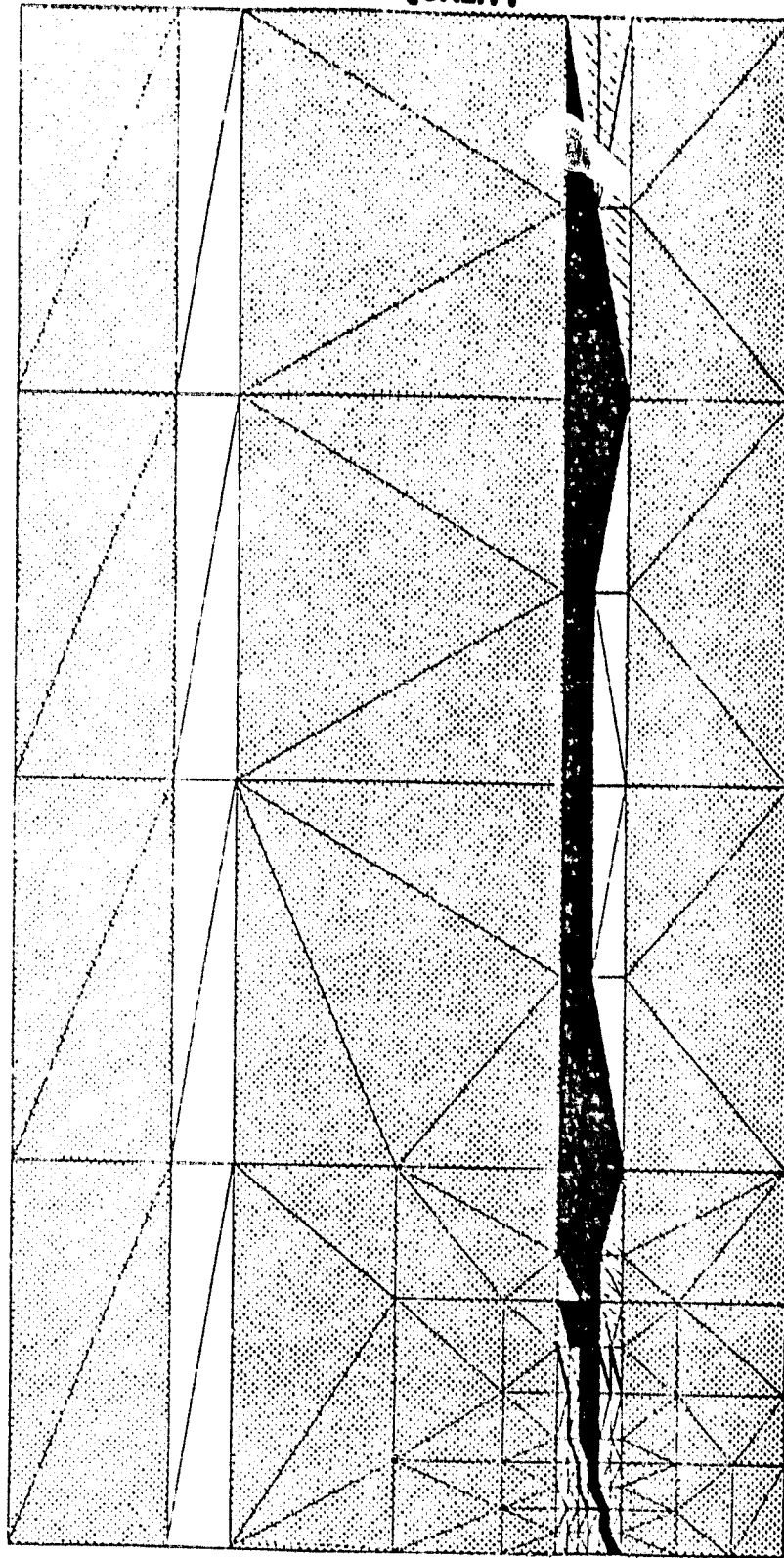


FIGURE 17. Subsequent Crack Growth and Plastic Deformation at an Average Applied Stress of  $\bar{\sigma}_x = 94$  ksi, 90° Section Longitudinal Model.

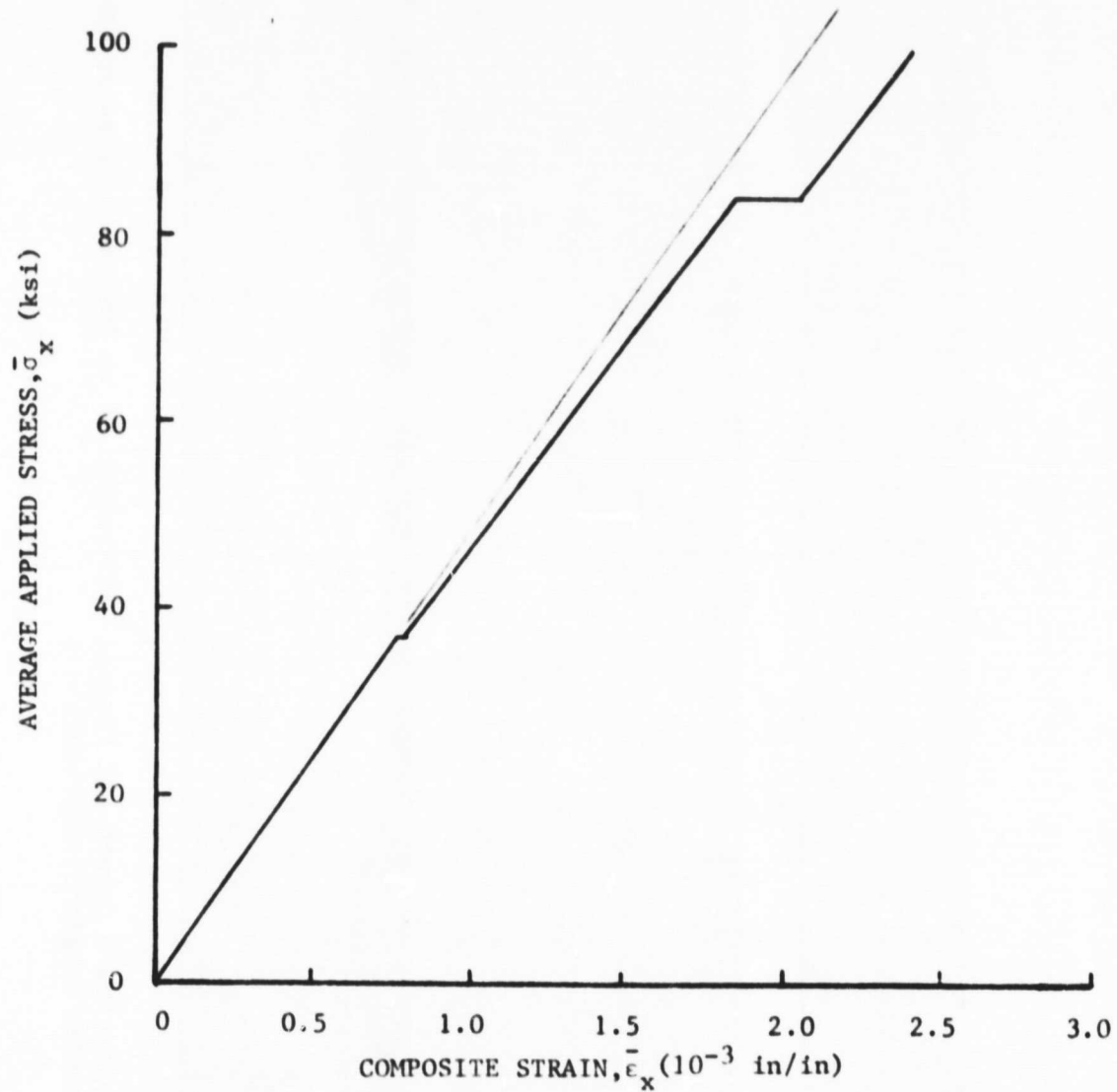


FIGURE 18. Plot of Applied Stress versus Composite Strain for the 90° Section Longitudinal Model, 33.3 Percent Discontinuous Fibers.

loss of effectiveness of the discontinuous fiber. However, this stiffness change is far less pronounced in the  $90^\circ$  section model, as would be expected with its much smaller initial crack formulation.

#### 6.4. Axial Loading of Longitudinal Models with 12.5 Percent Discontinuous Fibers

##### 6.4.1. Crack Initiation and Propagation in the $45^\circ$ Section Longitudinal Model

The  $45^\circ$  section longitudinal model was loaded axially with one boron fiber again treated as discontinuous. Plastic deformation around the stress concentration caused by the fiber discontinuity was first observed at an average applied stress level of 18.0 ksi. Loading was continued until an initial failure occurred at an applied stress level of 75.1 ksi, which is considerably higher than the 64.1 ksi level at which first failure occurred in the  $45^\circ$  model studied in Section 6.3.1. In addition, only one element failed, the crack tip being temporarily "blunted" by this failure. The state of stress in the aluminum matrix just prior to the initial failure is clearly illustrated in the contour plots in Figures 19 through 22. Although any or all of the various stress and strain components can be plotted by the computer program, contours of constant octahedral shear stress, octahedral shear strain, maximum principal stress, and in-plane shear stress have been selected here as being the most useful in studying the axial loading of unidirectional composites containing defects. Note that the octahedral shear stresses in Figure 19 have been normalized with respect to the octahedral shear yield strength of the 6061-T6 aluminum alloy. In this way, the region of plastic deformation can be readily discerned, as any contour value equal to one defines a plastic zone boundary.

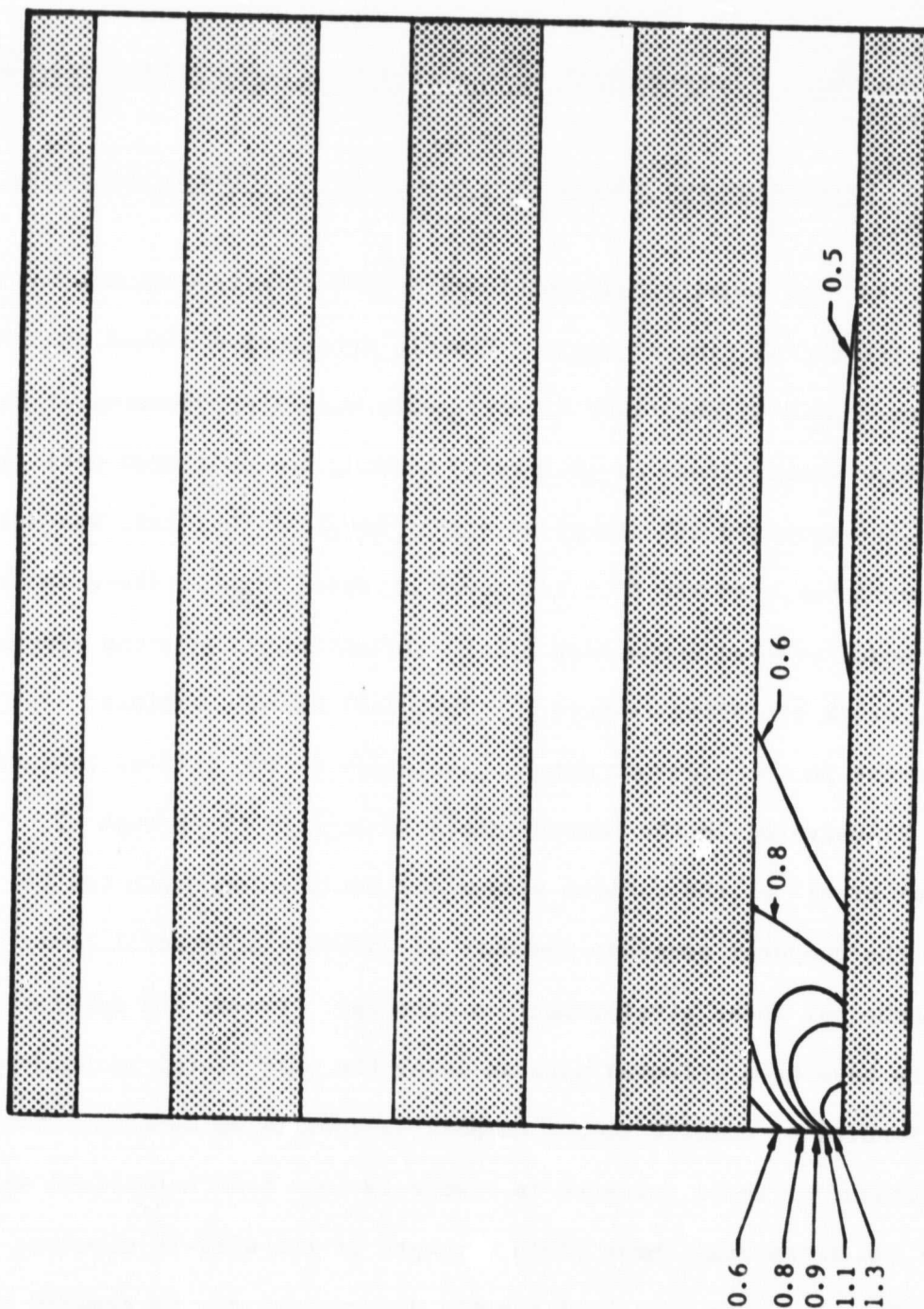


FIGURE 19. Contours of Constant Octahedral Shear Stress, Normalized by Dividing by the Matrix Yield Value of 17 ksi. Average Applied Stress,  $\bar{\sigma}_x = 75.1$  ksi.  $45^\circ$  Section Longitudinal Model.



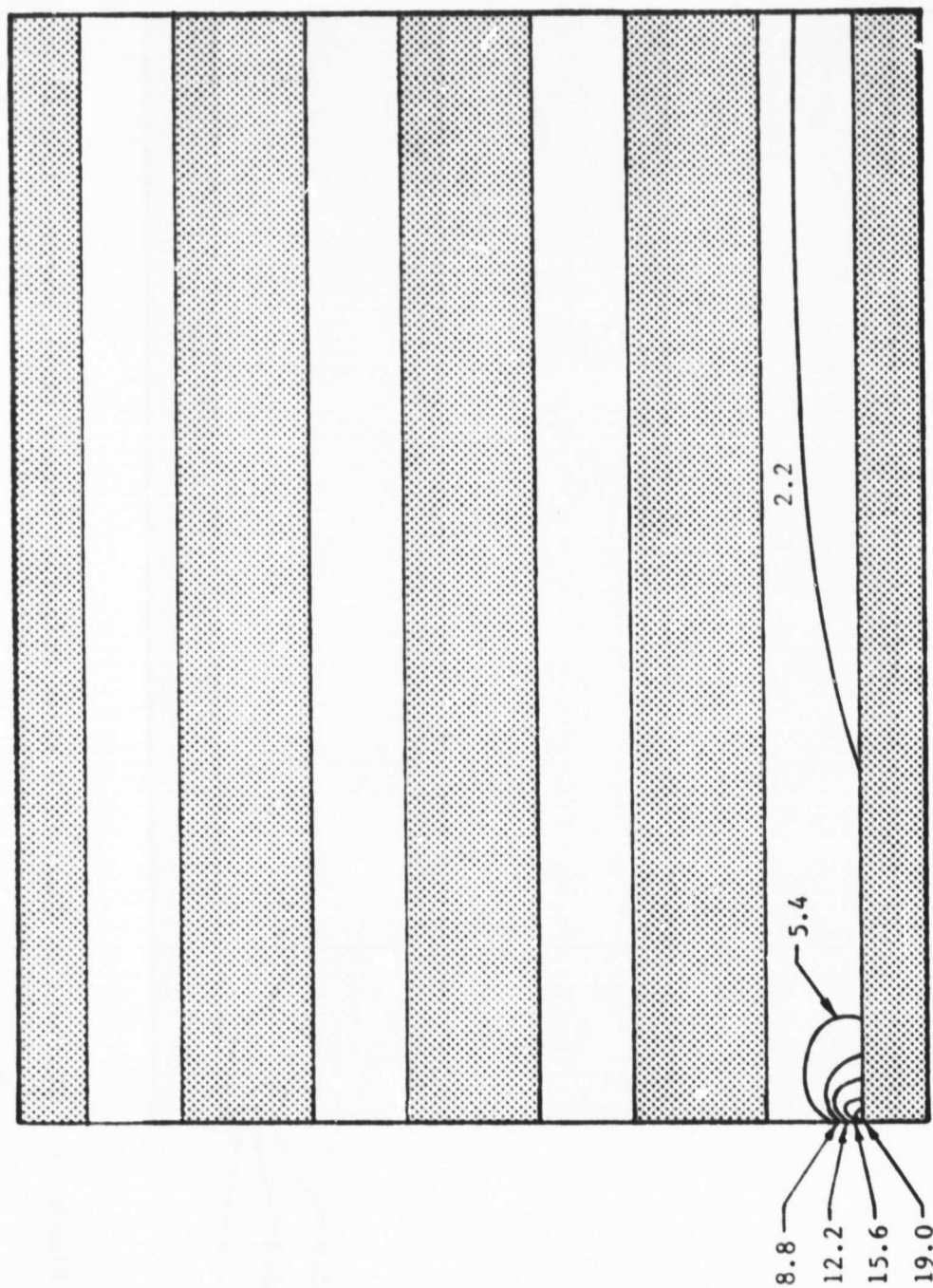


FIGURE 20. Contours of Constant Octahedral Shear Strain ( $10^{-3}$  in/in), Average Applied Stress,  $\bar{\sigma}_x = 75.1$  ksi,  $45^\circ$  Section Longitudinal Model.

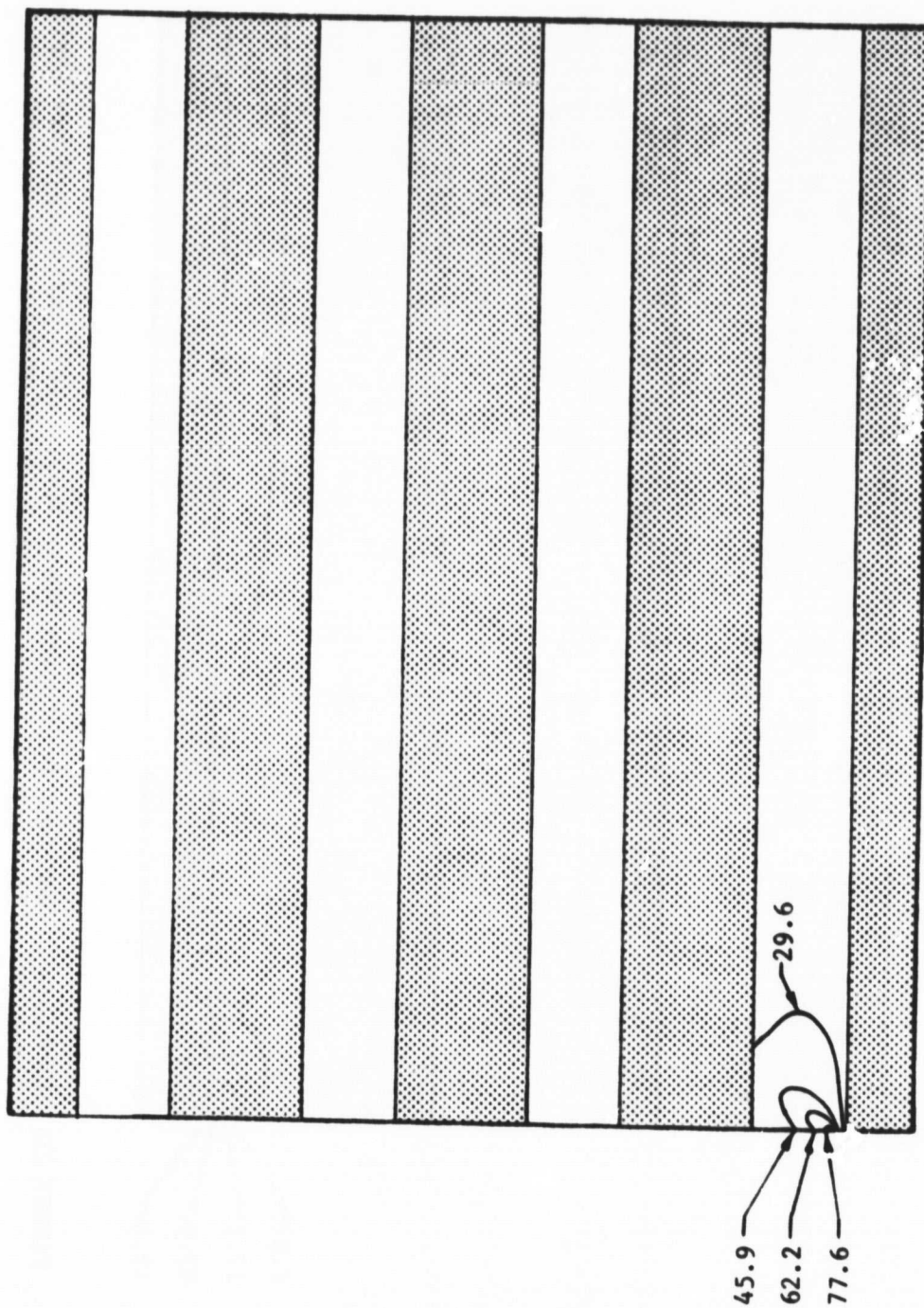


FIGURE 21. Contours of Constant Maximum Principal Stress (ksi), Average Applied Stress,  $\bar{\sigma}_x = 75.1$  ksi,  $45^\circ$  Section Longitudinal Model.

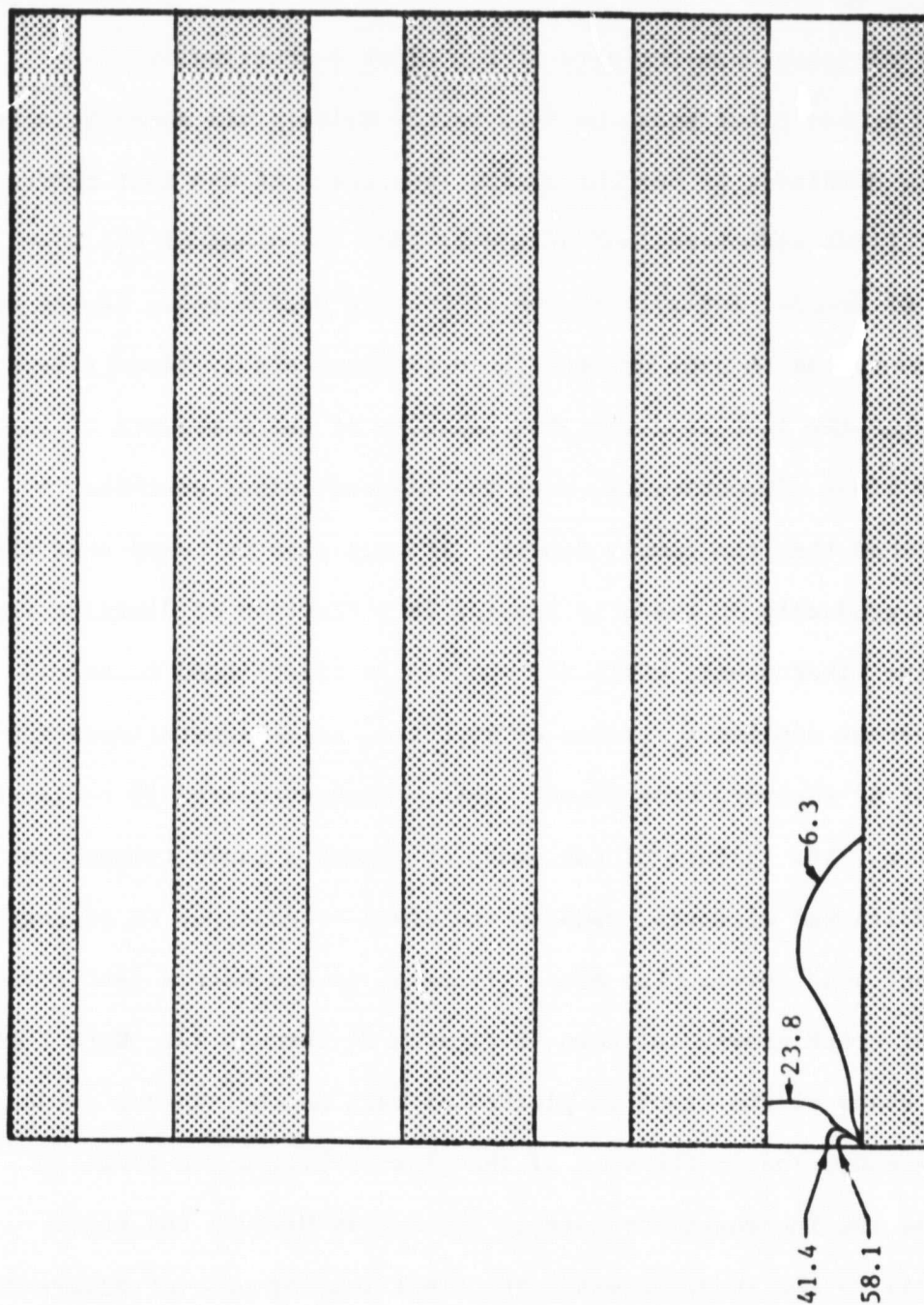


FIGURE 22. Contours of Constant In-Plane Shear Stress (ksi), Average Applied Stress,  $\bar{\sigma}_x = 75.1$  ksi, 45° Section Longitudinal Model.

It will be noted that at an average applied stress level of 75.1 ksi, the plastic zone is on the order of one fiber diameter in length. The state of stress in the fibers just prior to crack initiation is also of great interest; this is illustrated quite effectively in Figure 23. In this figure, the stress level of each of the fibers in the model is plotted as a function of distance from the site of the fiber discontinuity. As expected, the broken fiber picks up load fairly quickly via shearing stresses in the matrix, attaining 89 percent of the load level of the most remote fibers at 8.2 fiber diameters (end of model) from the plane of the discontinuity. Of special interest is the affect the broken fiber has on its nearest neighbor, and to some extent, the next fiber also. These fibers must make up for the lost load carrying capacity of the composite in the region of the fiber discontinuity, with the adjacent fiber carrying 10 percent more load than the remote fibers. It will also be noted that the remote fibers gradually increase in loading as a function of distance from the site of the fiber break, while the two closer fibers tend to unload.

At an average applied  $\bar{\sigma}_x$  stress of 76.0 ksi, crack growth involving the failure of 82 elements took place. This process required 16 redistribution steps, i.e., the failure of one group of elements would trigger the failure of additional elements, causing the crack to continue to propagate at the constant load level. The state of stress in the matrix just after this period of crack growth is shown in Figures 24 through 27. Note that the size and shape of the crack is plotted as well as the contour values. Note also the reduction in the size of the plastic region, as shown in Figure 24, and the increased stresses in the matrix between the other fibers, especially the shear stress. The fiber loading plot of Figure 28

69-66

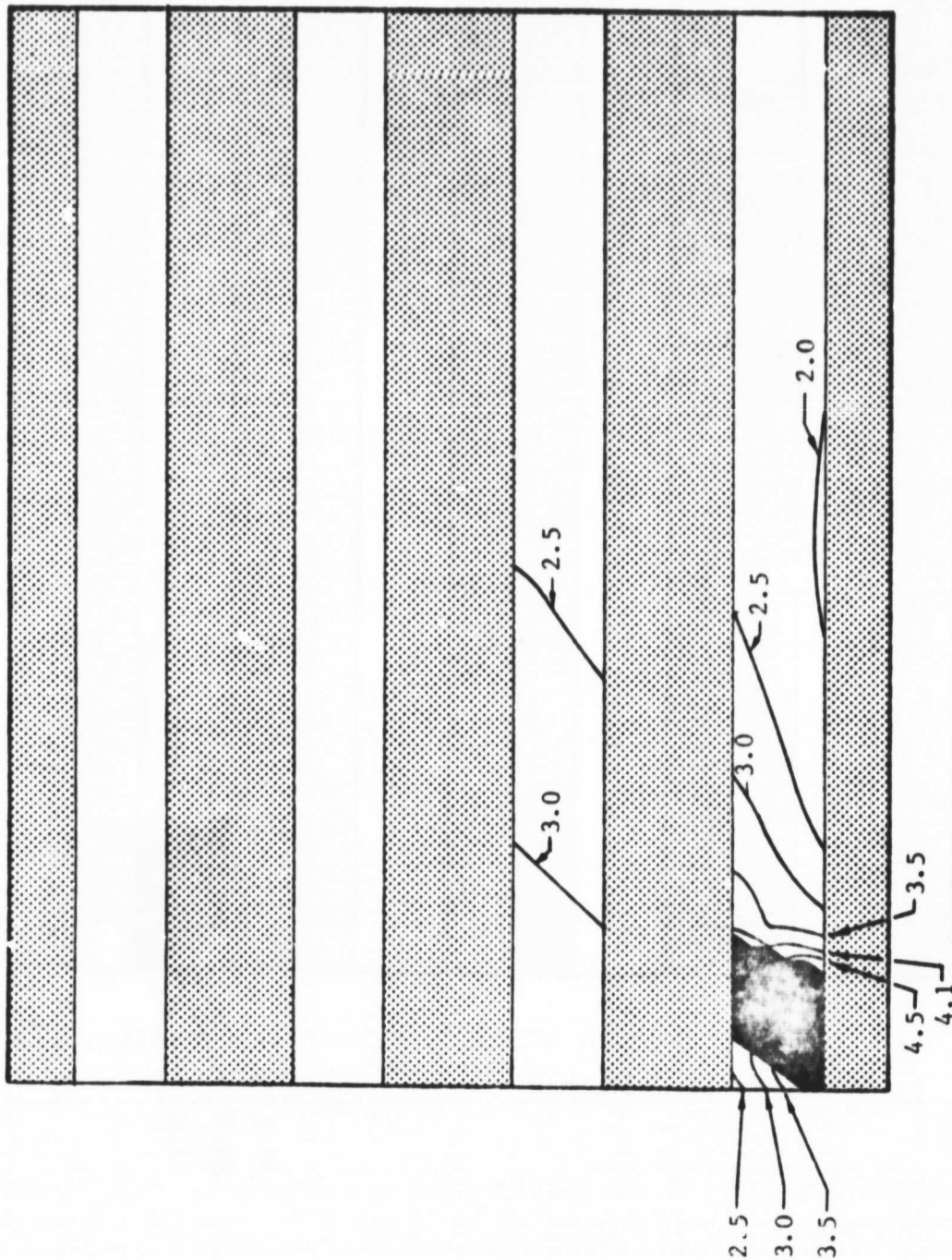


FIGURE 25. Contours of Constant Octahedral Shear Strain ( $10^{-3}$  in/in), Average Applied Stress,  $\bar{\sigma}_x = 76.0$  ksi,  $45^\circ$  Section Longitudinal Model.



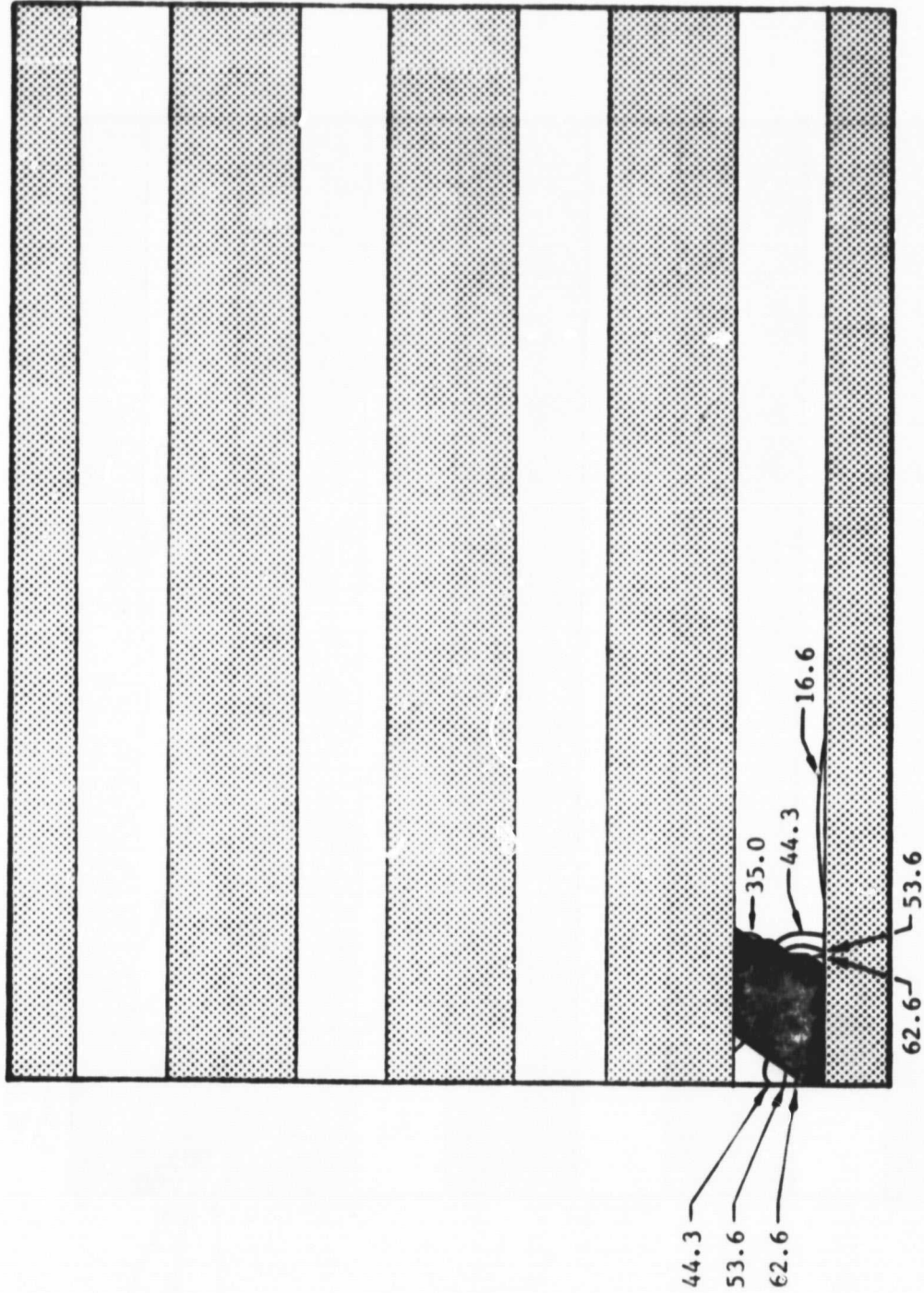


FIGURE 26. Contours of Constant Maximum Principal Stress (ksi), Average Applied Stress,  $\sigma_x = 76.0$  ksi,  $45^\circ$  Section Longitudinal Model.

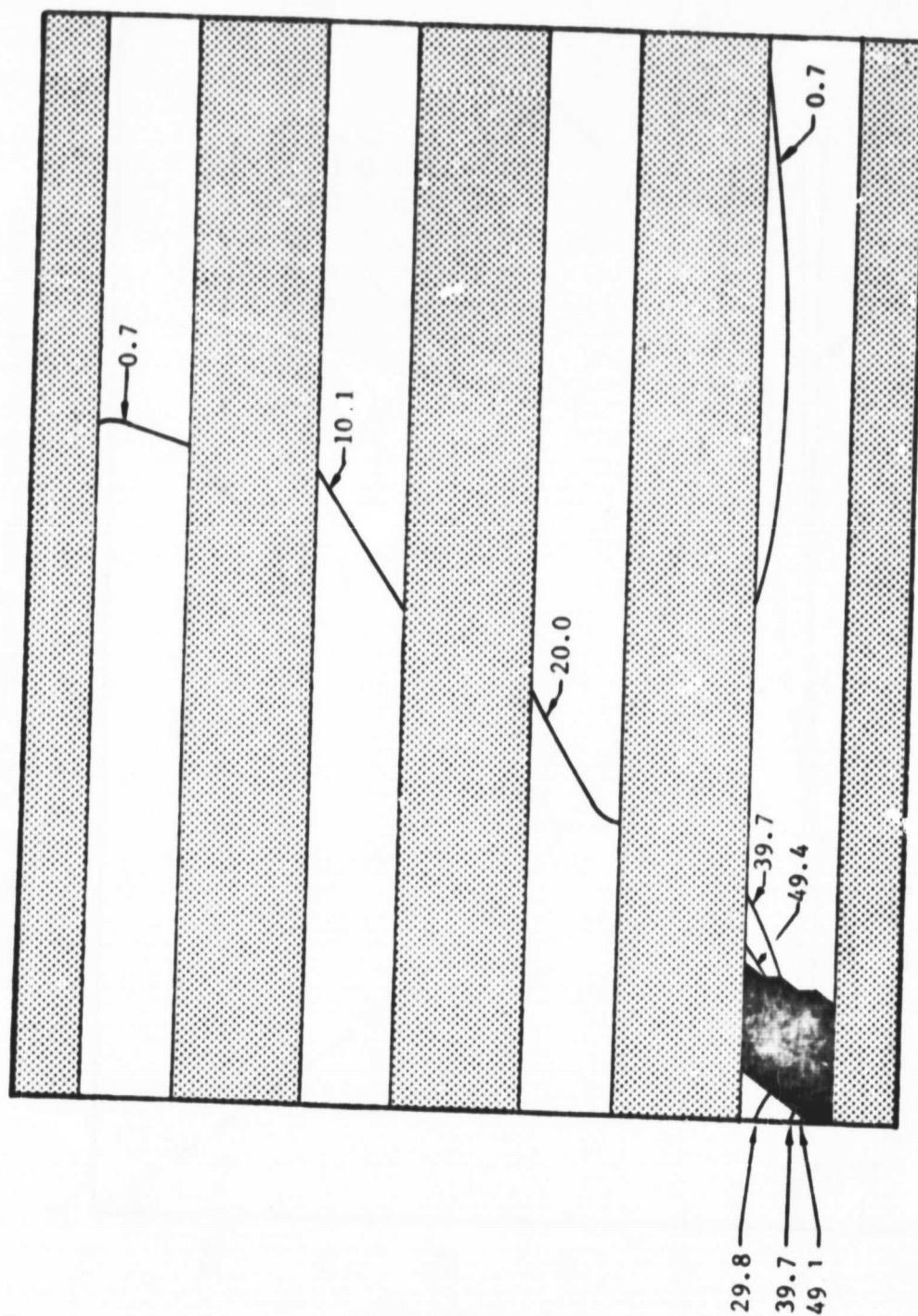


FIGURE 27. Contours of Constant In-Plane Shear Stress (ksi), Average Applied Stress,  $\bar{\sigma}_x = 76.0$  ksi,  $45^\circ$  Section Longitudinal Model.





corresponds to the state of stress and deformation of Figures 24 through 27, and the most change caused by the element failures appears to be the reduced loading of the broken fiber. While it is still loaded to almost the same percent at the right boundary of the model, the slope of its loading curve is somewhat less near the break site.

The next set of figures, Figures 29 through 33, are plots corresponding to an average applied stress of 97.4 ksi. At this load level, further crack growth was immanent. It will be noted that the region of plastic deformation has enlarged considerably, and that the loading of the broken fiber at 8.2 fiber diameters from the plane of discontinuity is now only 86 percent of the load carried by the two most remote fibers, Fibers 4 and 5. An increase in the load resulted in only one additional element failure, however, and crack propagation did not resume until an average stress level of 183 ksi had been attained.

At an applied composite stress of 183 ksi, crack propagation involving 169 elements and 11 stages of growth at constant stress occurred. The results of this growth are illustrated in Figures 34 through 38. What is most significant about this stage of the loading of this model is that the extensive growth of the primary crack has resulted in such a high, localized stress in the adjacent fiber that two large matrix elements between it and the next intact fiber have ruptured. As Figure 38 illustrates, the adjacent fiber (Fiber 2) is now carrying about 14 percent more stress than Fibers 4 and 5, and appears destined to fail well before Fibers 3, 4, and 5.

The 45° section longitudinal model continued to absorb loading up to an average stress level of 208.5 ksi with no further failures. The analysis was terminated at this point. In Figure 39, the stress-strain plot of the

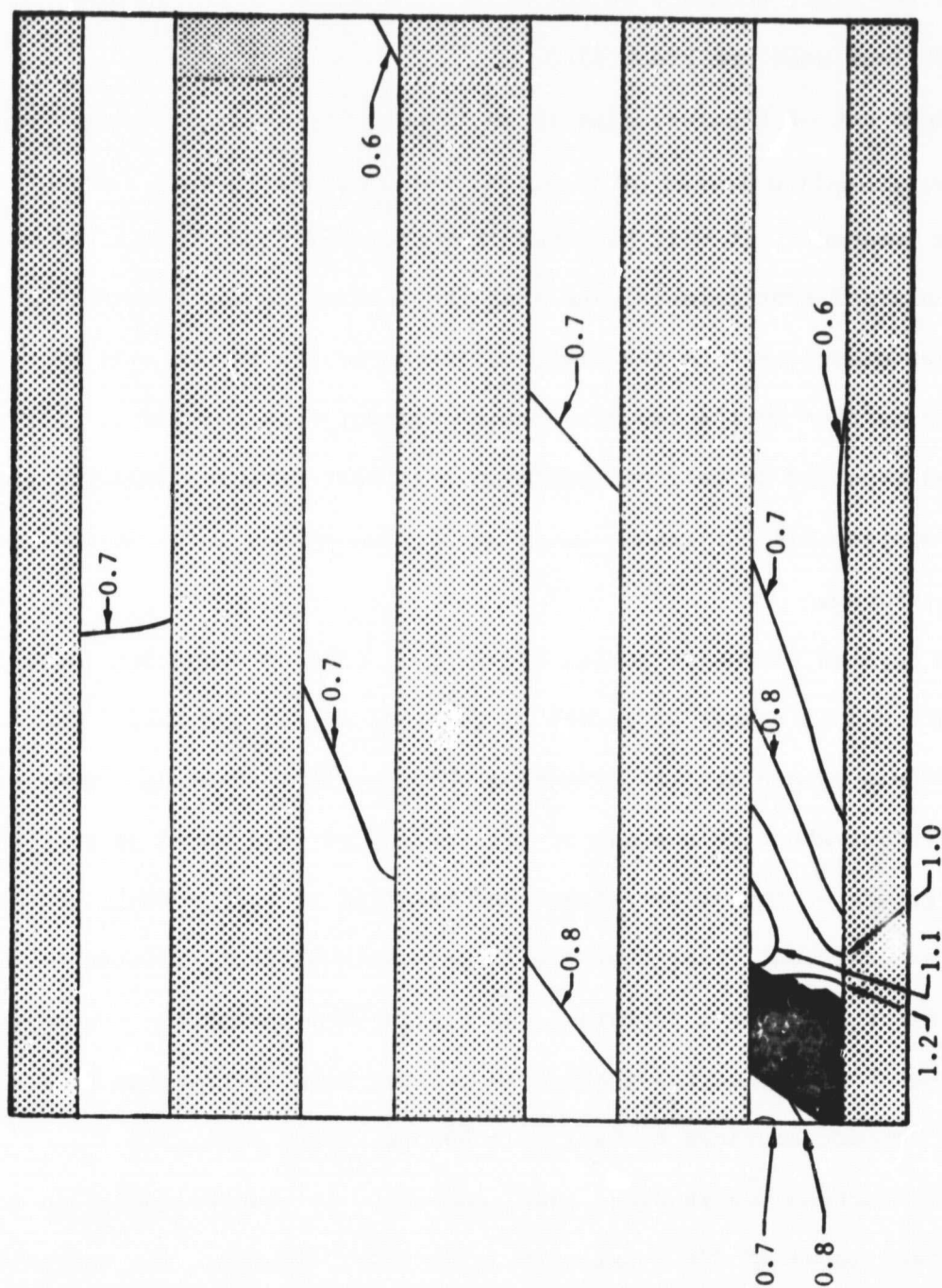


FIGURE 29. Contours of Constant Octahedral Shear Stress, Normalized by Dividing by the Matrix Yield Value of 17 ksi. Average Applied Stress,  $\bar{\sigma}_x = 97.4$  ksi,  $45^\circ$  Section Longitudinal Model.

ORIGINAL PAGE IS  
OF POOR QUALITY

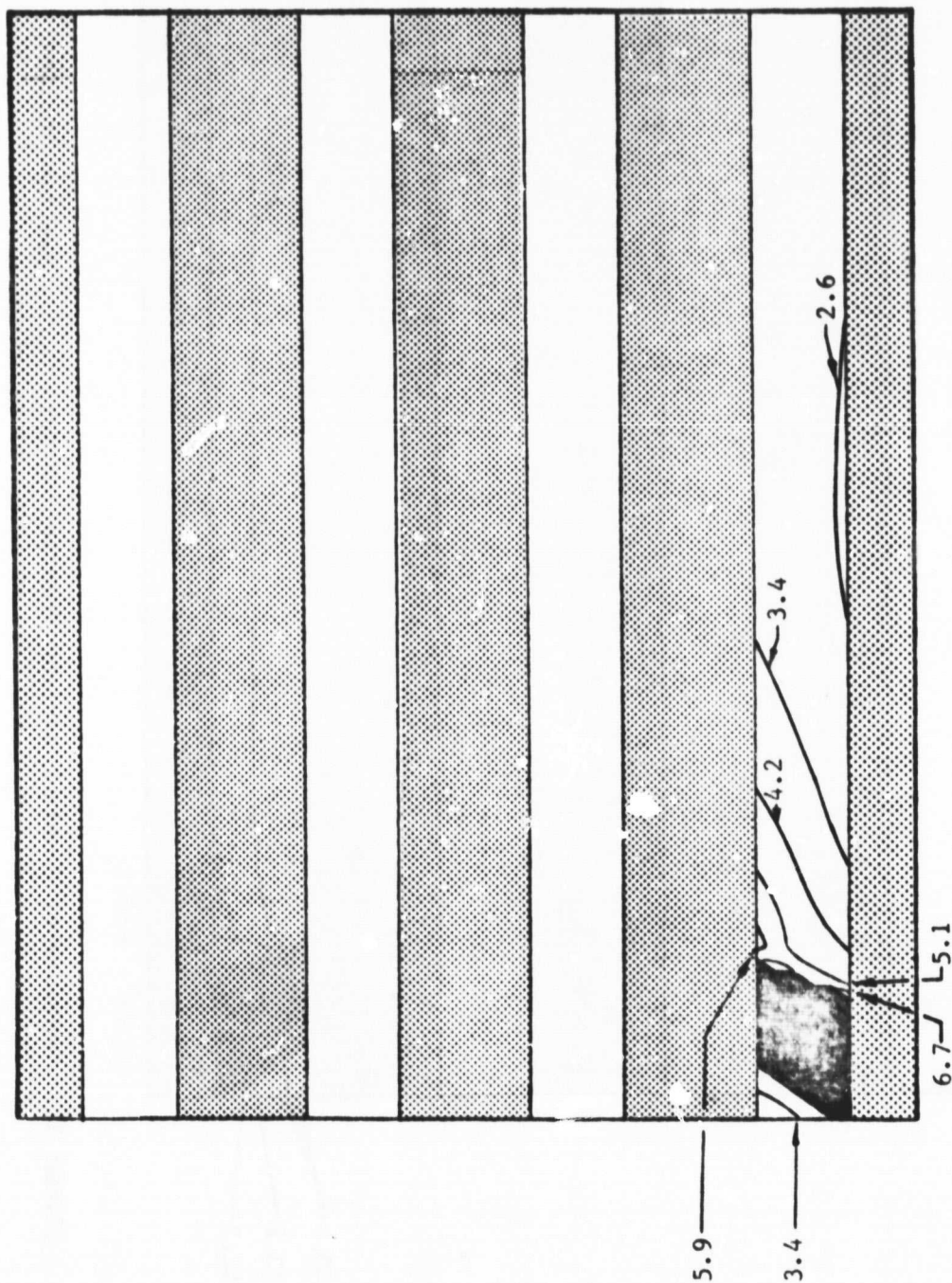


FIGURE 30. Contours of Constant Octahedral Shear Strain ( $10^{-3}$  in/in), Average Applied Stress,  $\bar{\sigma}_x = 97.4$  ksi,  $45^\circ$  Section Longitudinal Model.



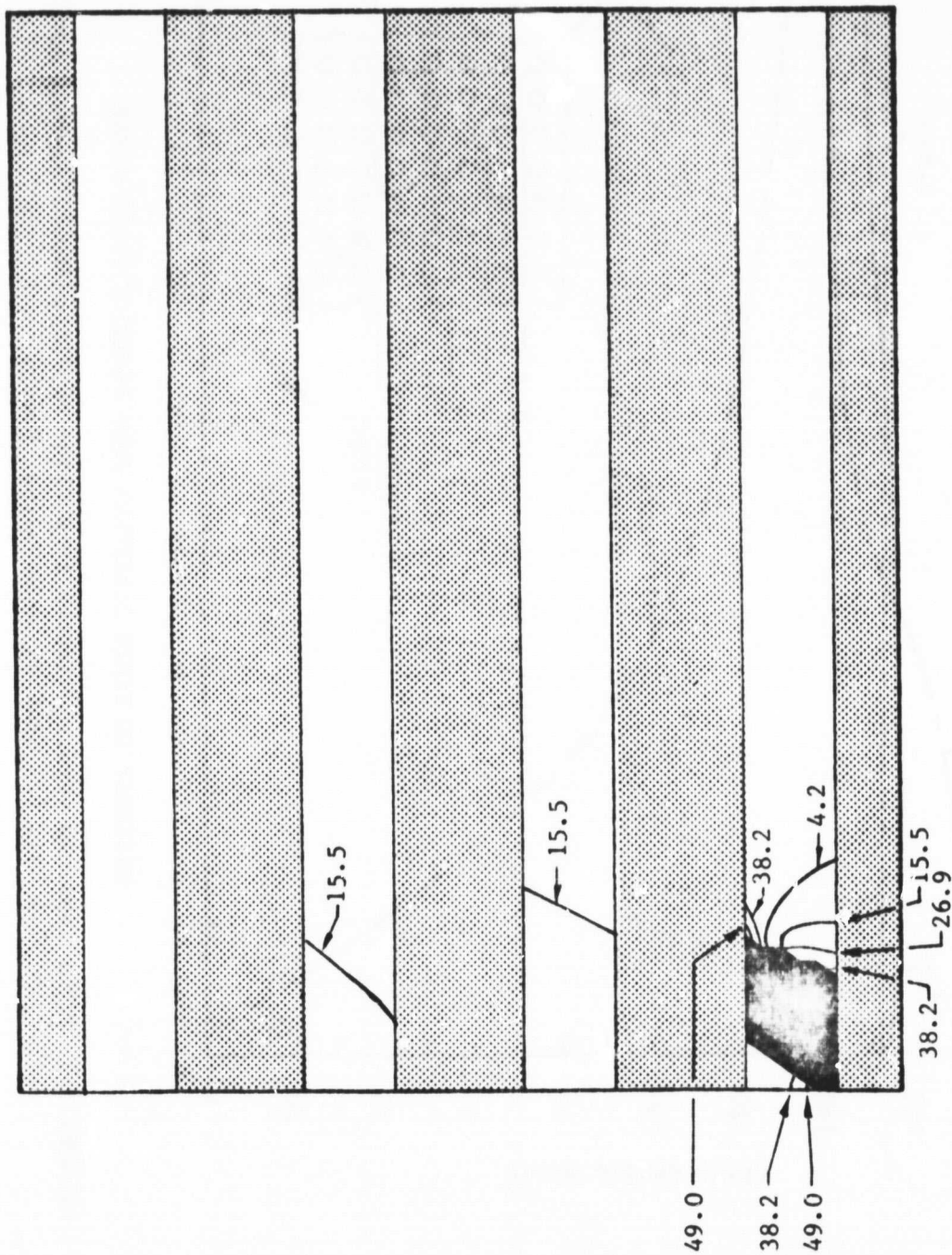


FIGURE 32. Contours of Constant In-Plane Shear Stress (ksi), Average Applied Stress,  $\bar{\sigma}_x = 97.4$  ksi,  $45^\circ$  Section Longitudinal Model.



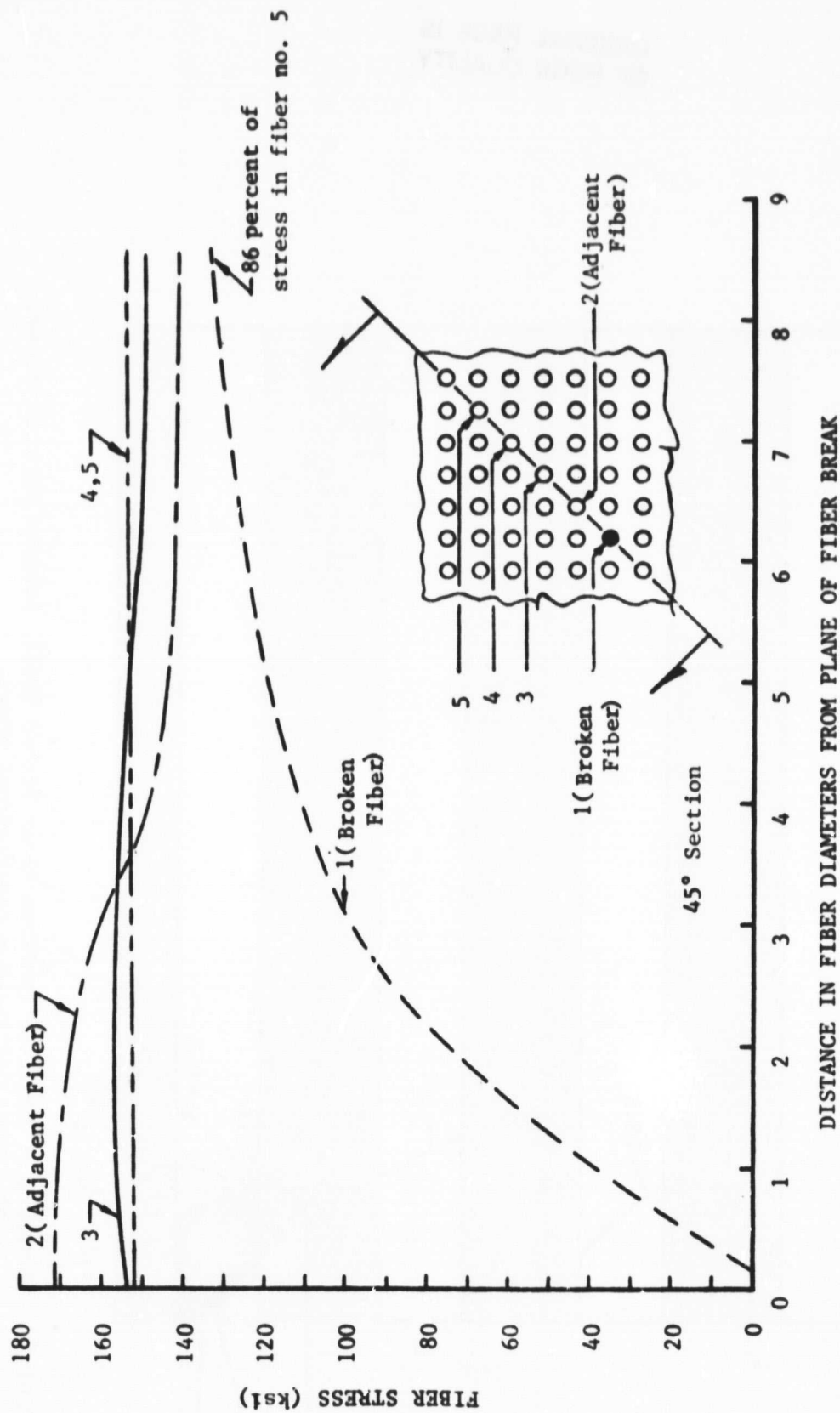


FIGURE 33. Fiber Loadings versus Distance from Plane of Fiber Break, Average Applied Stress,  $\bar{\sigma}_x = 97.4$  ksi, 45° Section Longitudinal Model.

ORIGINAL PAGE IS  
OF POOR QUALITY

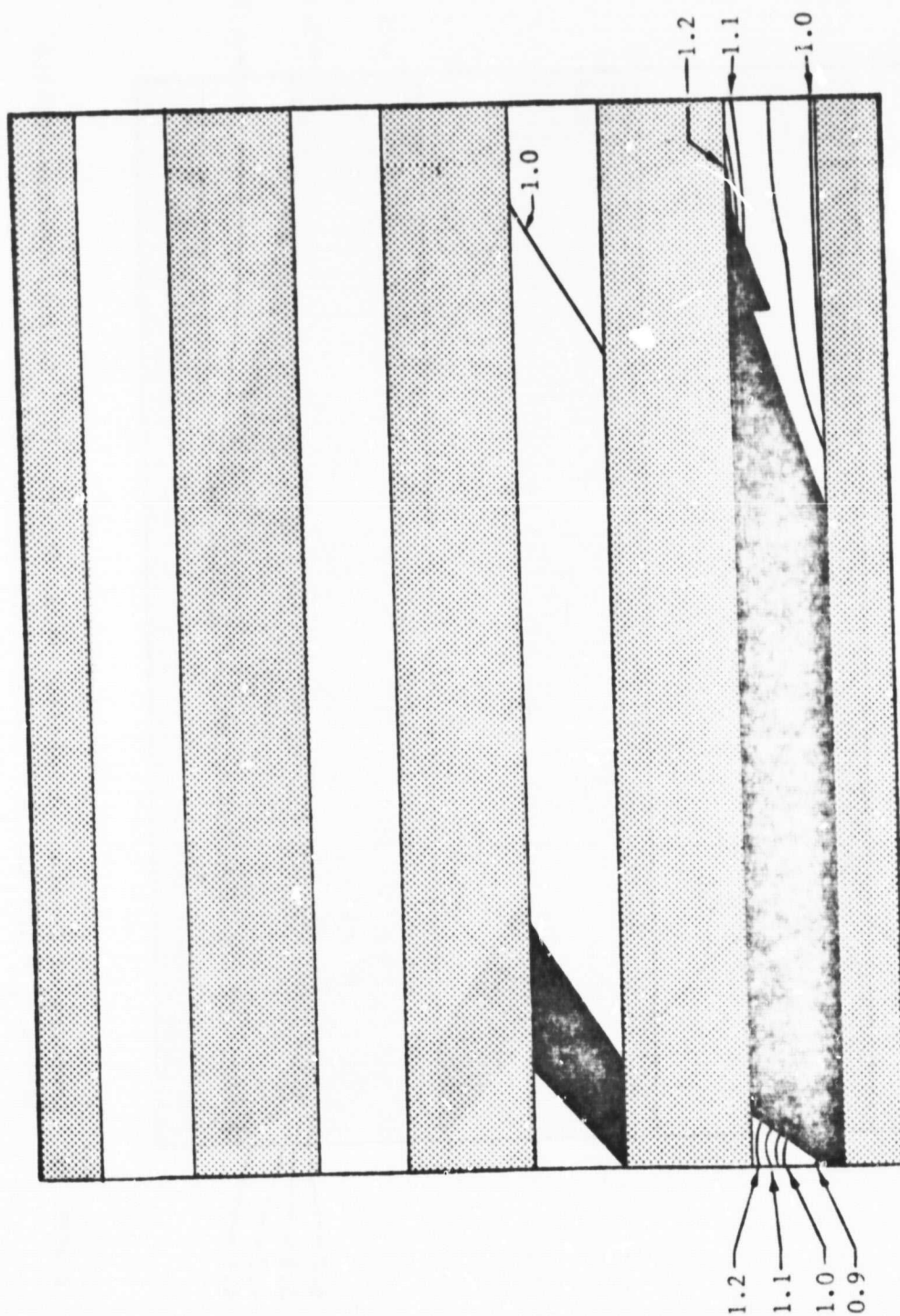


FIGURE 34. Contours of Constant Octahedral Shear Stress, Normalized by Dividing by the Matrix Yield Value of 17 ksi, Average Applied Stress,  $\bar{\sigma}_x = 183$  ksi,  $45^\circ$  Section Longitudinal Model.

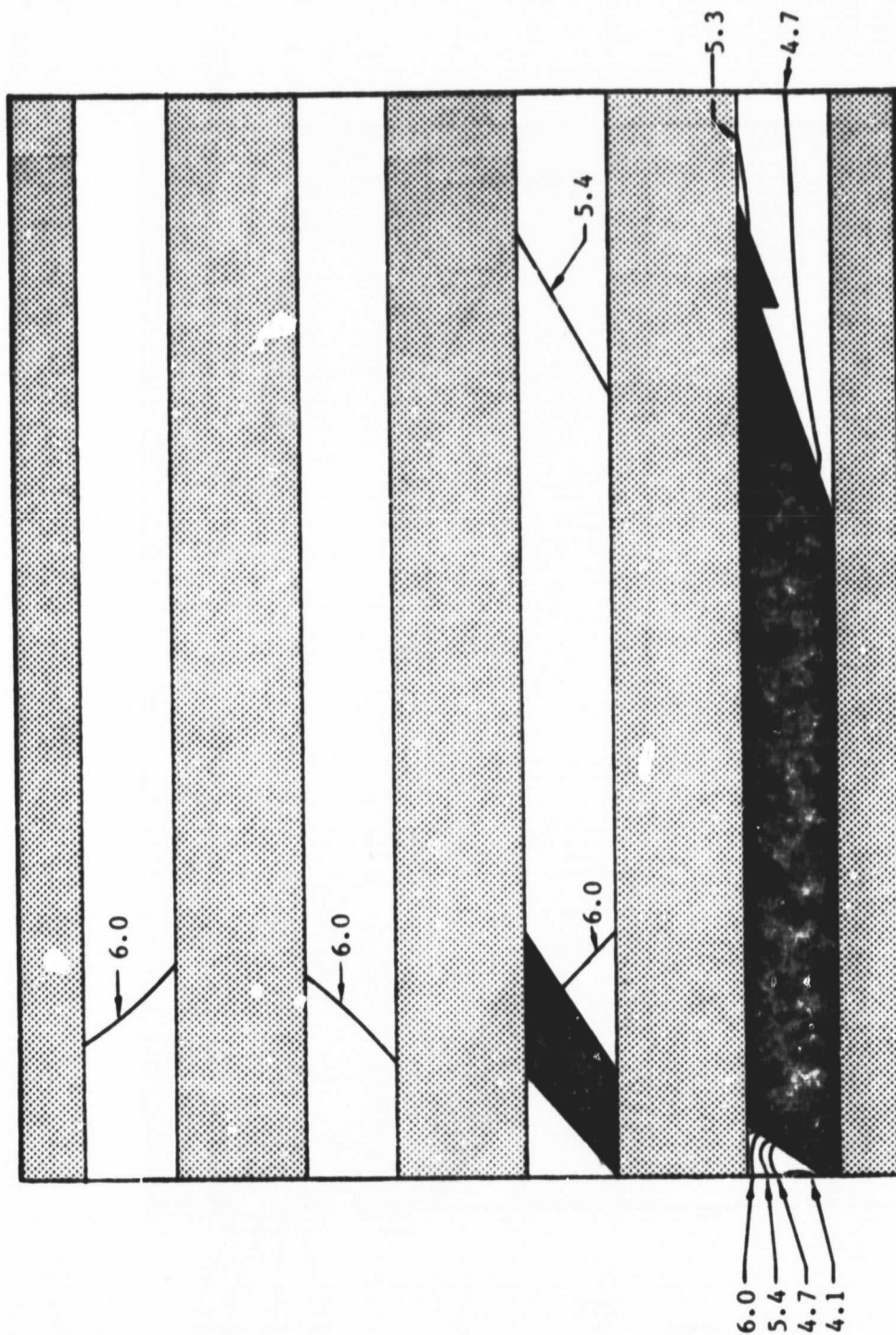


FIGURE 35. Contours of Constant Octahedral Shear Strain ( $10^{-3}$  in/in), Average Applied Stress,  $\bar{\sigma}_x = 183$  ksi,  $45^\circ$  Section Longitudinal Model.



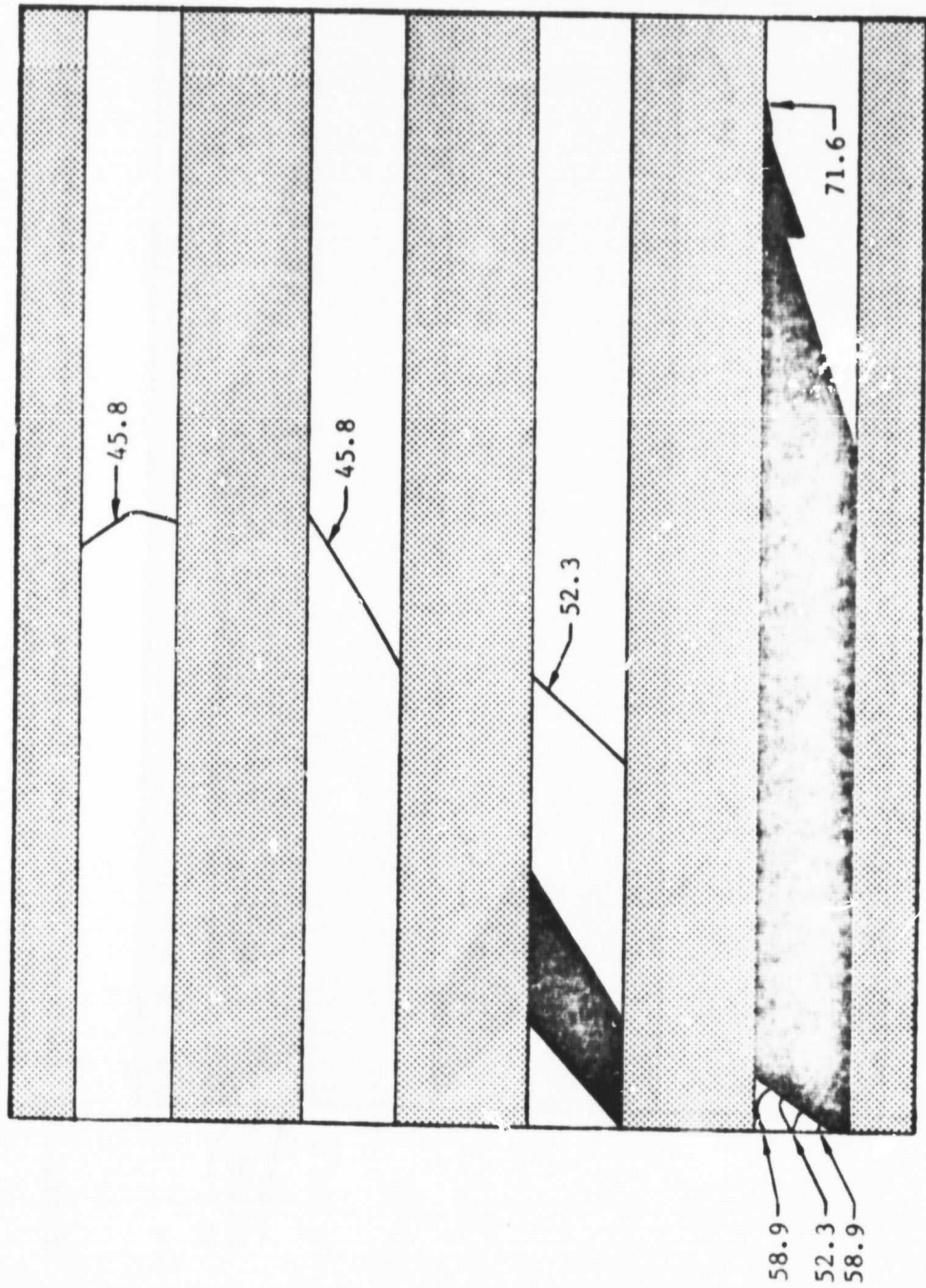


FIGURE 36. Contours of Constant Maximum Principal Stress (ksi), Average Applied Stress,  $\bar{\sigma}_x = 183$  ksi, 45° Section Longitudinal Model

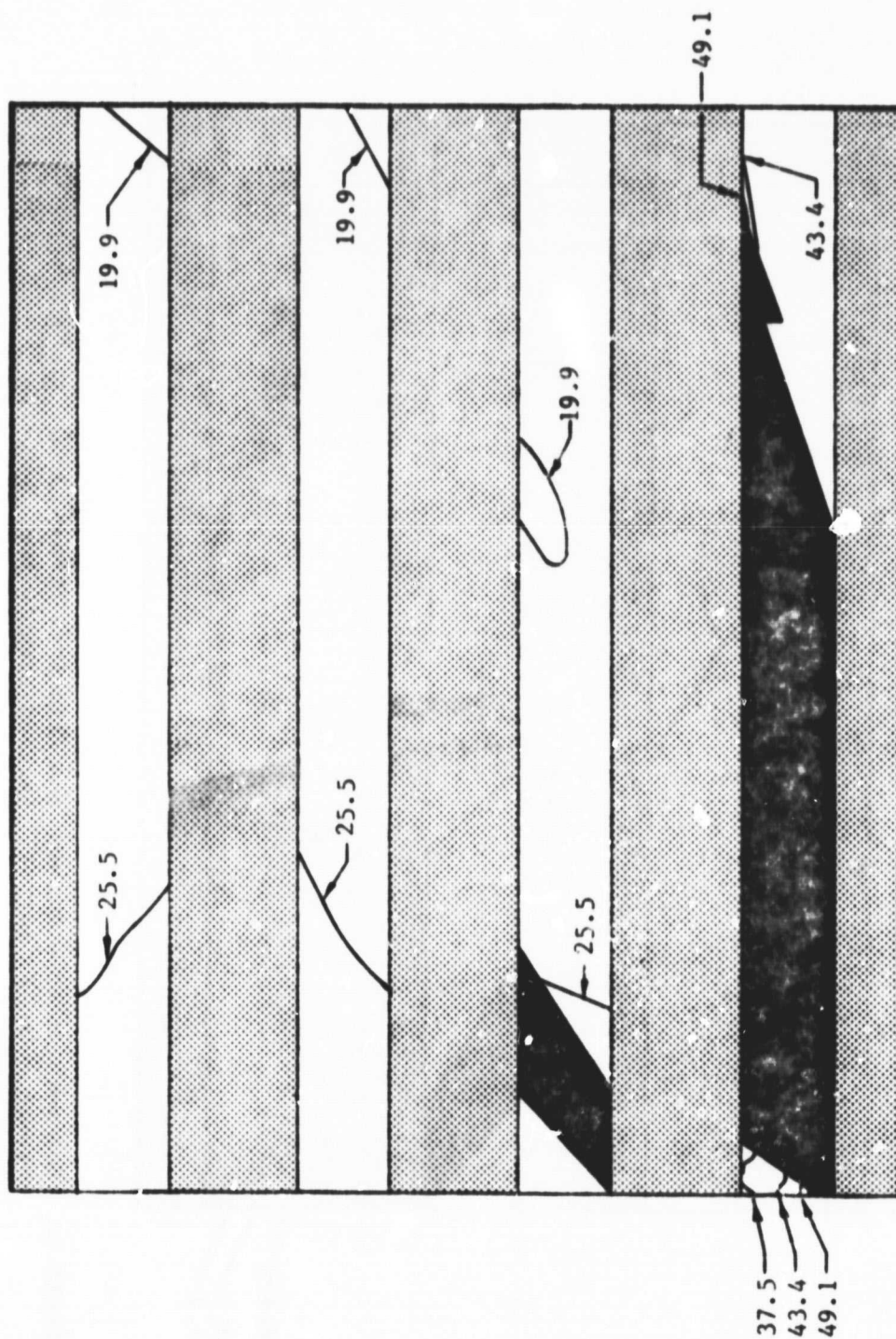


FIGURE 37. Contours of Constant In-Plane Shear Stress (ksi), Average Applied Stress,  $\bar{\sigma}_x = 183$  ksi,  $45^\circ$  Section Longitudinal Model.

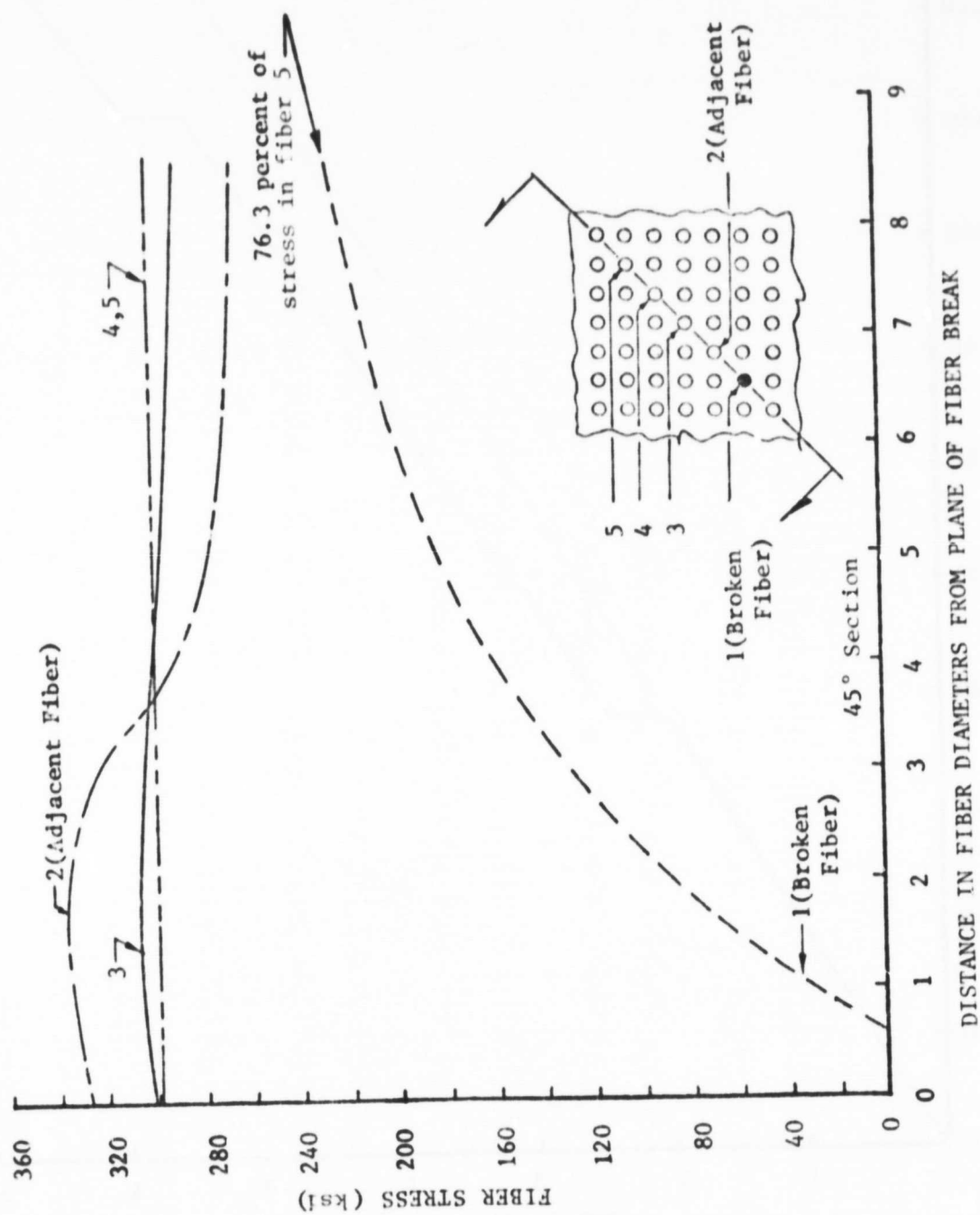


FIGURE 38. Fiber Loadings versus Distance from Plane of Fiber Break, Average Applied Stress,  $\bar{\sigma}_x = 183$  ksi, 45° Section Longitudinal Model.

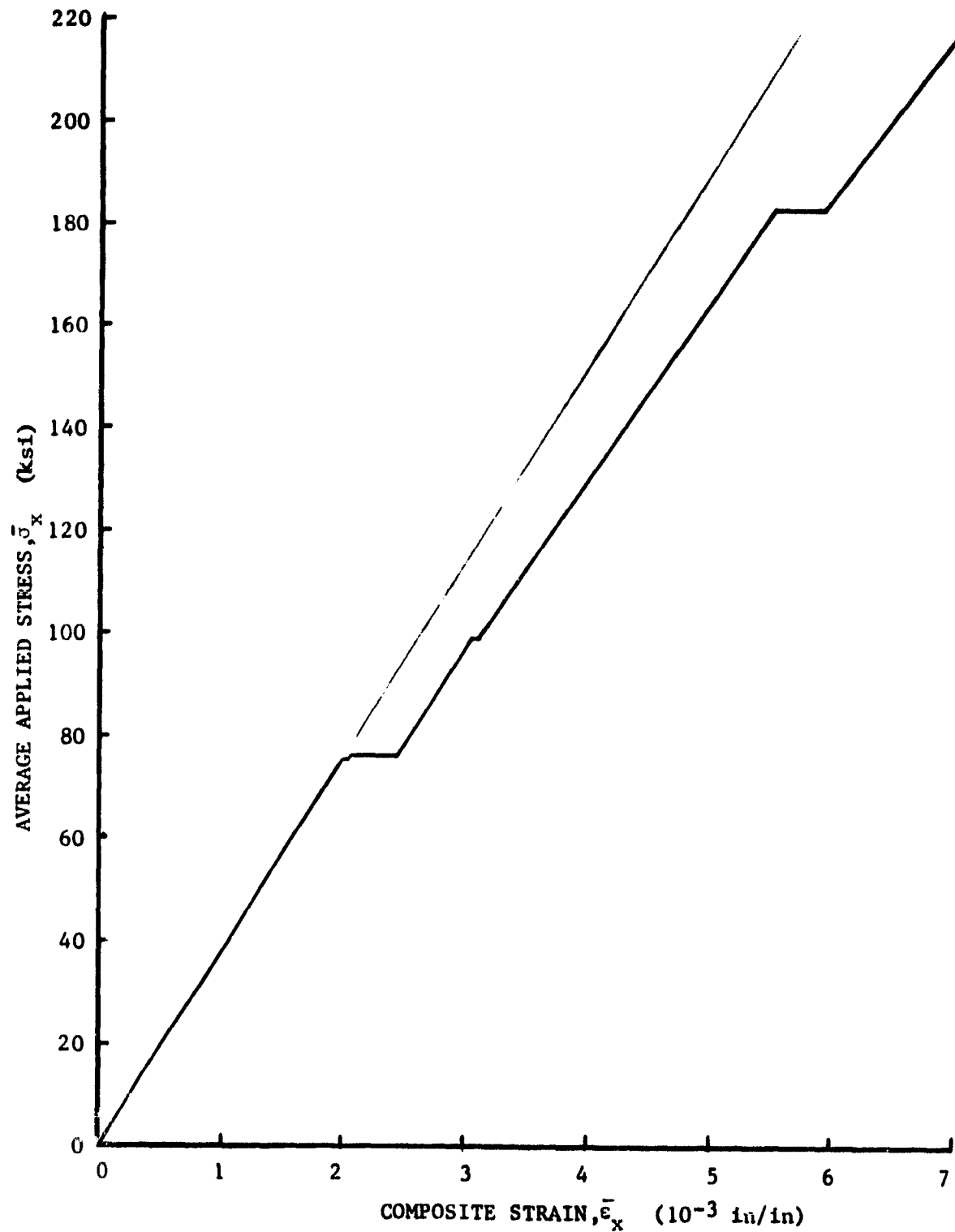


FIGURE 39. Plot of Applied Stress versus Composite Strain for the 45° Section Longitudinal Model, 12.5 Percent Discontinuous Fibers.

total composite is presented, reflecting the occurrences of crack propagation and the associated decreases in composite modulus.

The process of modeling stress redistributions due to crack growth involves many cycles of the numerical solution procedure, and when this is coupled to the incremental loading of an analytical model which experiences localized plastic deformation at a small fraction of its total load capacity, computer time requirements become very large. For example, the analysis of the 45° longitudinal section model discussed in this section required 9,577 seconds of running time on the CDC Cyber 760 computer and 372 thousand words of core storage. When one considers that, in the present example, plastic deformation began at an applied stress level of 18 ksi, and at  $\bar{\sigma}_x = 208.5$  ksi total failure had not yet occurred, the complexity of the problem being analyzed can be appreciated.

#### 6.4.2. Crack Initiation and Propagation in the 90° Section Longitudinal Model

The 90° section longitudinal model was loaded to a maximum of 208.3 ksi, during which five periods of crack growth were observed, but catastrophic failure of the composite did not occur. In the discussion that follows, contour plots and fiber loading diagrams are presented to illustrate some of the more interesting points in the loading history of this model. While a great many similarities between the response of the 45° and 90° section longitudinal models exist, a careful comparison will indicate the differences in crack growth pattern, stress distributions, fiber loading, and load levels at which they occur. Such a comparison confirms the fact that there is a strong dependence of the results on fiber spacing when plastic deformation and crack growth are considered.

This dependence is what makes the use of a two-dimensional formulation so difficult to correlate to actual conditions, as there is no practical way of manufacturing most unidirectional composites in which every fiber is equidistant from each of its nearest neighbors. As was discussed in Section 4.1, it is possible that specialized test specimens, used in conjunction with the axisymmetric analysis, could lead to the determination of an average, i.e., effective, fiber spacing, thus allowing the present generalized plane strain formulation to more accurately model square and rectangular fiber arrays.

Because of its much higher apparent fiber volume, shear loading of the matrix between the broken fiber and its nearest neighbor in the  $90^\circ$  section longitudinal model is more severe than in the  $45^\circ$  section longitudinal model. As a result, the initial stress concentration caused by the broken fiber is more pronounced, and initial element failure in the  $90^\circ$  section model was observed before a plastic region of any significant extent could form around the crack tip. This failure occurred at an average applied stress level of 24.9 ksi. The matrix stress contour plots for the composite just prior to this event are presented in Figures 40 through 43. The single element failure at this applied stress level appears to have very effectively "blunted" the crack, as the next failure did not occur until an average applied stress level of 84.0 ksi had been attained. At this point, one additional element failed, again temporarily blunting the crack. Figures 44 through 48 illustrate the state of stress in the matrix and the loading of the various fibers at this load level just prior to the failure of the second element. At this point there is a fairly extensive zone of plastic deformation around the

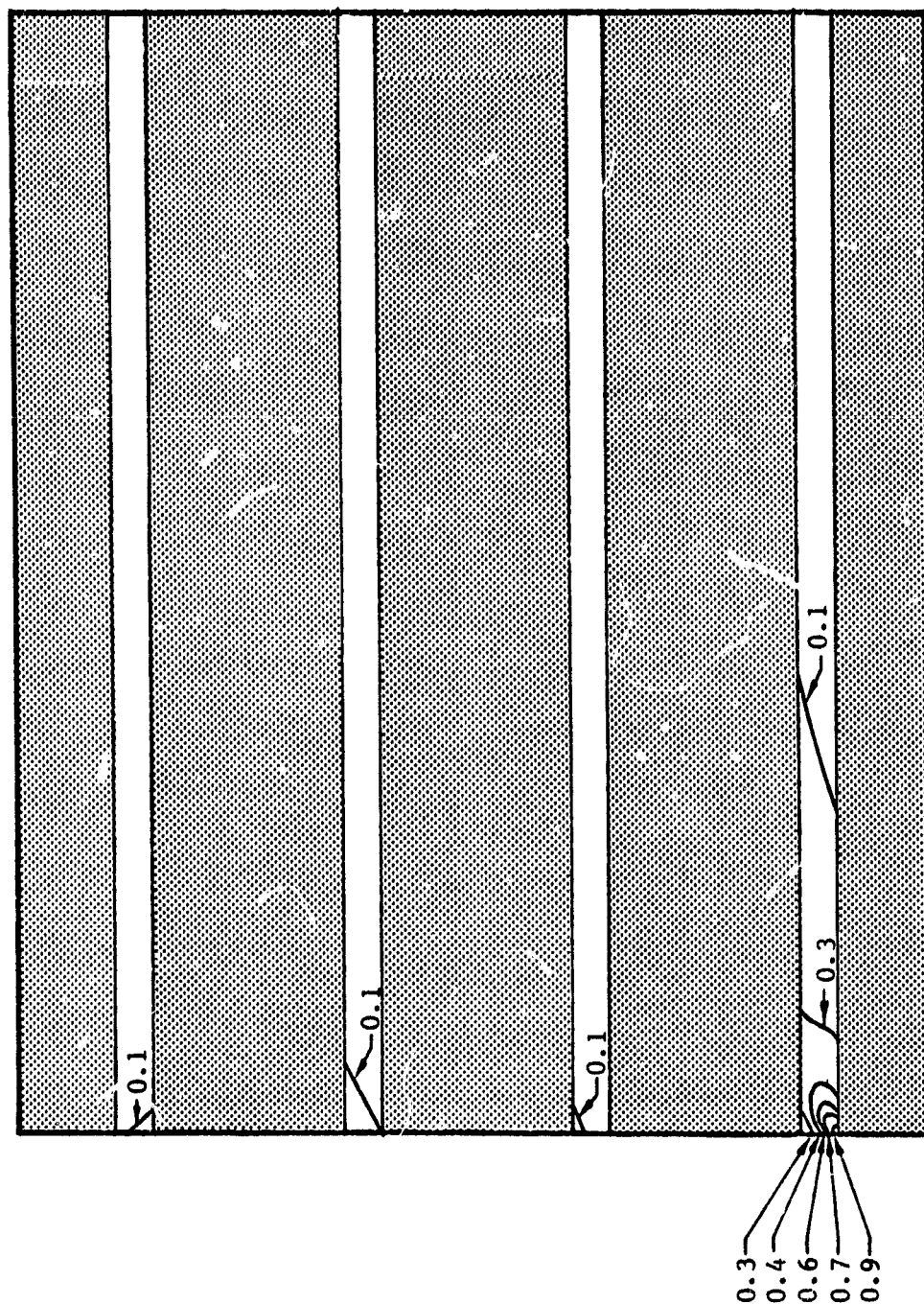


FIGURE 40. Contours of Constant Octahedral Shear Stress, Normalized by Dividing by the Matrix Yield Value of 17 ksi, Average Applied Stress,  $\bar{\sigma}_x = 24.9$  ksi,  $90^\circ$  Section Longitudinal Model.

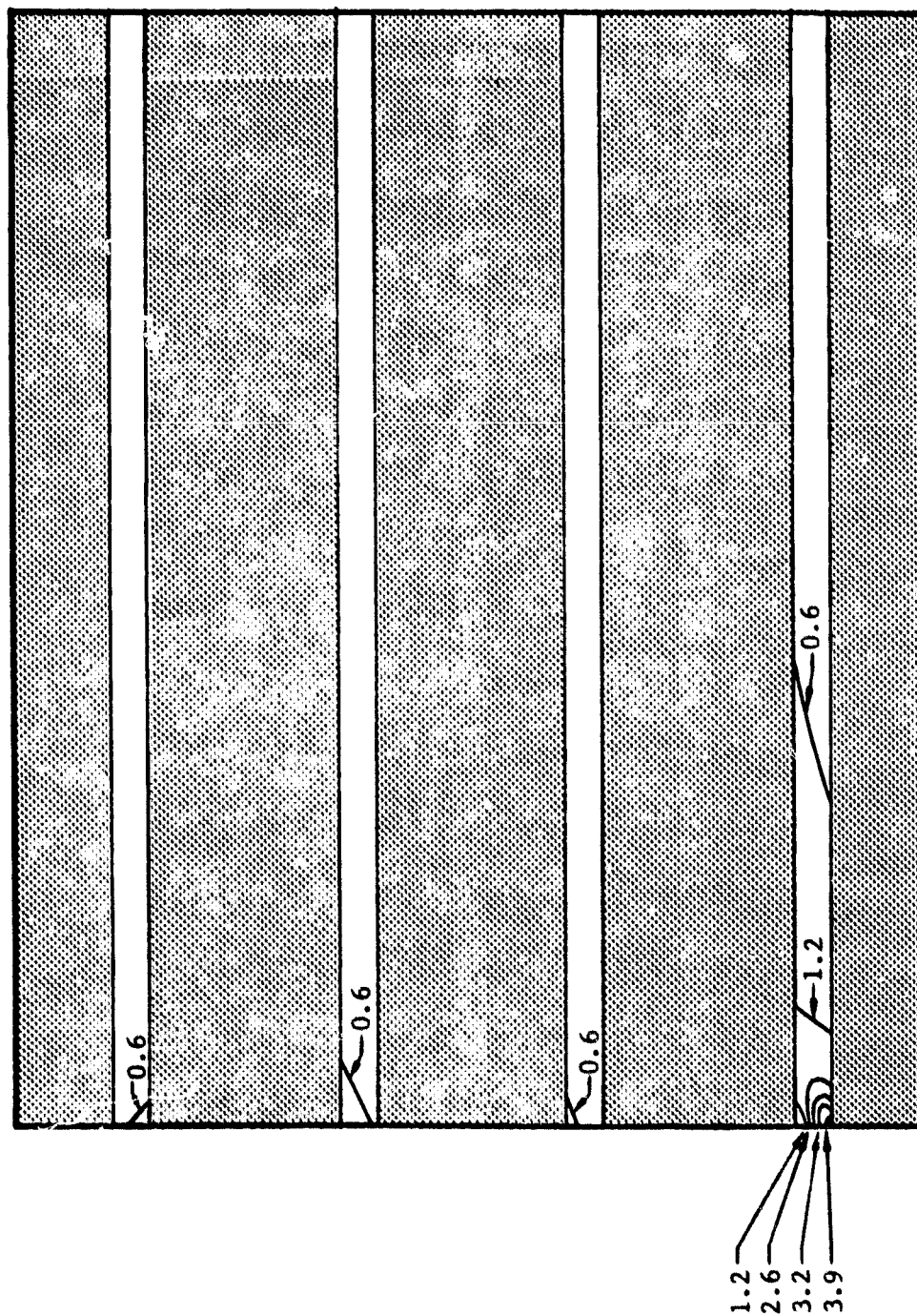


FIGURE 41. Contours of Constant Octahedral Shear Strain ( $10^{-3}$  in/in), Average Applied Stress,  $\bar{\sigma}_x = 24.9$  ksi,  $90^\circ$  Section Longitudinal Model.



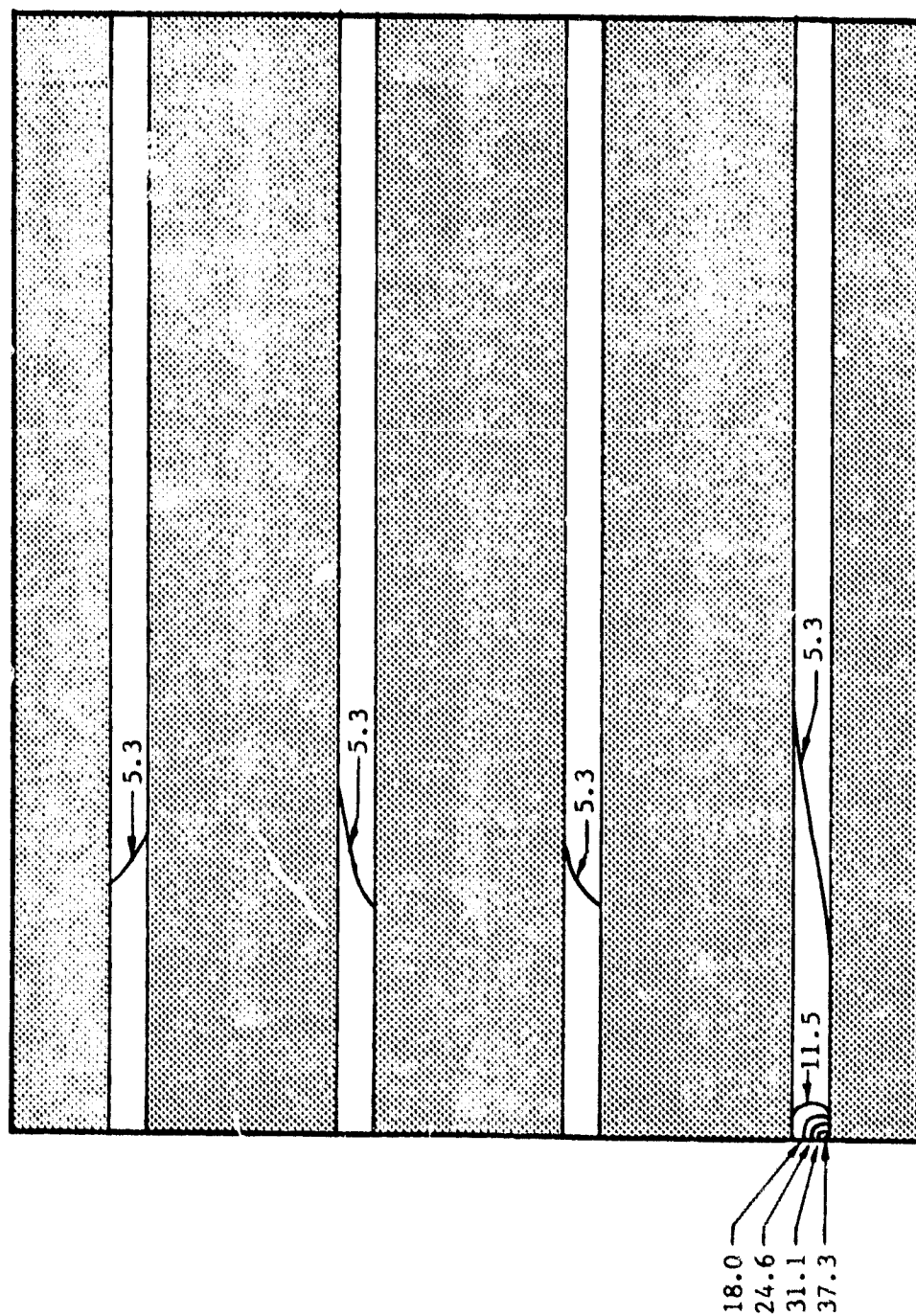


FIGURE 42. Contours of Constant Maximum Principal Stress (ksi), Average Applied Stress,  $\bar{\sigma}_x = 24.9$  ksi, 90° Section Longitudinal Model.

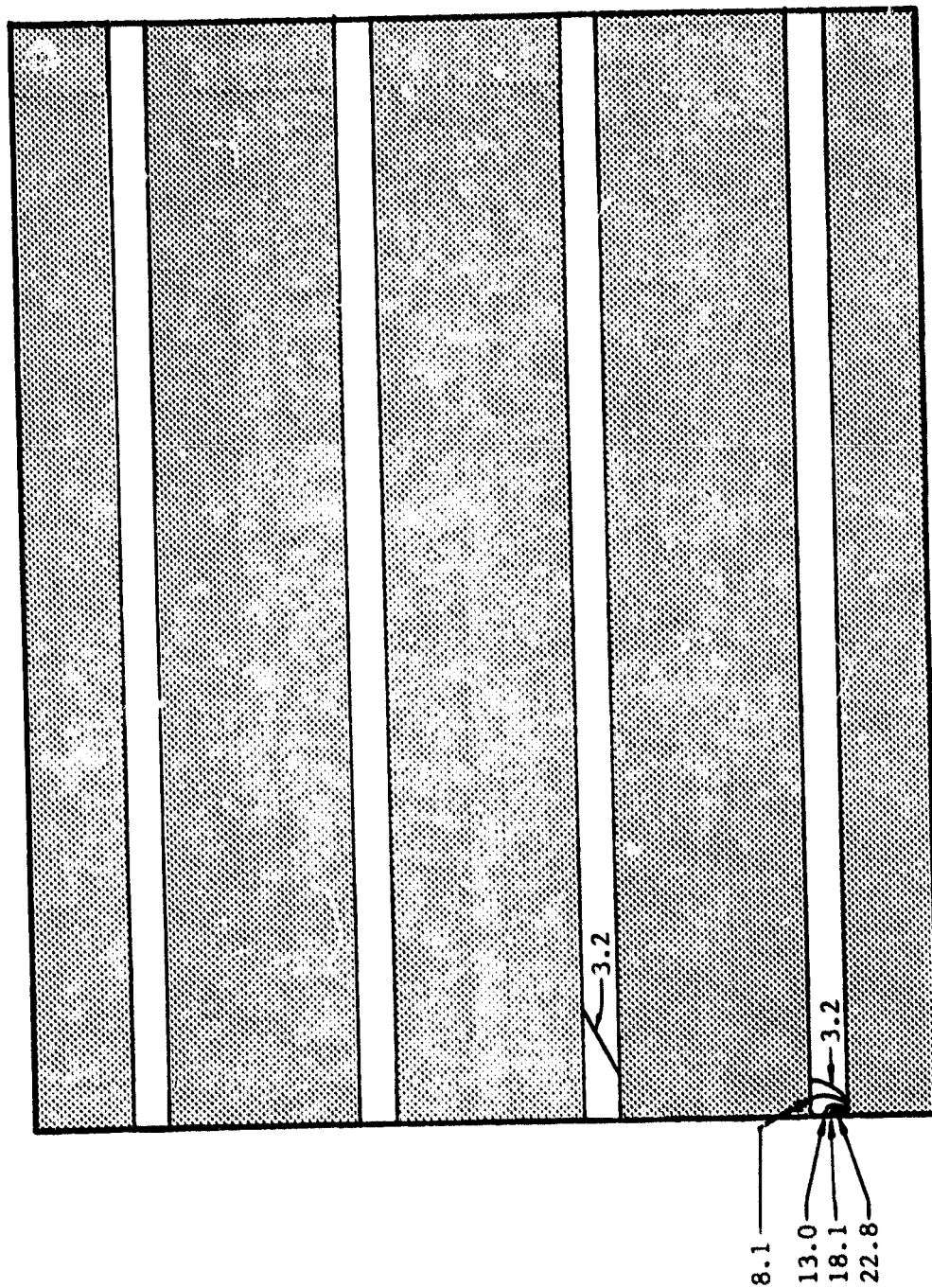


FIGURE 43. Contours of Constant In-Plane Shear Stress (ksi), Average Applied Stress,  $\sigma_x = 24.9$  ksi, 90° Section Longitudinal Model.

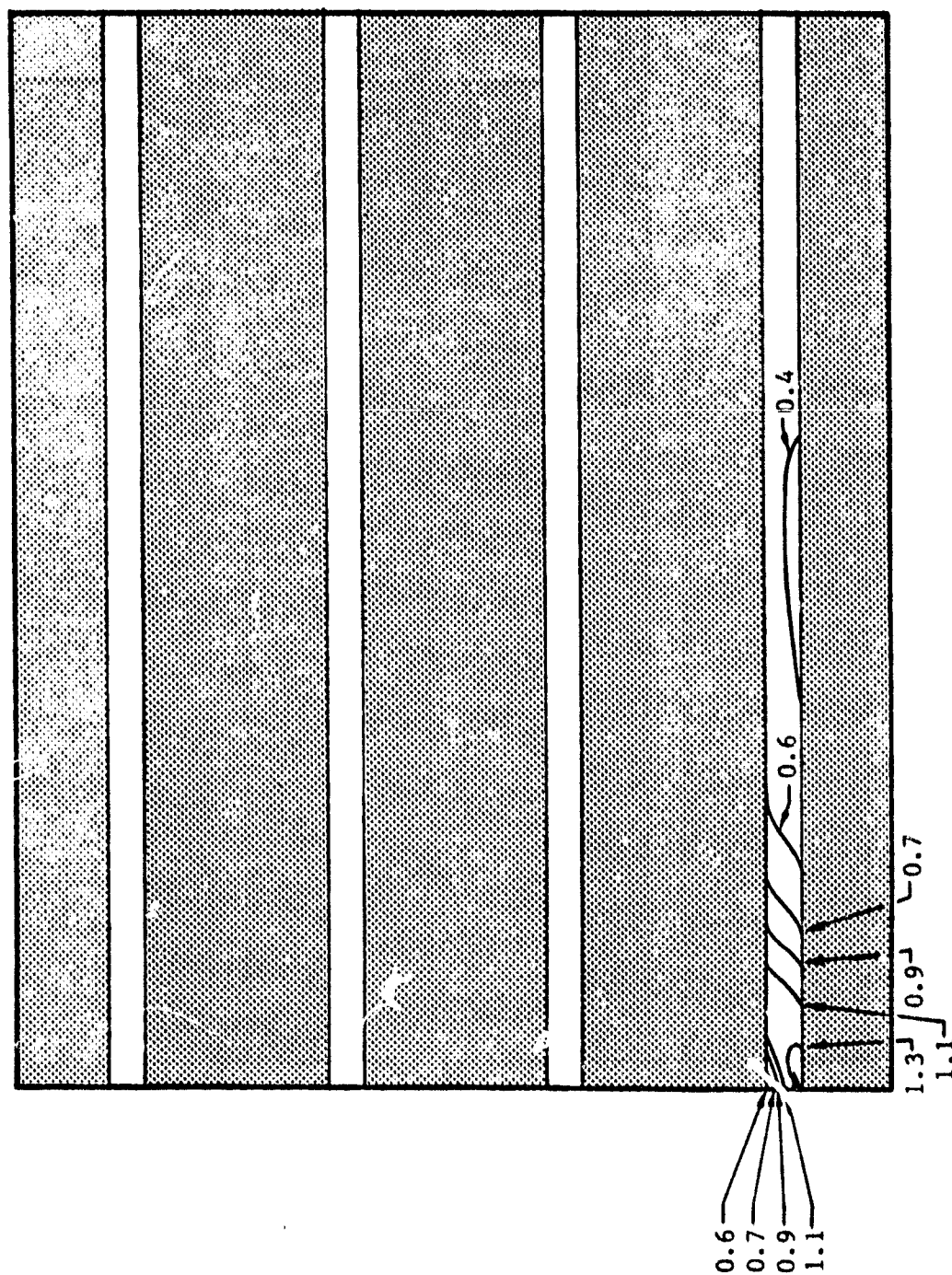


FIGURE 44. Contours of Constant Octahedral Shear Stress, Normalized by Dividing by the Matrix Yield Value of 17 ksi, Average Applied Stress,  $\bar{\sigma}_x = 84$  ksi,  $90^\circ$  Section Longitudinal Model.

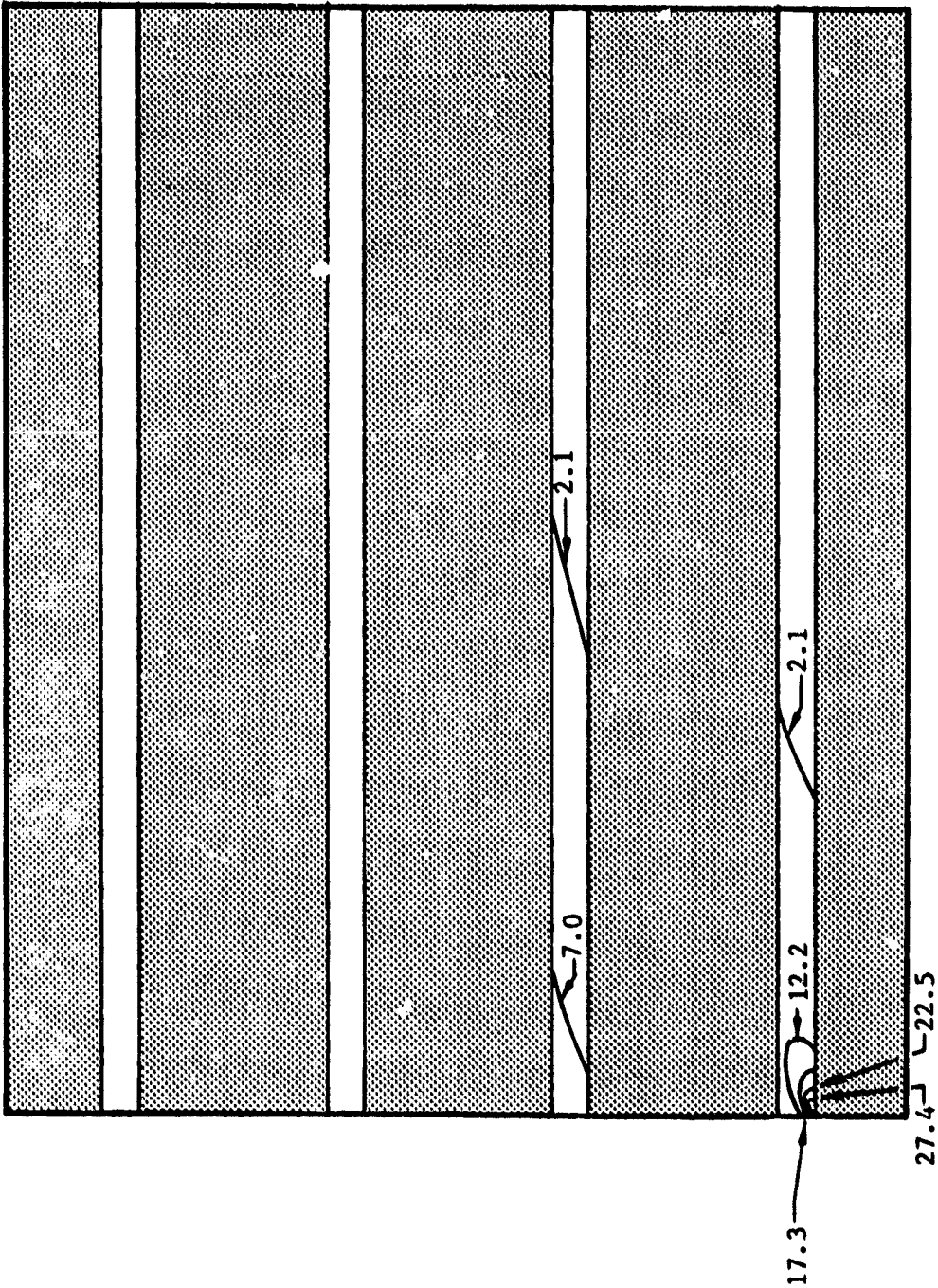


FIGURE 45. Contours of Constant Octahedral Shear Strain ( $10^{-3}$  in/in), Average Applied Stress,  $\sigma_x = 84$  ksi,  $90^\circ$  Section Longitudinal Model.

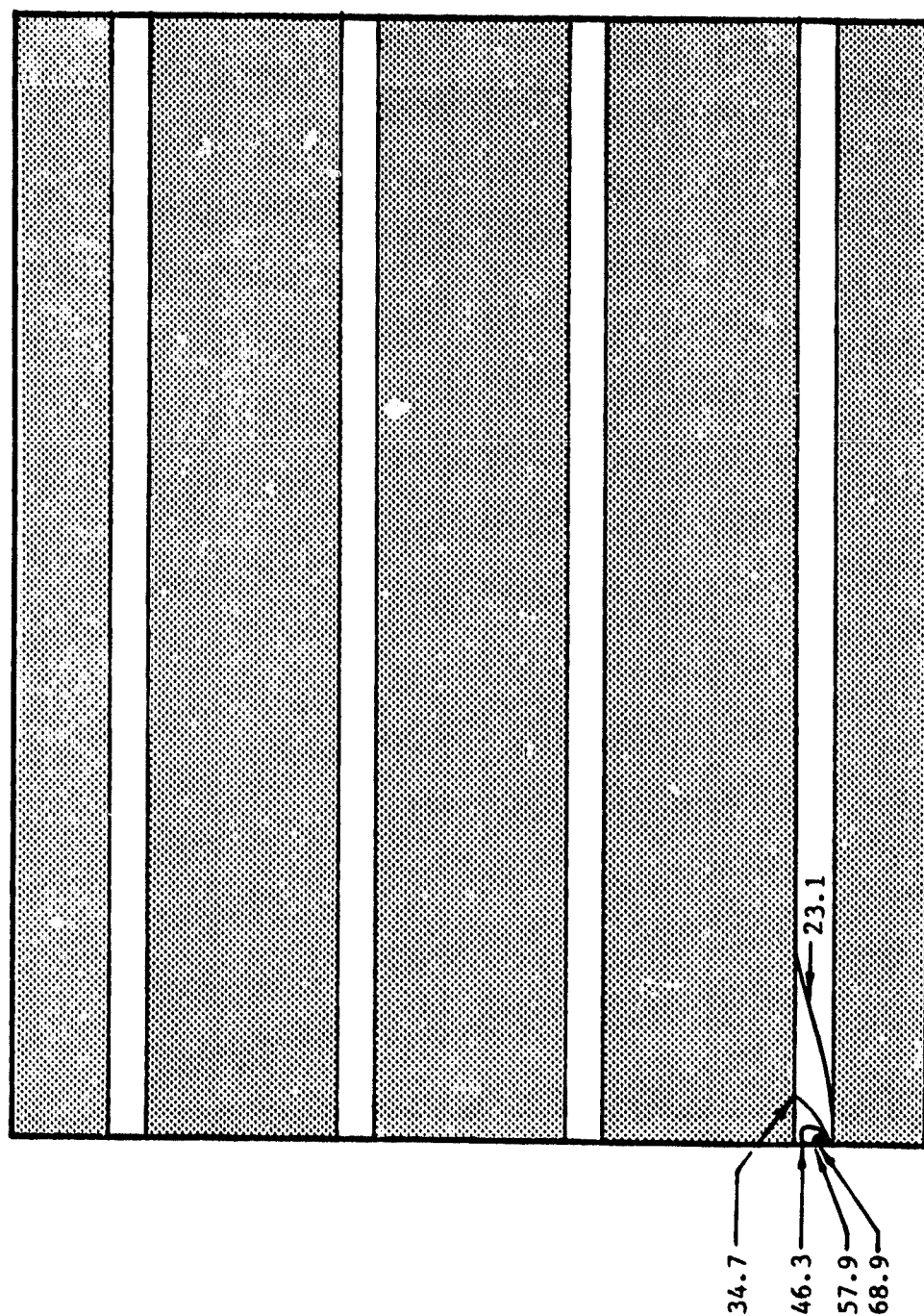


FIGURE 46. Contours of Constant Maximum Principal Stress (ksi), Average Applied Stress,  $\bar{\sigma}_x = 84$  ksi,  $90^\circ$  Section Longitudinal Model.

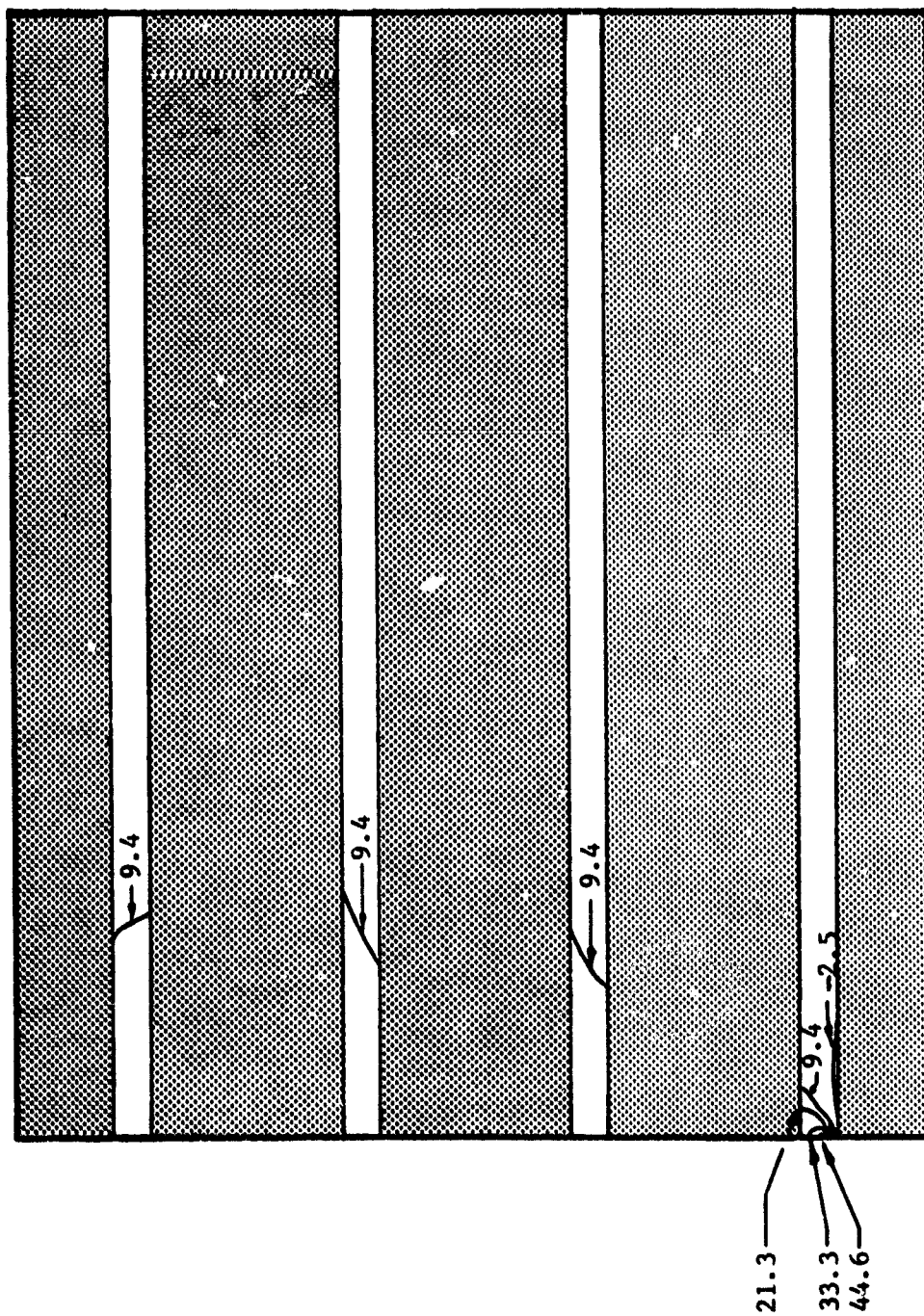


FIGURE 47. Contours of Constant In-Plane Shear Stress (ksi), Average Applied Stress,  $\bar{\sigma}_x = 84$  ksi, 90° Section Longitudinal Model.

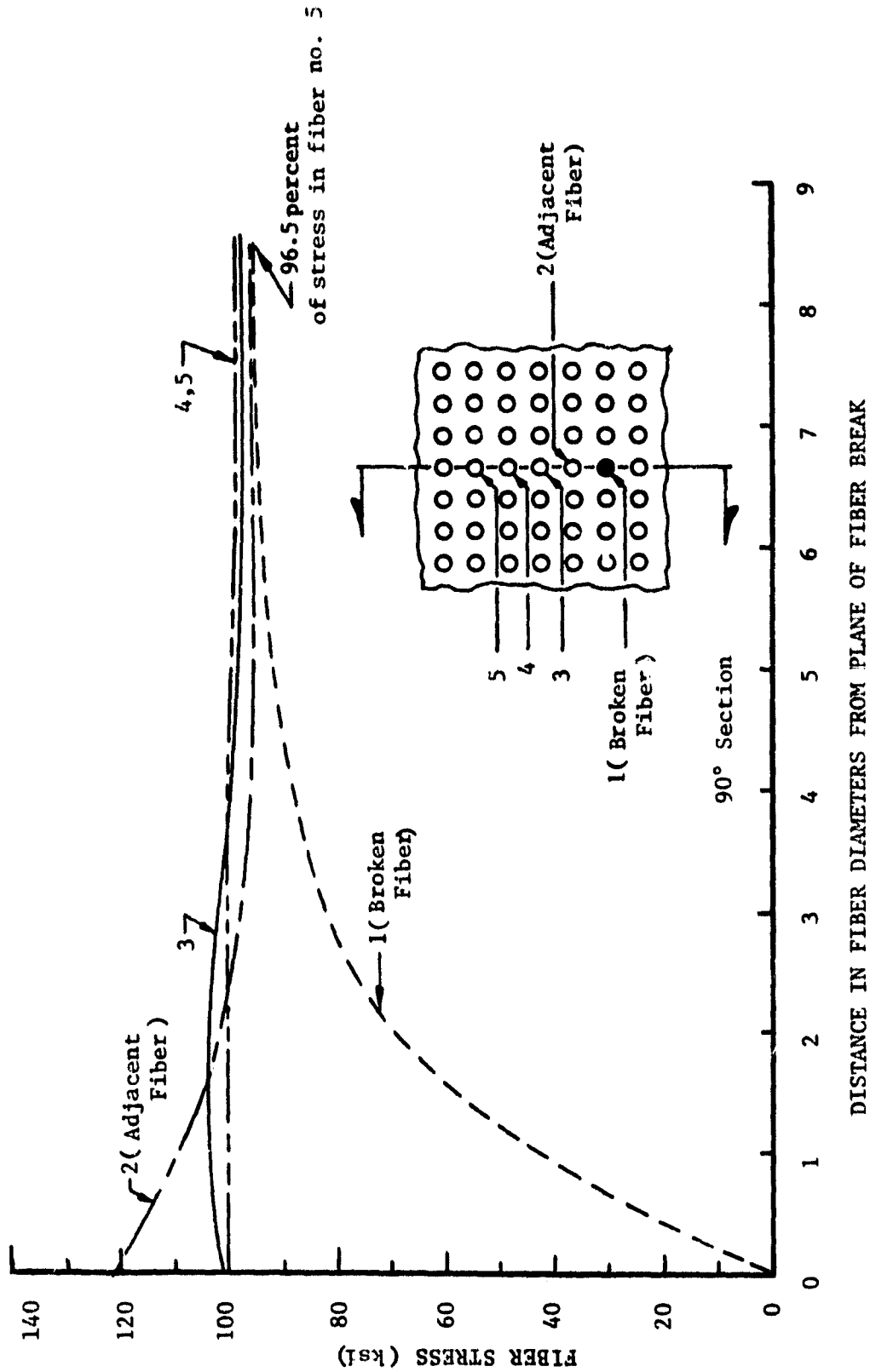


FIGURE 48. Fiber Loadings versus Distance from Plane of Fiber Break, Average Applied Stress,  $\sigma_x = 84$  ksi, 90° Section Longitudinal Model.

crack tip. Also, the shear stress levels in the matrix between outer fibers are much higher, and display some gradation. Of particular interest is the fiber loading plot, Figure 48. In this 90° section model, the effect of the broken fiber is confined to a smaller region than for the 45° section model (see Figure 28), with the adjacent fiber being loaded more than 20 percent higher at the plane of the break than the far field average. The more remote fibers are much less affected. At 8.2 fiber diameters, the broken fiber is almost fully loaded.

The next stage of crack growth occurred at  $\bar{\sigma}_x = 85.4$  ksi, involving 102 elements which failed in 9 intervals of constant stress crack propagation. The tip of the resulting crack advanced along the boundary of the adjacent fiber, as is also suggested by the final shape of the crack, shown in Figures 49 through 53. It will be noted in Figure 49 that the matrix has been unloaded to the point that once again there is no plastic deformation. In all these respects, the results of the 90° section model differ from those of the 45° section model.

Loading was then increased monotonically to a level of 145.4 ksi, at which point one more element failed. Again, the states of stress and strain in the matrix and fibers have been plotted so that one can contrast them to the situation that existed just after this particular crack was formed. These results are presented in Figures 54 through 57. At this point there is a very extensive zone of plastic deformation, and the effects of the crack on the fiber loading are not nearly so localized.

At a load level of 146.8 ksi, extensive crack growth again occurred. A total of 83 elements and 10 intervals of constant stress crack propagation were involved in this process. The shape of the resulting crack,



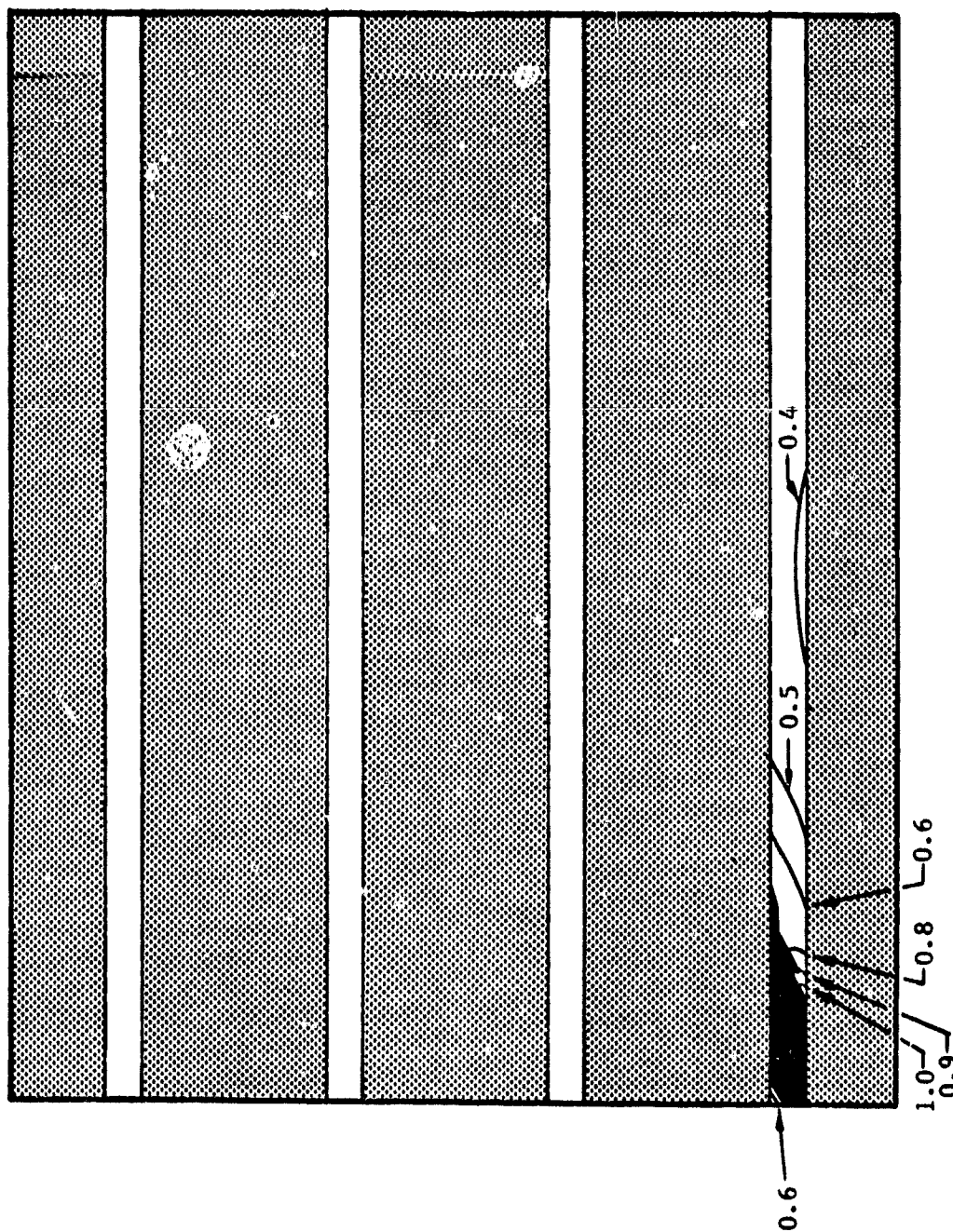


FIGURE 49. Contours of Constant Octahedral Shear Stress  $S_e$ , Normalized by Dividing by the Matrix Yield Value of 17 ksi, Average Applied Stress,  $\bar{\sigma}_x = 85.4$  ksi,  $90^\circ$  Section Longitudinal Model.

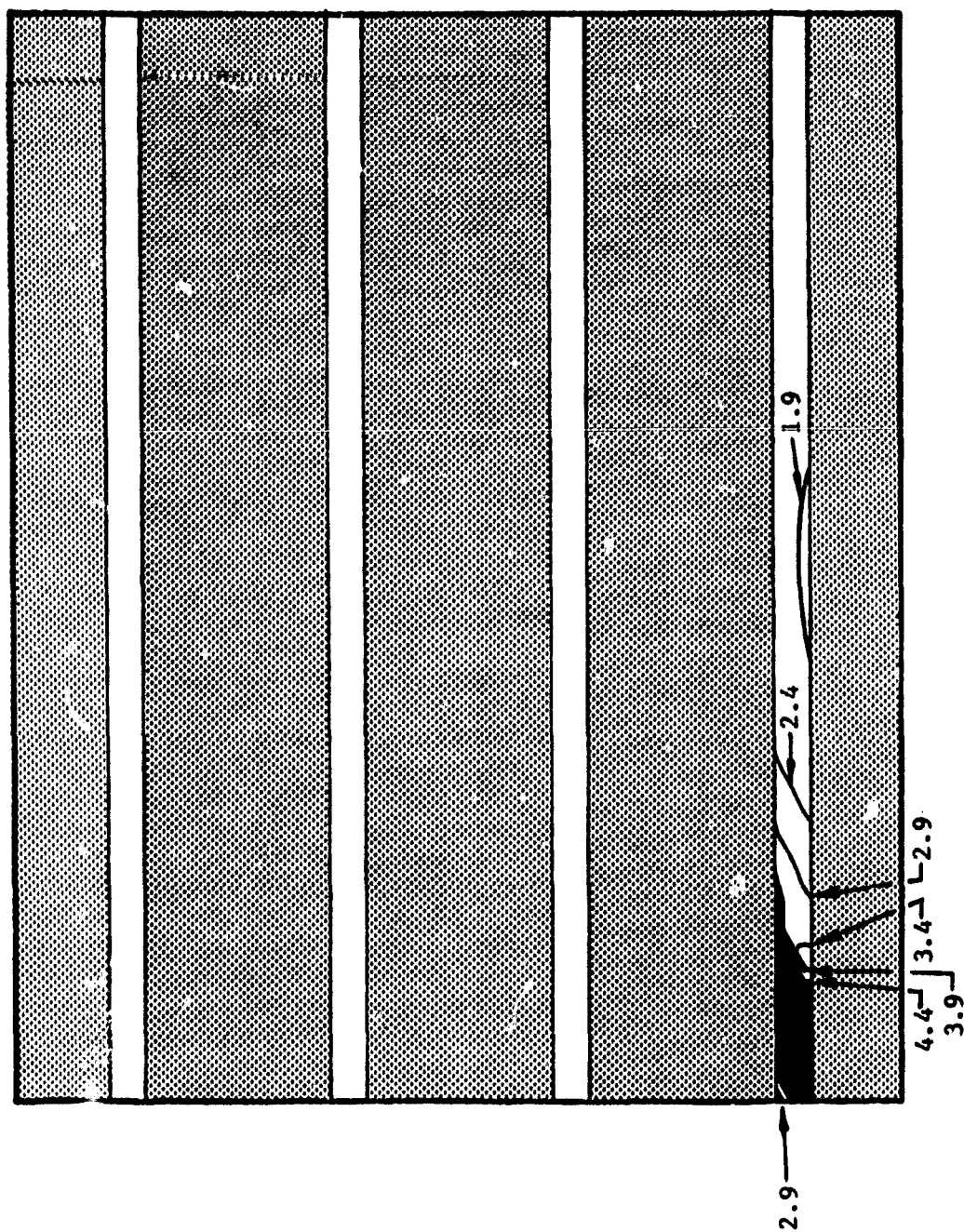


FIGURE 50. Contours of Constant Octahedral Shear Strain ( $10^{-3}$  in/in), Average Applied Stress,  $\bar{\sigma}_x = 85.4$  ksi,  $90^\circ$  Section Longitudinal Model.

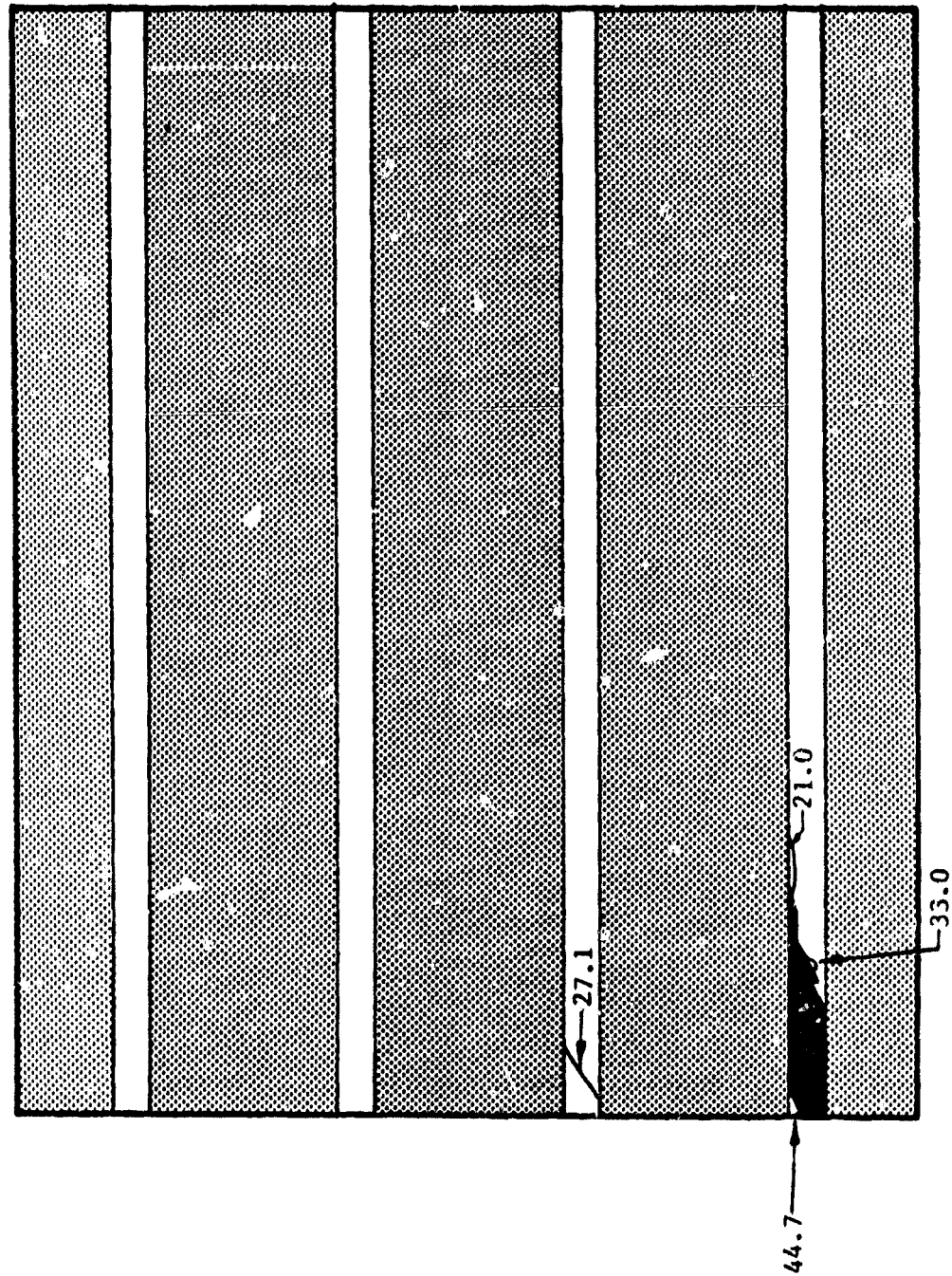


FIGURE 51. Contours of Constant Maximum Principal Stress (ksi), Average Applied Stress,  $\bar{\sigma}_x = 85.4$  ksi,  $90^\circ$  Section Longitudinal Model.

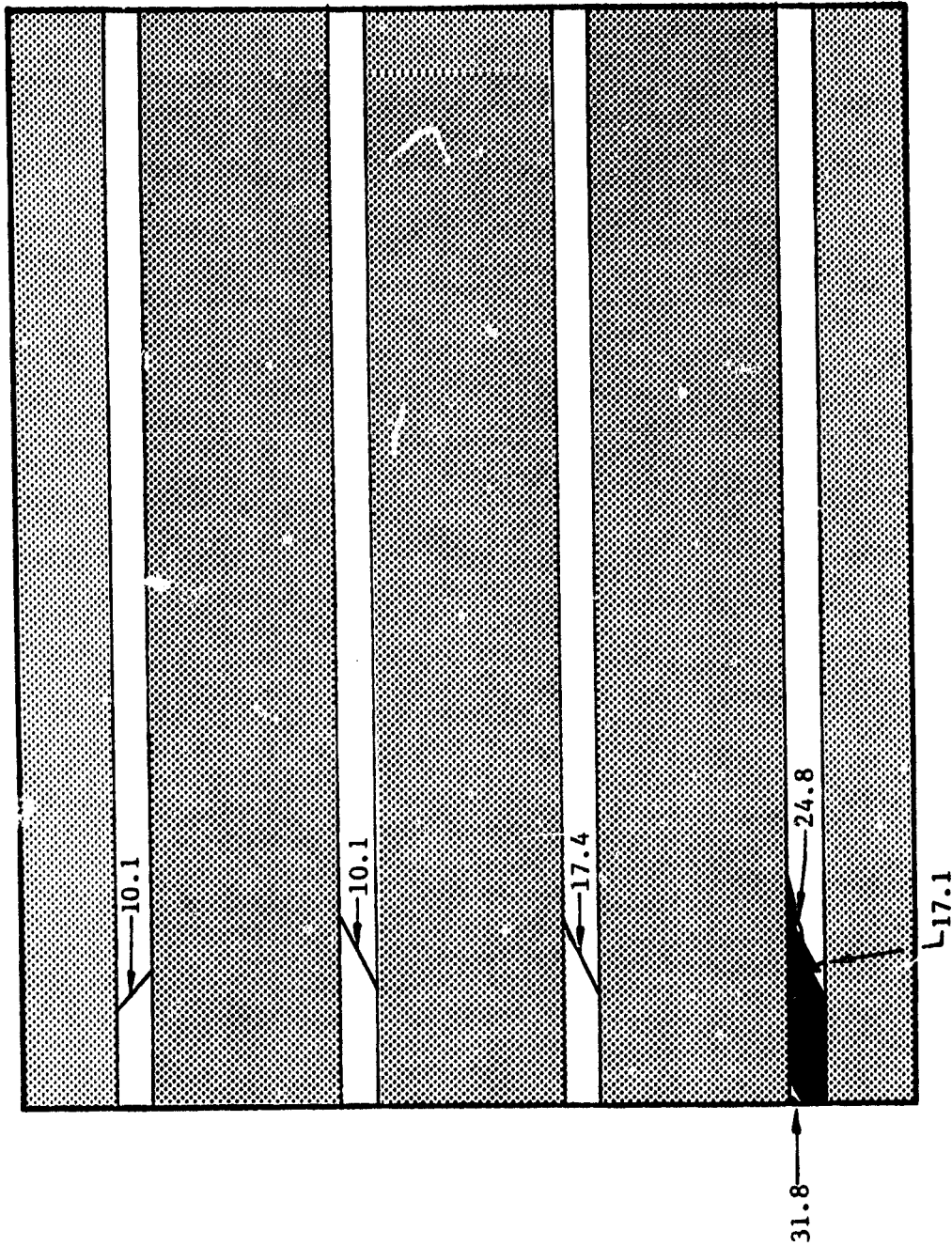


FIGURE 52. Contours of Constant In-Plane Shear Stress (ksi), Average Applied Stress,  $\bar{\sigma}_x = 85.4$  ksi,  $90^\circ$  Section Longitudinal Model.

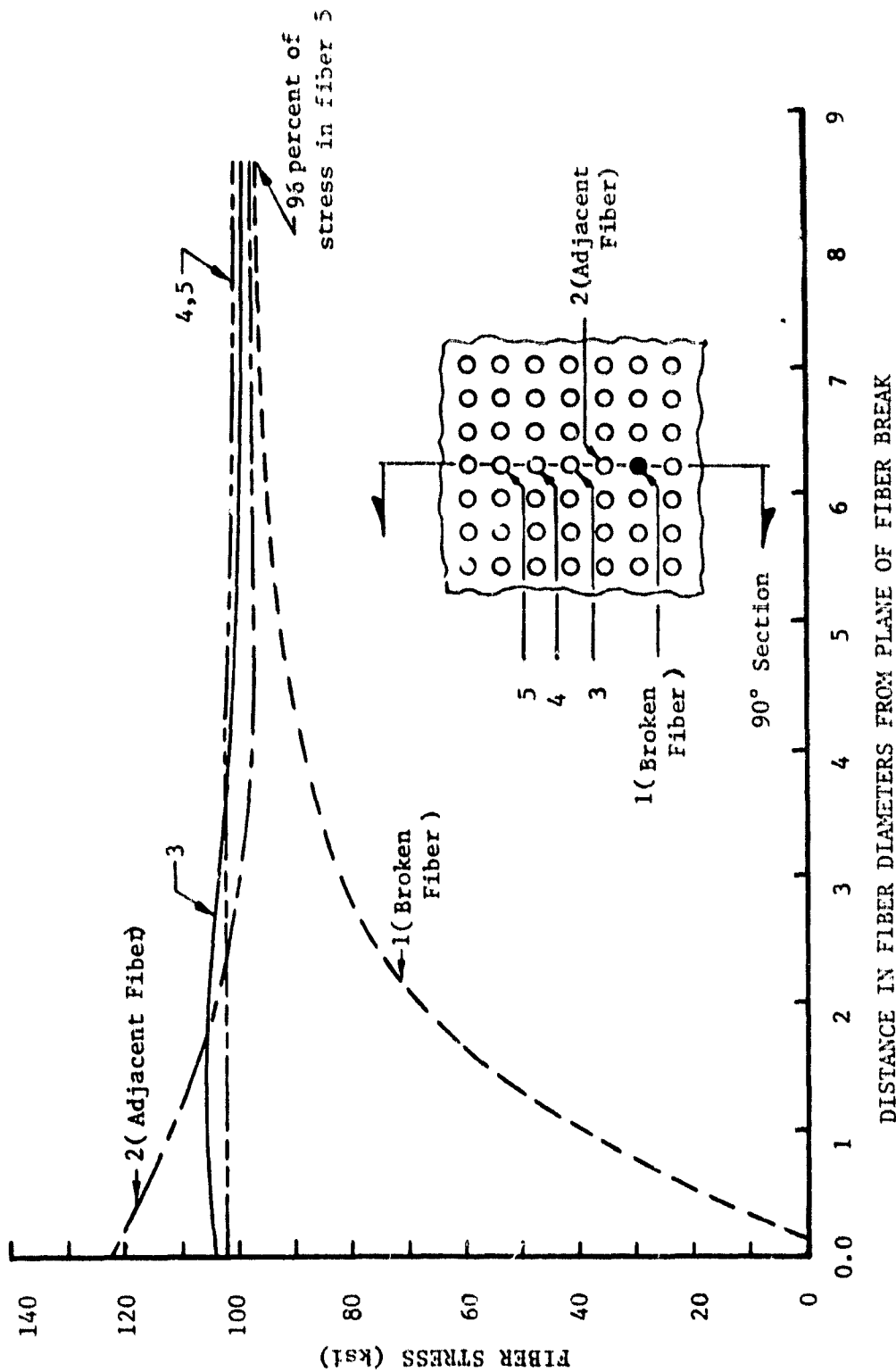


FIGURE 53. Fiber Loadings versus Distance from Plane of Fiber Break, Average Applied Stress,  $\bar{\sigma}_x = 85.4$  ksi, 90° Section Longitudinal Model.



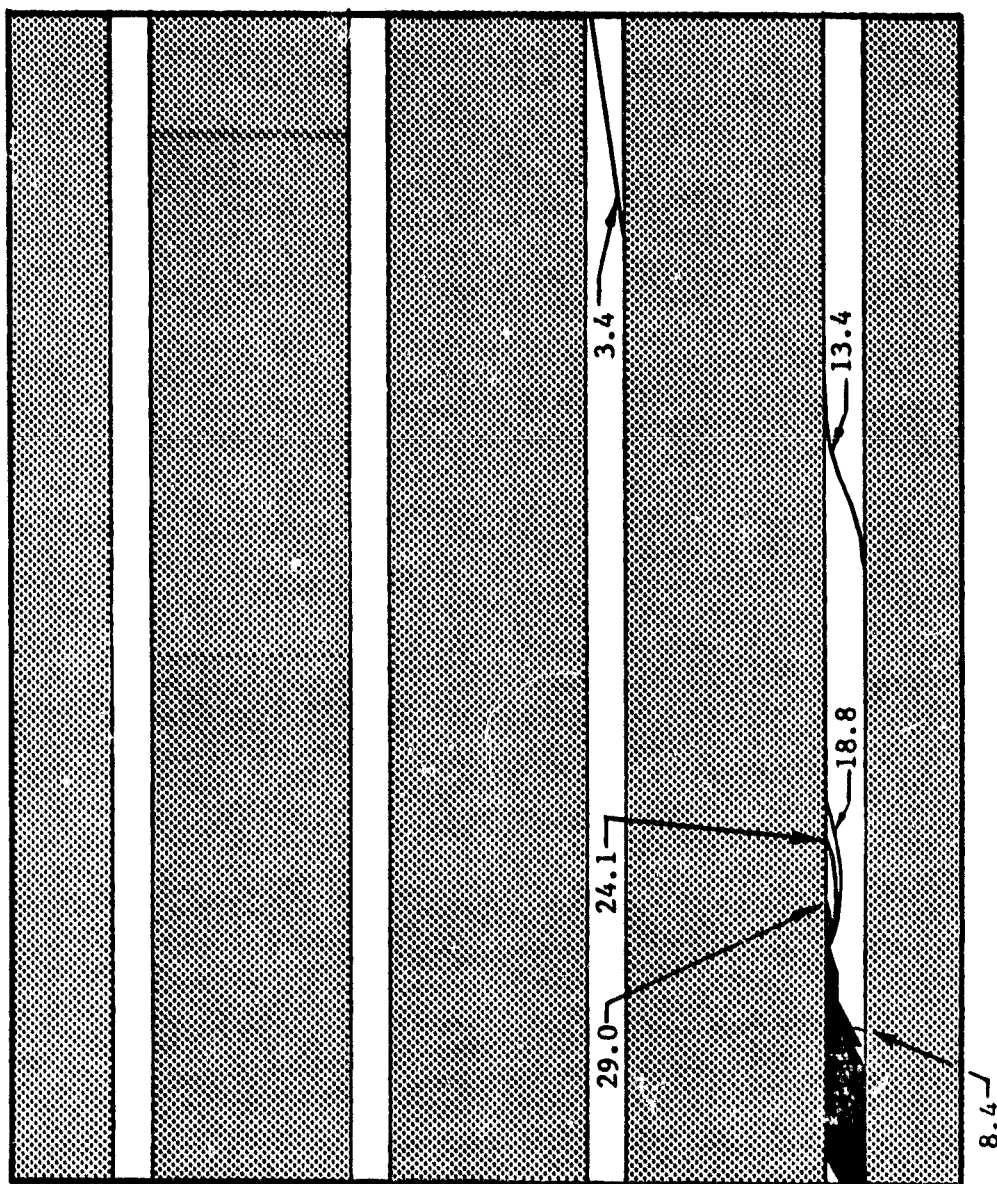


FIGURE 55. Contours of Constant Octahedral Shear Strain ( $10^{-3}$  in/in), Average Applied Stress,  $\bar{\sigma}_x = 145.4$  ksi,  $90^\circ$  Section Longitudinal Model.



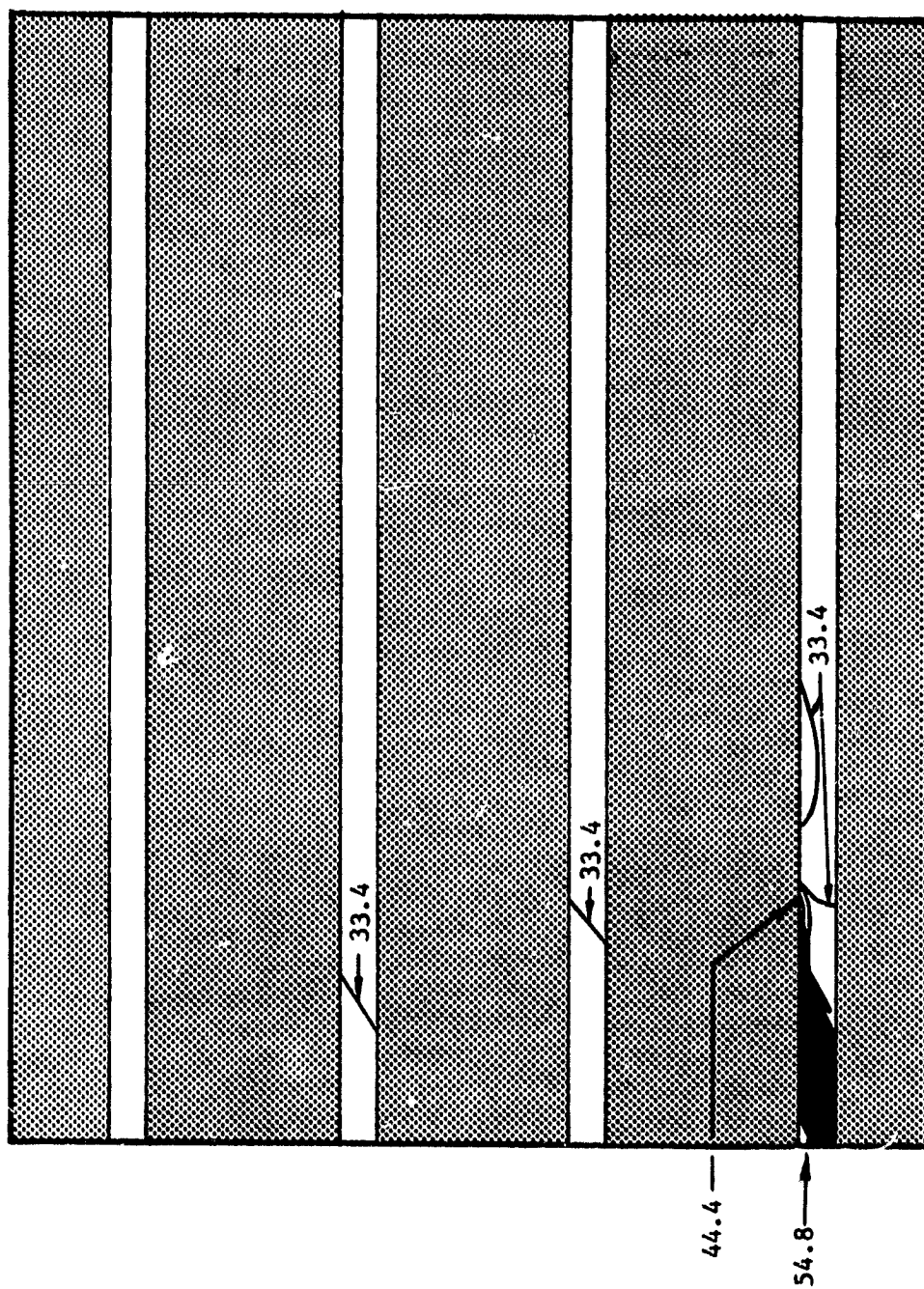
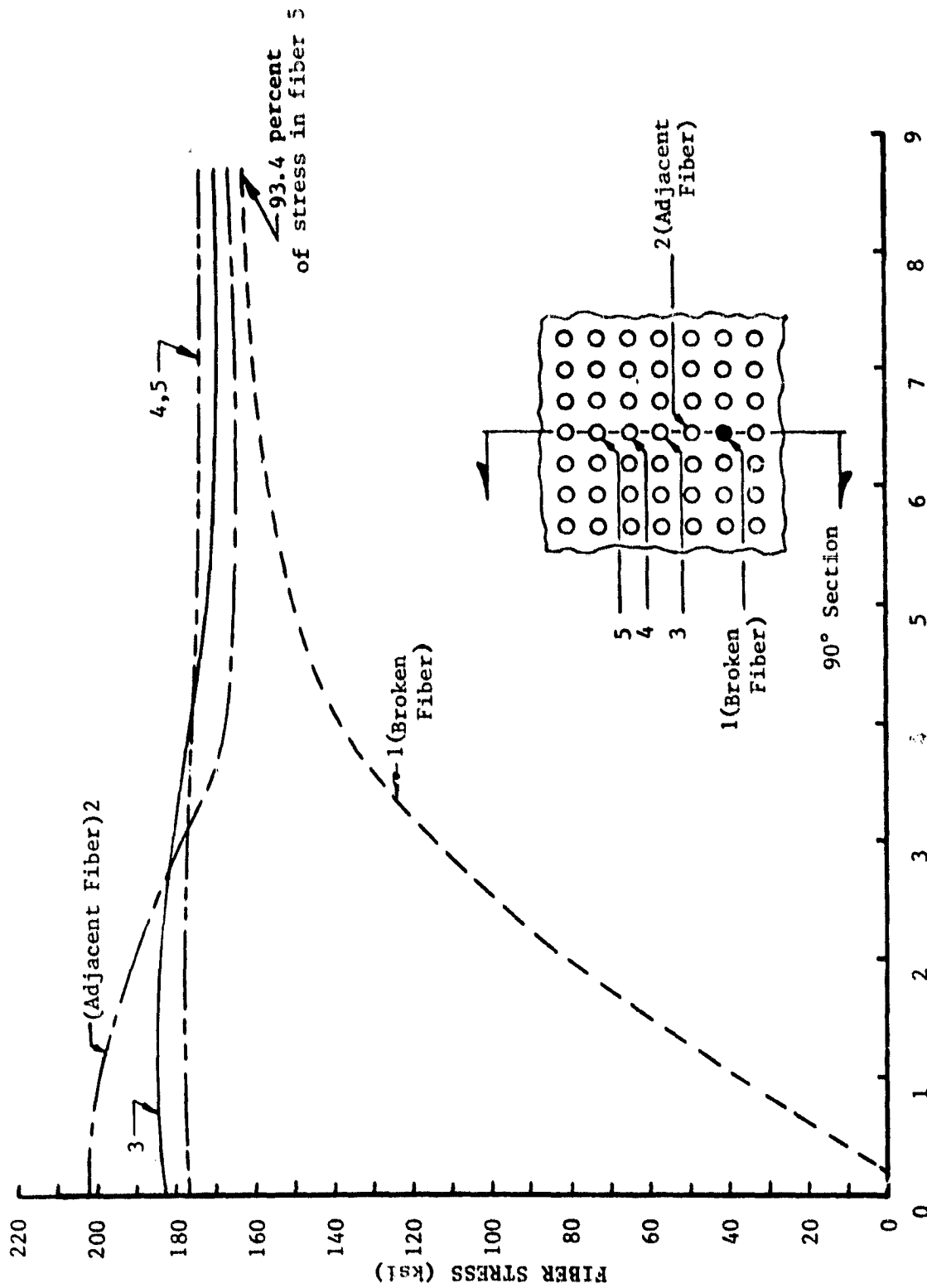


FIGURE 56. Contours of Constant Maximum Principal Stress (ksi), Average Applied Stress,  $\bar{\sigma}_x = 145.4$  ksi,  $90^\circ$  Section Longitudinal Model.





DISTANCE IN FIBER DIAMETERS FROM PLANE OF FIBER BREAK

FIGURE 57. Fiber Loadings versus Distance from Plane of Fiber Break, Average Applied Stress,  $\bar{\sigma}_x = 145.4$  ksi, 90° Section Longitudinal Model.

along with contours of normalized octahedral shear stress, are presented in Figure 58. It will be noted that once again the crack has grown through the previous region of plastic deformation, and little or no plastic deformation remains after this process. In Figure 59, the affect of the crack growth on the fiber loading can be seen. The two nearest fibers become affected near the plane of the fiber break, and in addition, the two more remote fibers begin to display the same pattern as the closer fibers, i.e., increasing load in the vicinity of the flaw, decreasing as the axial distance from the break site increases.

Continued loading of the 90° section model to 208.3 ksi produced no additional element failures, at which point this computer run was terminated. The last states of stress to be plotted were at an average applied stress of 193.3 ksi. These are presented in Figures 60 through 63. A plot of the composite stress versus strain for this example is presented in Figure 64.

#### 6.5. Crack Initiation and Propagation in the Transverse Section Model, Loaded Transversely

Stress increments  $\bar{\sigma}_x$  were applied to the right hand boundary of the transverse model shown in Figure 11. Plastic deformation of the aluminum matrix began at the fiber-matrix interface at a point about 30° from the positive x-axis, i.e., Element Nos. 88 through 91 (see Figure 11). As loading increased, these elements became even more highly stressed. However, at 58.4 ksi, Element No. 81 ruptured in a hydrostatic tension failure mode. This failure triggered the failure of Element Nos. 83 and 85, whereupon further strain energy redistribution was required. Crack propagation progressed along the fiber-matrix interface, terminating at



FIGURE 58. Contours of Constant Octahedral Shear Stress, Normalized by Dividing by the Matrix Yield Value of 17 ksi, Average Applied Stress,  $\bar{\sigma}_x = 146.8$  ksi,  $90^\circ$  Section Longitudinal Model.

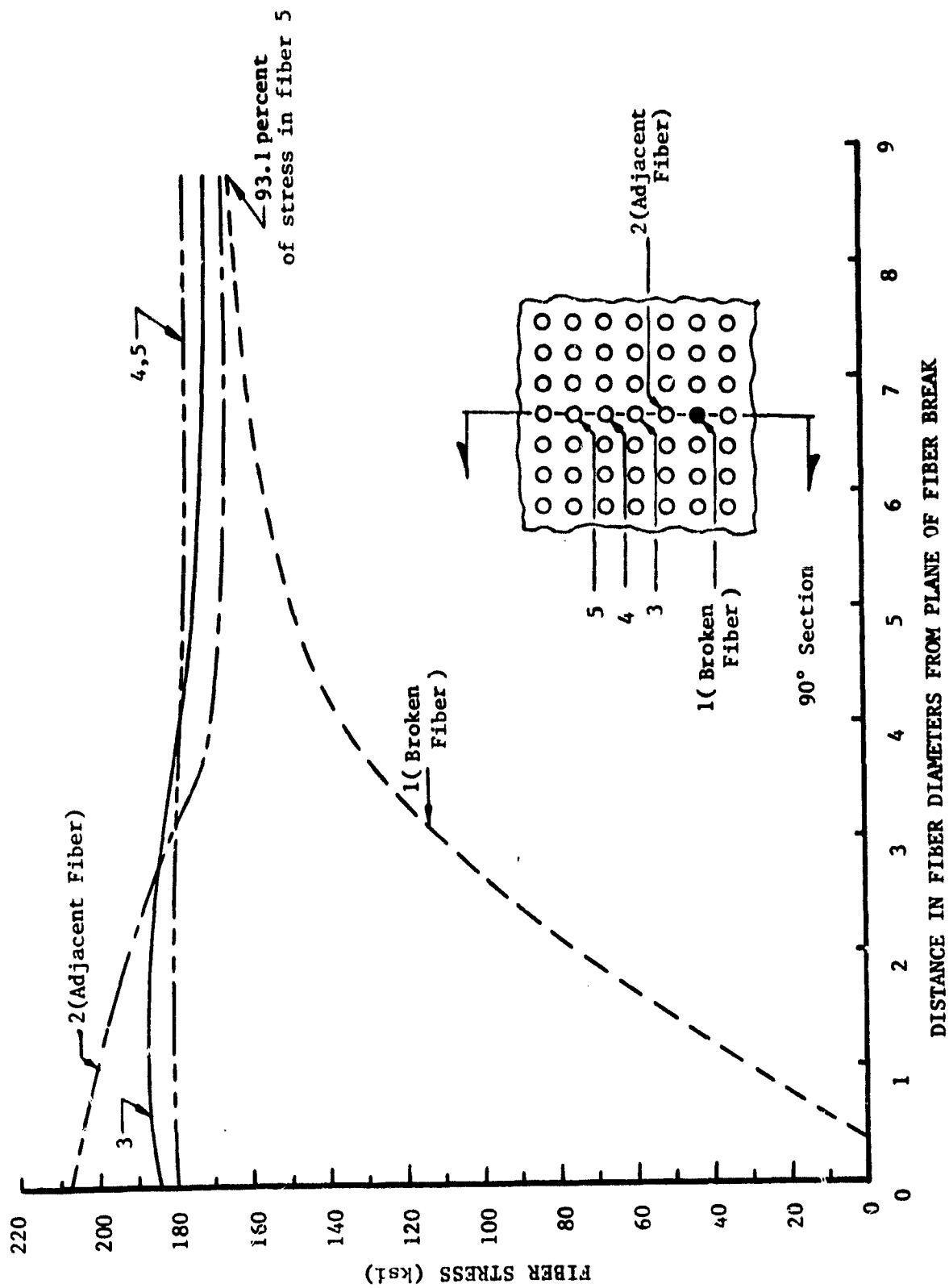


FIGURE 59. Fiber Loading versus Distance from Plane of Fiber Break, Average Applied Stress,  $\bar{\sigma}_x = 146.8$  ksi, 90° Section Longitudinal Model.

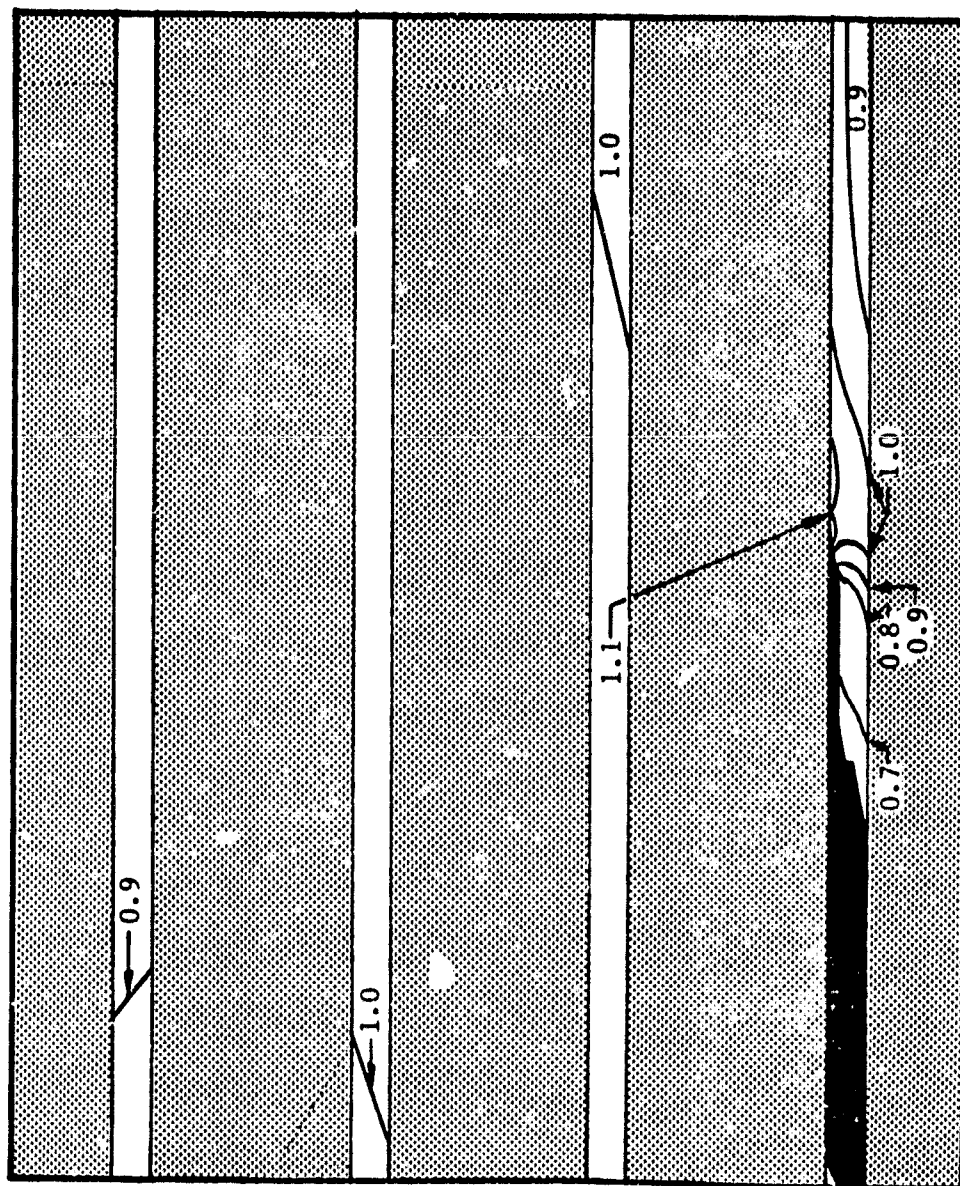


FIGURE 60. Contours of Constant Octahedral Shear Stress, Normalized by Dividing by the Matrix Yield Value of 17 ksi, Average Applied Stress,  $\bar{\sigma}_x = 193.3$  ksi,  $90^\circ$  Section Longitudinal Model.

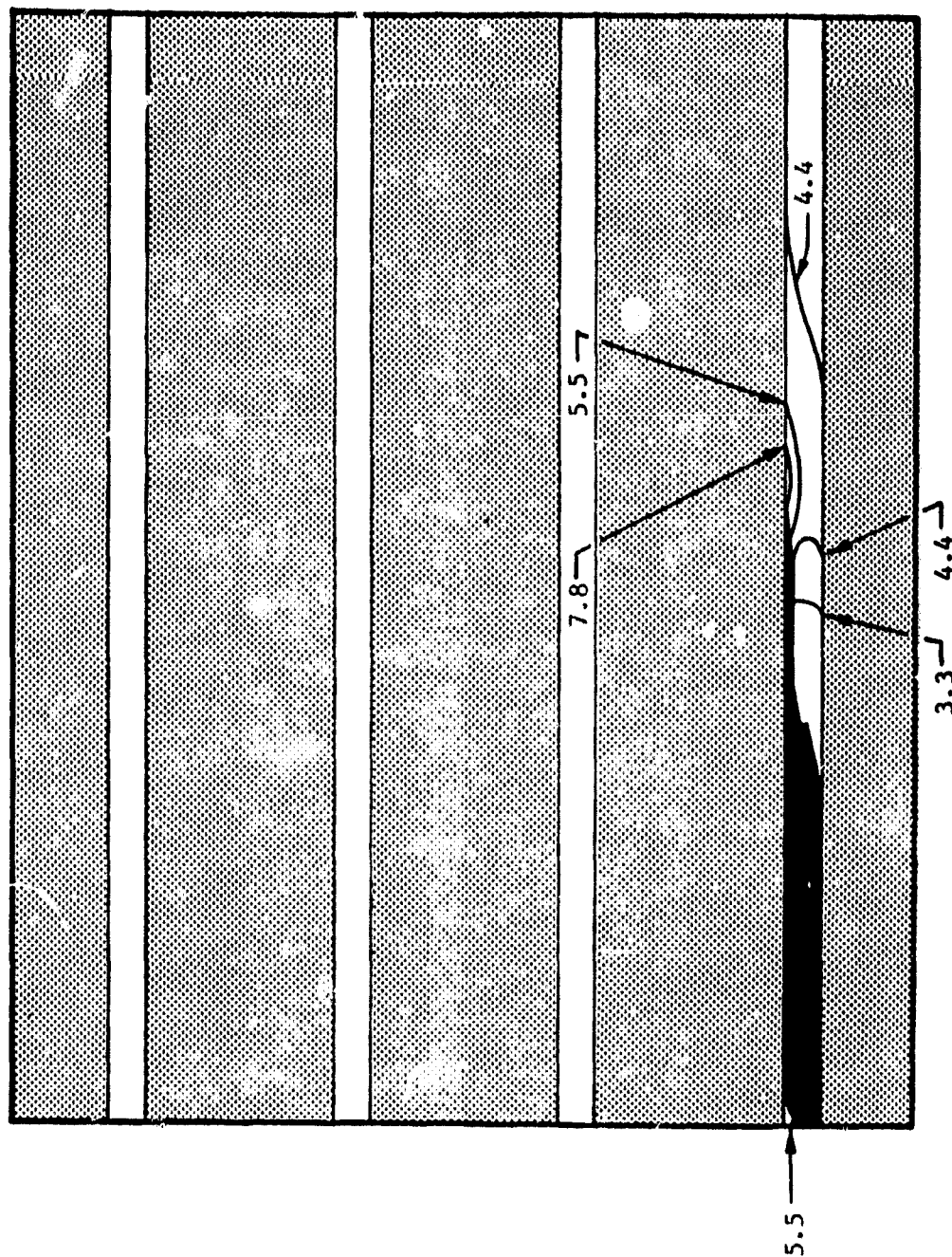


FIGURE 61. Contours of Constant Octahedral Shear Strain ( $10^{-3}$  in/in), Average Applied Stress,  $\bar{\sigma}_x = 193.3$  ksi,  $90^\circ$  Section Longitudinal Model.

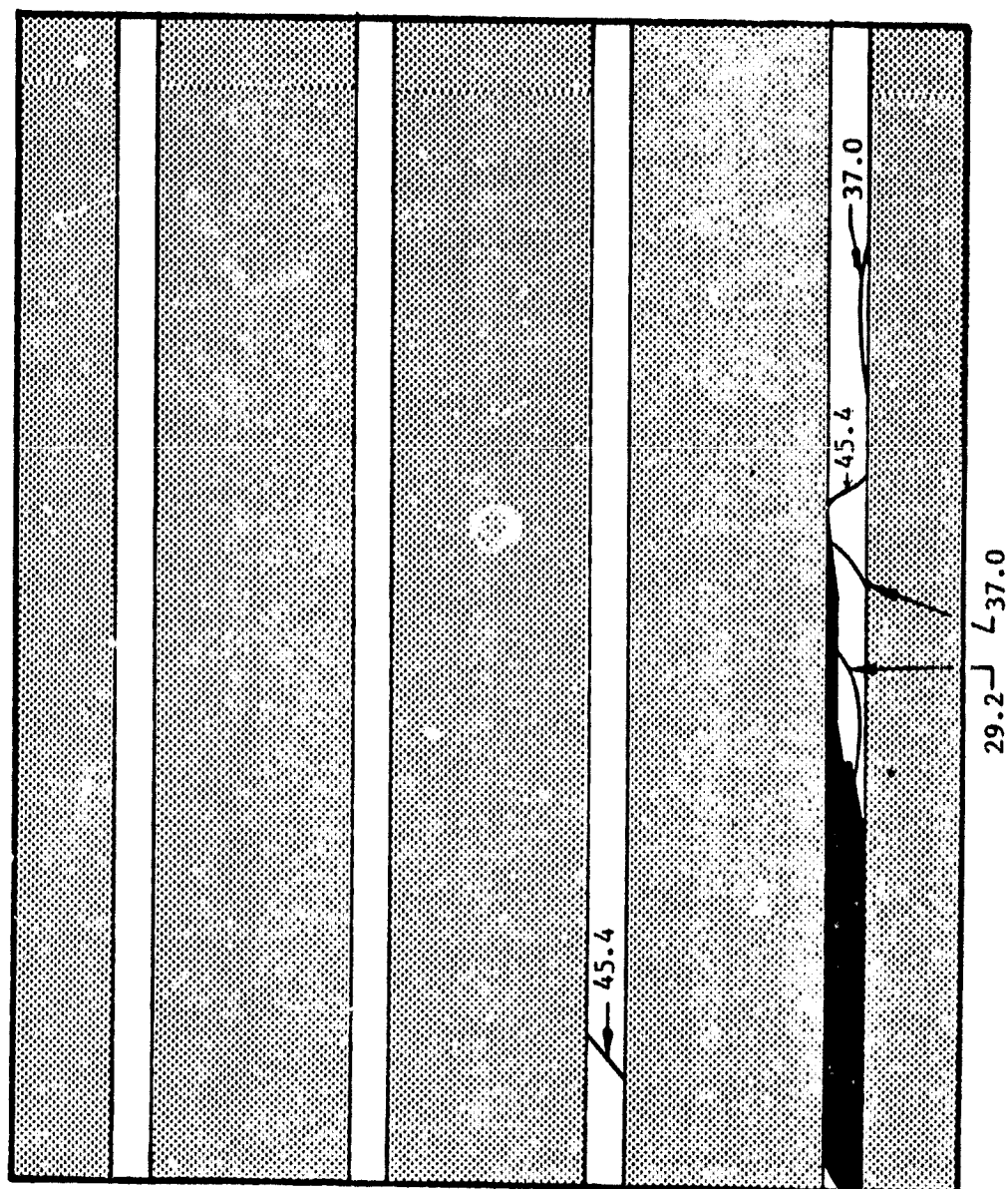


FIGURE 62. Contours of Constant Maximum Principal Stress (ksi), Average Applied Stress,  $\bar{\sigma}_x = 193.3$  ksi,  $90^\circ$  Section Longitudinal Model.

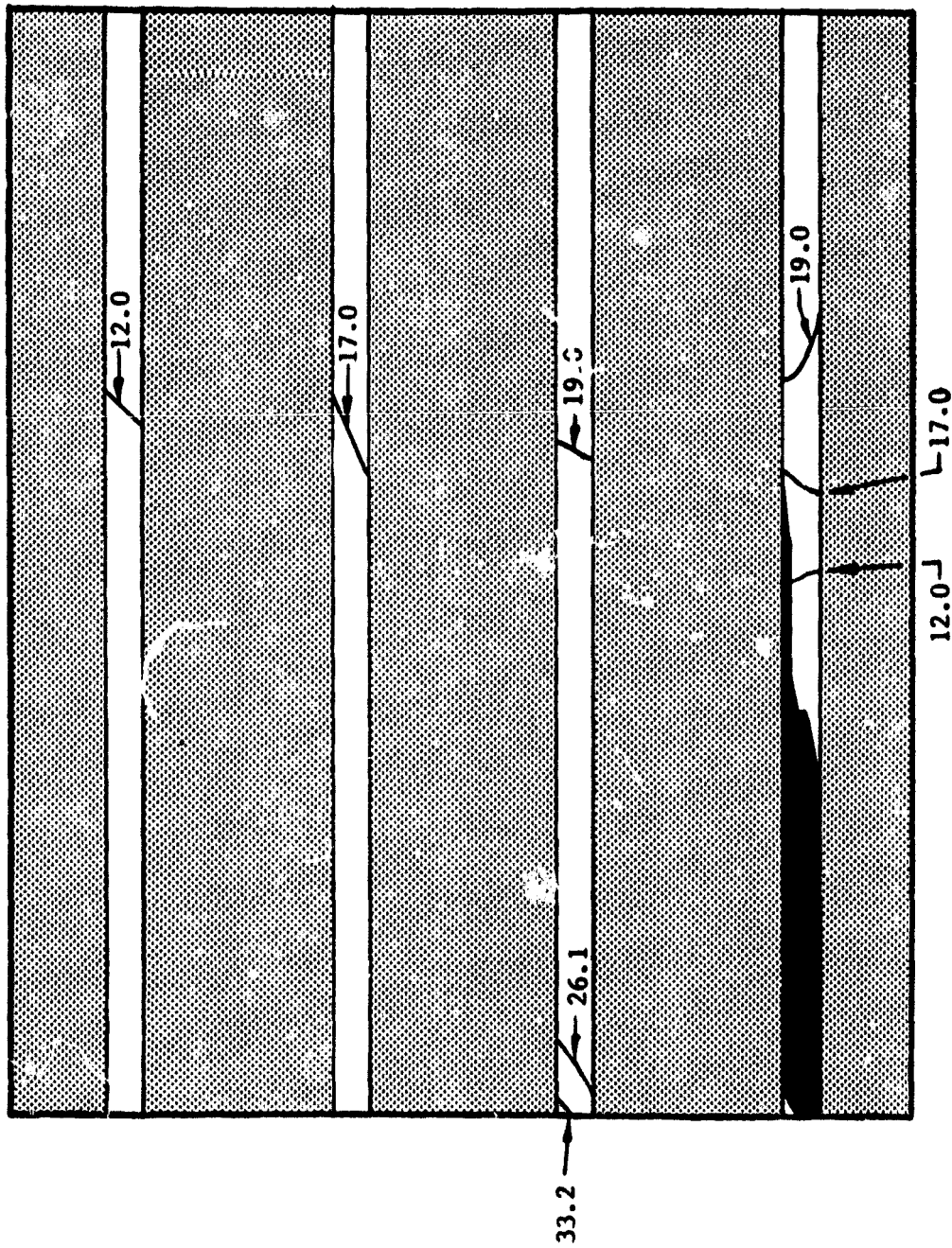


FIGURE 63. Contours of Constant In-Plane Shear Stress (ksi), Average Applied Stress,  $\bar{\sigma}_x = 193.3$  ksi,  $90^\circ$  Section Longitudinal Model.



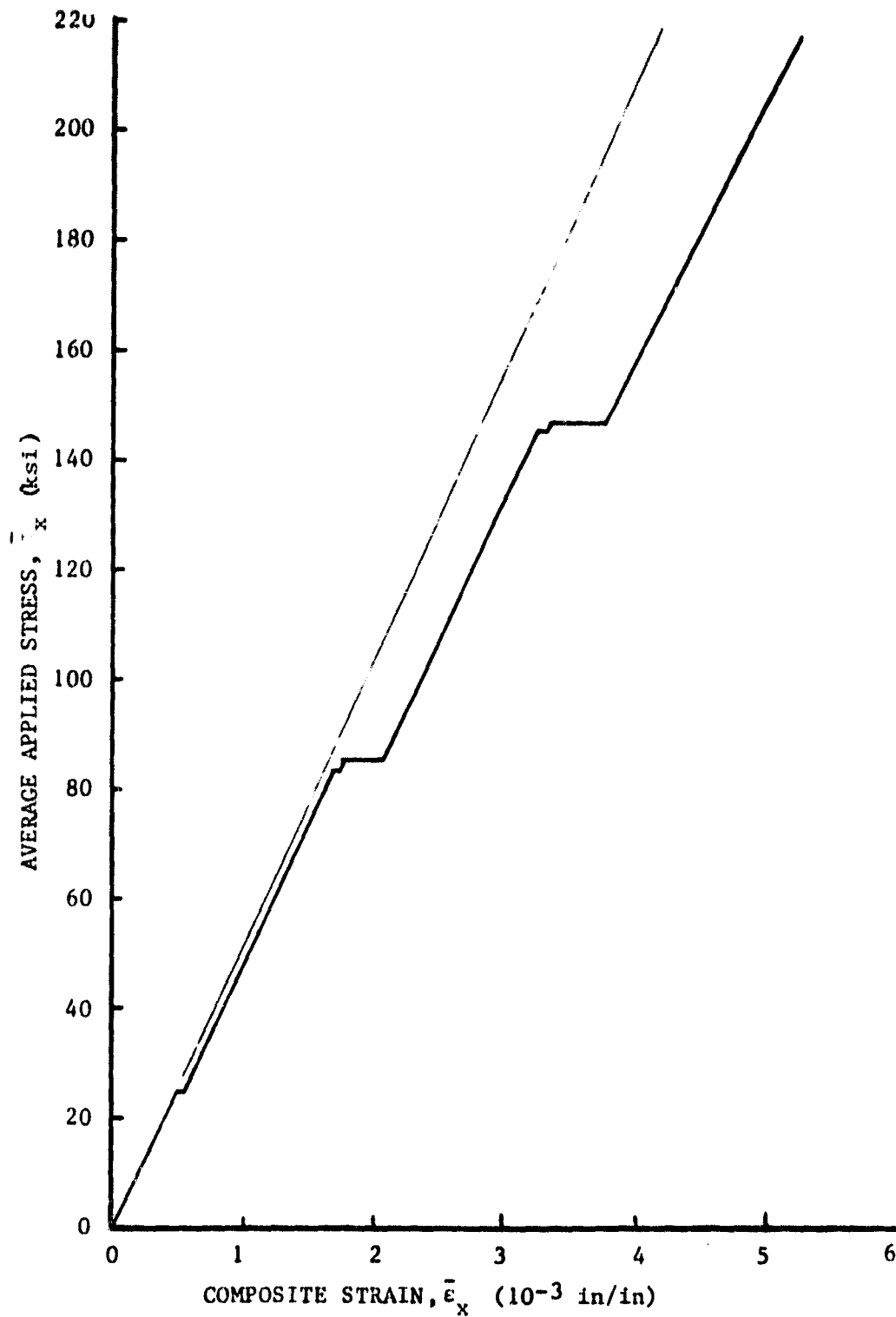


FIGURE 64. Plot of Applied Stress versus Composite Strain for the 90° Section Longitudinal Model, 12.5 Percent Discontinuous Fibers.

the point shown in Figure 65. This failure pattern agrees very well with that presented by Adams [4] in his 1973 study of crack propagation in a transverse section of a unidirectional boron/aluminum composite. His effort involved an analysis scheme with a constant displacement rather than a constant stress loading procedure, a finer mesh finite element representation, and smaller loading increments than were used in the present analysis. Adams also typically observed initial failure at matrix elements along the fiber-matrix interface at a point approximately  $30^\circ$  from the x-axis. However, his analysis did not include a hydrostatic failure mode, which could explain the slight difference in the location of crack initiation observed in the present study.

The loading increment following the 58.4 ksi load level resulted in further element failures, with the crack progressing along the fiber-matrix boundary. While this example was undertaken primarily for the purpose of comparing results of the present analysis with those of Adams [4], it is clear that the effects of disbonds, local matrix voids, and other manufacturing flaws on the transverse strength of a unidirectional composite could also be characterized. With larger finite element arrays, constructed to simulate such flaws, manufacturing cycles of compression and thermal loading could be imposed to determine the residual stresses caused by these defects, and their effects on subsequent service loading and environmental exposure.

#### 6.6. Axial Loading of the Axisymmetric Longitudinal Model

Numerous computer runs, involving a variety of finite element models, were made to verify the correctness and accuracy of the axisymmetric

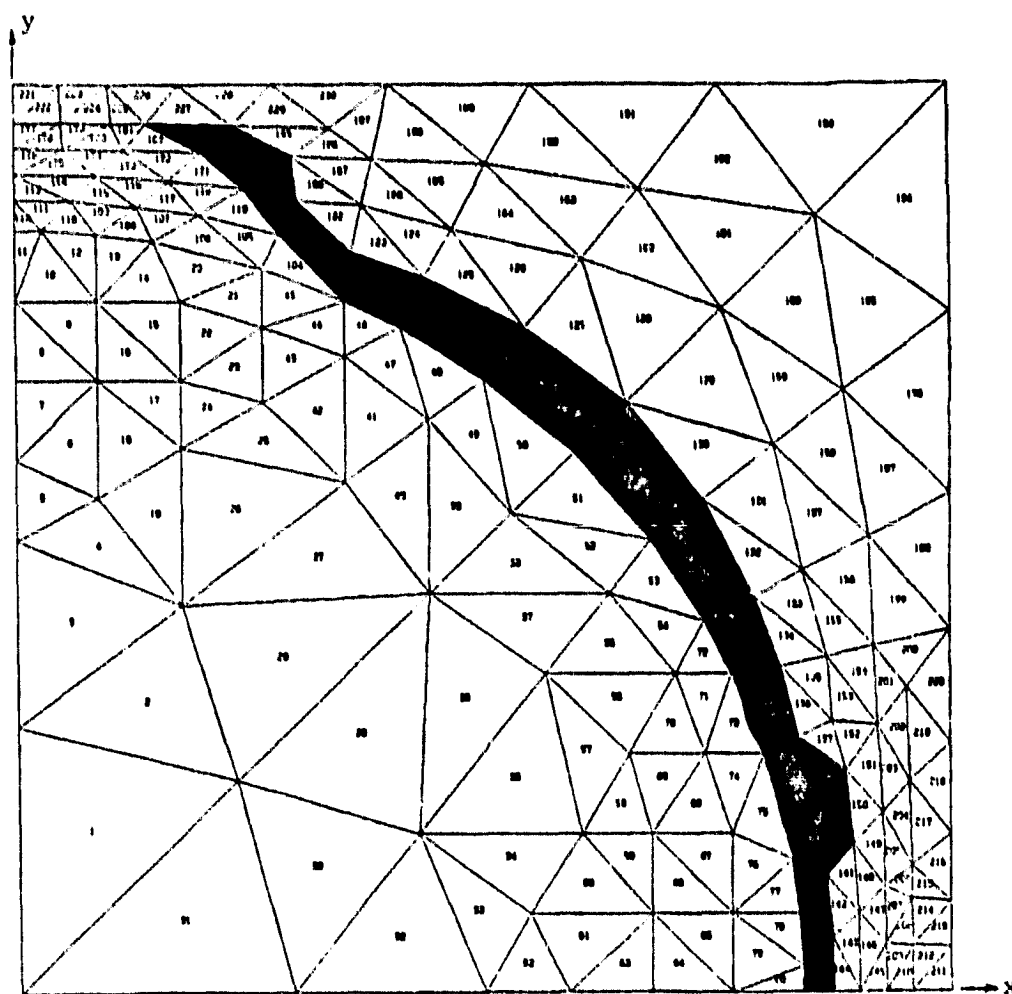


FIGURE 65. Crack Propagation in the Transverse Section Model at an Average Applied Stress,  $\bar{\sigma}_x = 58.4$  ksi.

analysis program under all possible combinations of element geometry, material types (i.e., elastic isotropic or transversely isotropic, and plastic isotropic) and loading. When all difficulties had been identified and corrected, a series of runs was made, employing the finite element model shown in Figure 13. Three different variations of this model were employed in this preliminary study, aimed primarily at assessing the effect of thickness of the annular sheath of aluminum on the response of the single broken fiber configuration. The first model studied represents the condition of minimum fiber spacing in a 55 percent fiber volume, square array, unidirectional composite. This results in a model in which the broken fiber has a rather thin sheath of matrix around it, the ratio of the fiber radius to the total model radius ( $r_f/r_m$ ) being 0.714. Another model studied was the case of maximum fiber spacing in the 55 percent fiber volume, square array composite, wherein the ratio of the fiber radius to the model radius is 0.424. Finally, after studying the results of runs using the first two models, it was decided to increase the thickness of the matrix in the maximum fiber spacing model by 50 percent, to further investigate the effect of matrix thickness in this particular configuration ( $r_f/r_m = 0.330$ ).

The results of this study are summarized in contour plots for each model configuration, with normalized octahedral shear stress, octahedral shear strain, maximum principal stress, and in-plane shear stress being the parameters plotted.

Figures 66 and 67 represent the case of minimum matrix thickness. It can be seen immediately that a rather small portion of the cross section of the model perpendicular to the applied load is aluminum matrix. Since

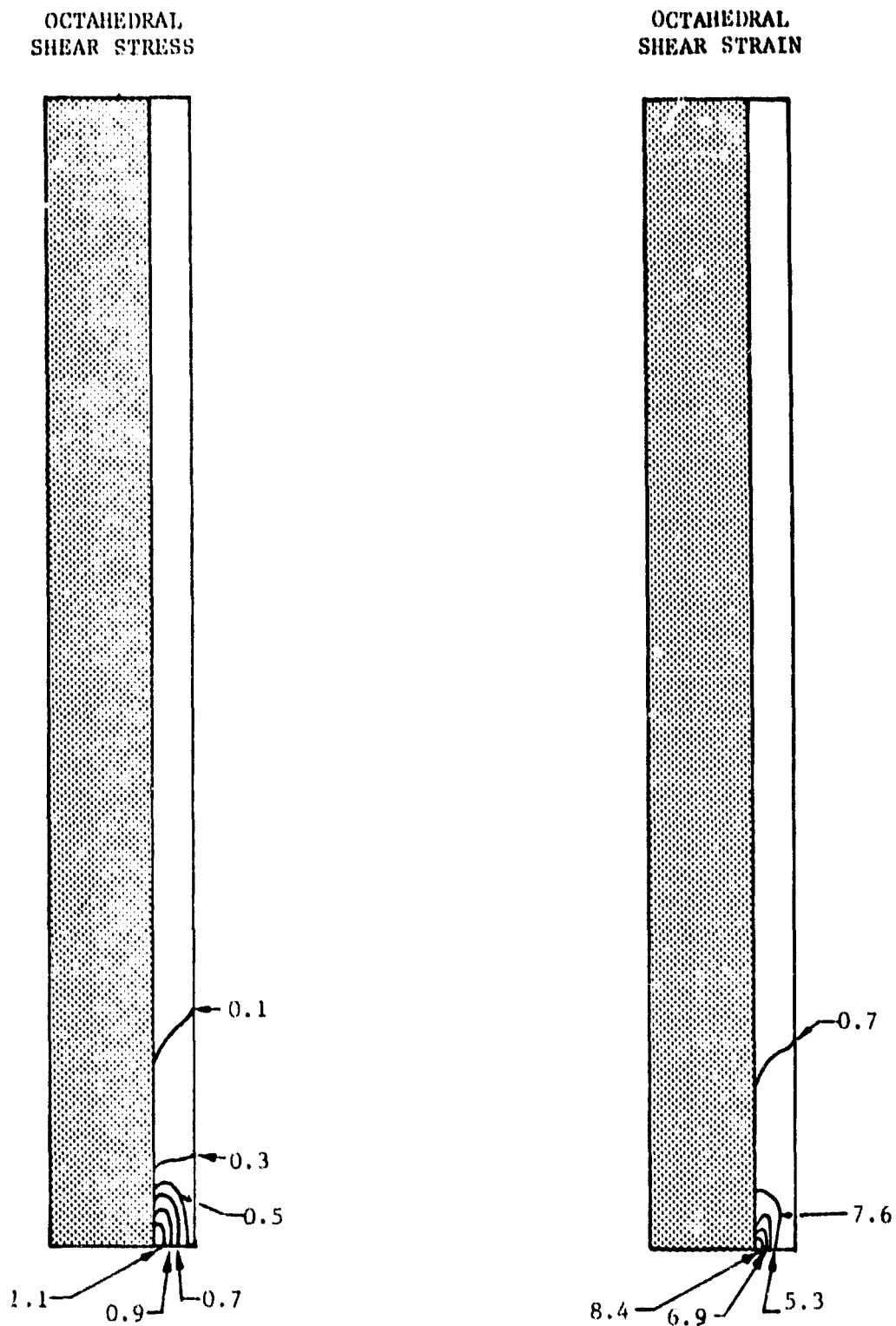


FIGURE 66. Contours of Constant Octahedral Shear Stress (Normalized by Dividing by the Matrix Yield Value of 17 ksi) and Octahedral Shear Strain, Minimum Fiber Spacing Model ( $r_f/r_m = 0.714$ ), Average Applied Stress,  $\bar{\sigma}_z = 17.4$  ksi.

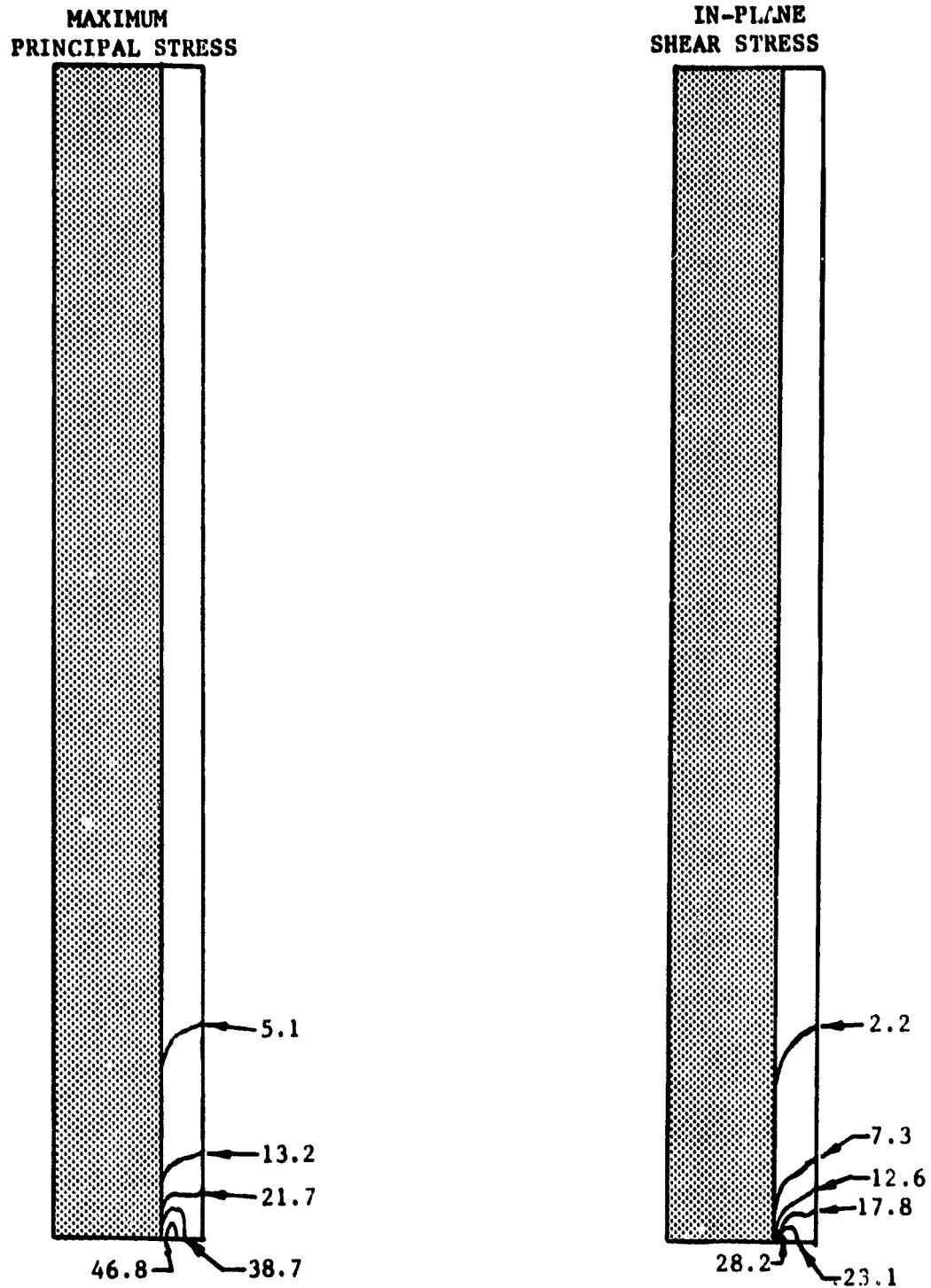


FIGURE 67. Contours of Constant Maximum Principal Stress and In-Plane Shear Stress, Minimum Fiber Spacing Model ( $r_f/r_m = 0.714$ ), Average Applied Stress,  $\bar{\sigma}_z = 17.4$  ksi.

the average stress is applied to the entire circular cross section, there is an immediate stress concentration at the  $z = 0$  plane (see Figure 13) due to an appreciable reduction in net cross-sectional area caused by the fiber discontinuity. This, and the presence of the penny-shaped crack, also a result of the fiber discontinuity, caused initial plastic deformation at the crack tip at an average applied stress of only 7 ksi. Continued loading resulted in a first failure in the matrix at an applied stress of 17.4 ksi. Failure of the first element triggered the failure of three additional elements along the  $z = 0$  boundary, the plane of the fiber discontinuity. This resulted in a further reduction of net section at the  $z = 0$  boundary, and a subsequent adjustment increment caused the crack to grow radially to the edge of the model, representing total failure and thus terminating the analysis. The contour plots of Figures 66 and 67 represent the state of octahedral shear stress and strain in this model just prior to crack initiation.

In the case of the axial loading of the maximum fiber spacing model ( $r_f/r_m = 0.424$ ), plastic deformation at the crack tip did not occur until an average applied stress of 13 ksi had been reached. Continued loading resulted in a first failure, or crack initiation, at a stress level of 32.3 ksi. As was the case with the minimum thickness model, the crack immediately grew through the region of plastic deformation, and the resulting reduction in the net section area of the model caused total failure. The contours of constant octahedral shear stress and strain for the maximum fiber spacing model just prior to crack initiation are presented in Figures 68 and 69.

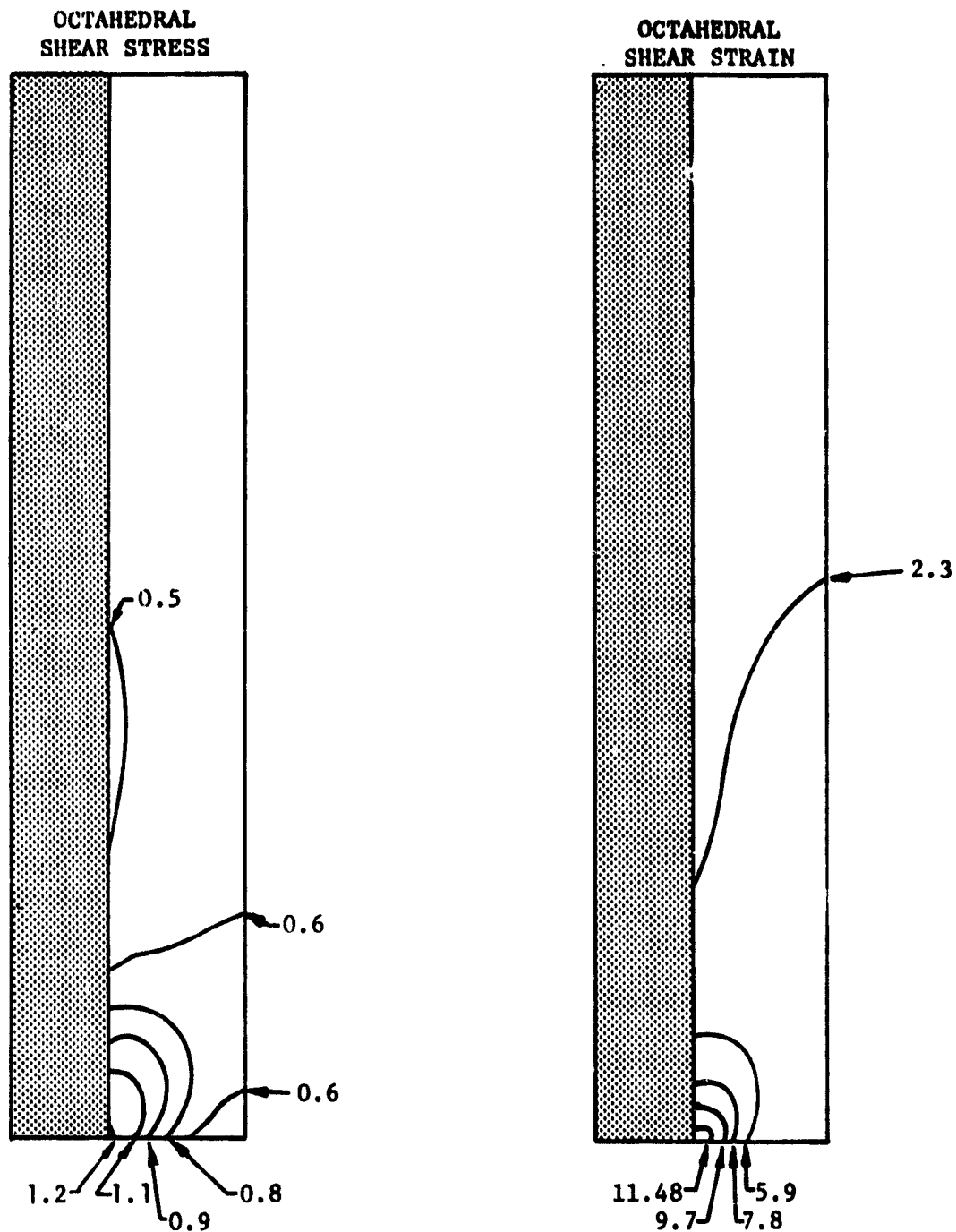


FIGURE 68. Contours of Constant Octahedral Shear Stress (Normalized by Dividing by the Matrix Yield Value of 17 ksi) and Octahedral Shear Strain, Maximum Fiber Spacing Model ( $r_f/r_m = 0.424$ ), Average Applied Stress,  $\bar{\sigma}_z = 32$  ksi.



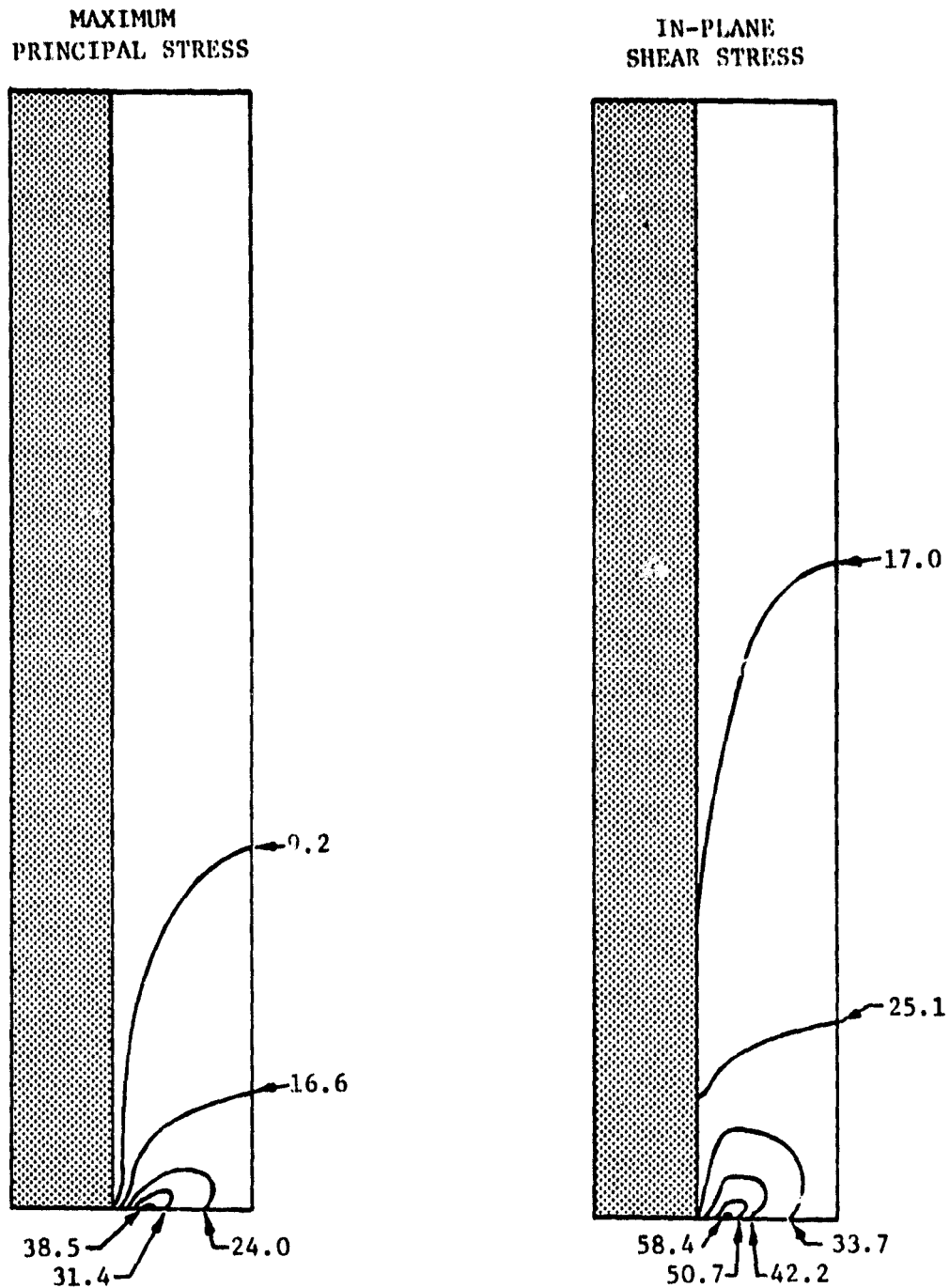


FIGURE 69. Contours of Constant Maximum Principal Stress and In-Plane Shear Stress, Maximum Fiber Spacing Model ( $r_f/r_m = 0.424$ ), Average Applied Stress,  $\bar{\sigma}_z = 32$  ksi.

For the thickest model run ( $r_f/r_m = 0.330$ ), plastic deformation was first observed at an average applied stress of 15 ksi. Initial crack formation occurred at an average applied stress of 37.2 ksi; the contour plots of stress and strain just prior to this crack initiation are presented in Figures 70 and 71. It will be noted that the region of plastic deformation around the crack tip involves more than a third of the matrix thickness, as was the case for the two models discussed above. As in the previous cases, this relatively low fiber volume model representation also suffered catastrophic failure once the crack had been initiated.

To provide further insight to the response of the axisymmetric model, the displacement of the broken fiber ends relative to each other has been plotted in Figure 72 as a function of the average applied stress level for the three model configurations discussed above. This plot clearly illustrates the variation in overall stiffness and load carrying capacity of the model as a function of matrix thickness. Experimental measurements could readily be made using test specimens of these configurations, and results compared with those shown in Figure 72.

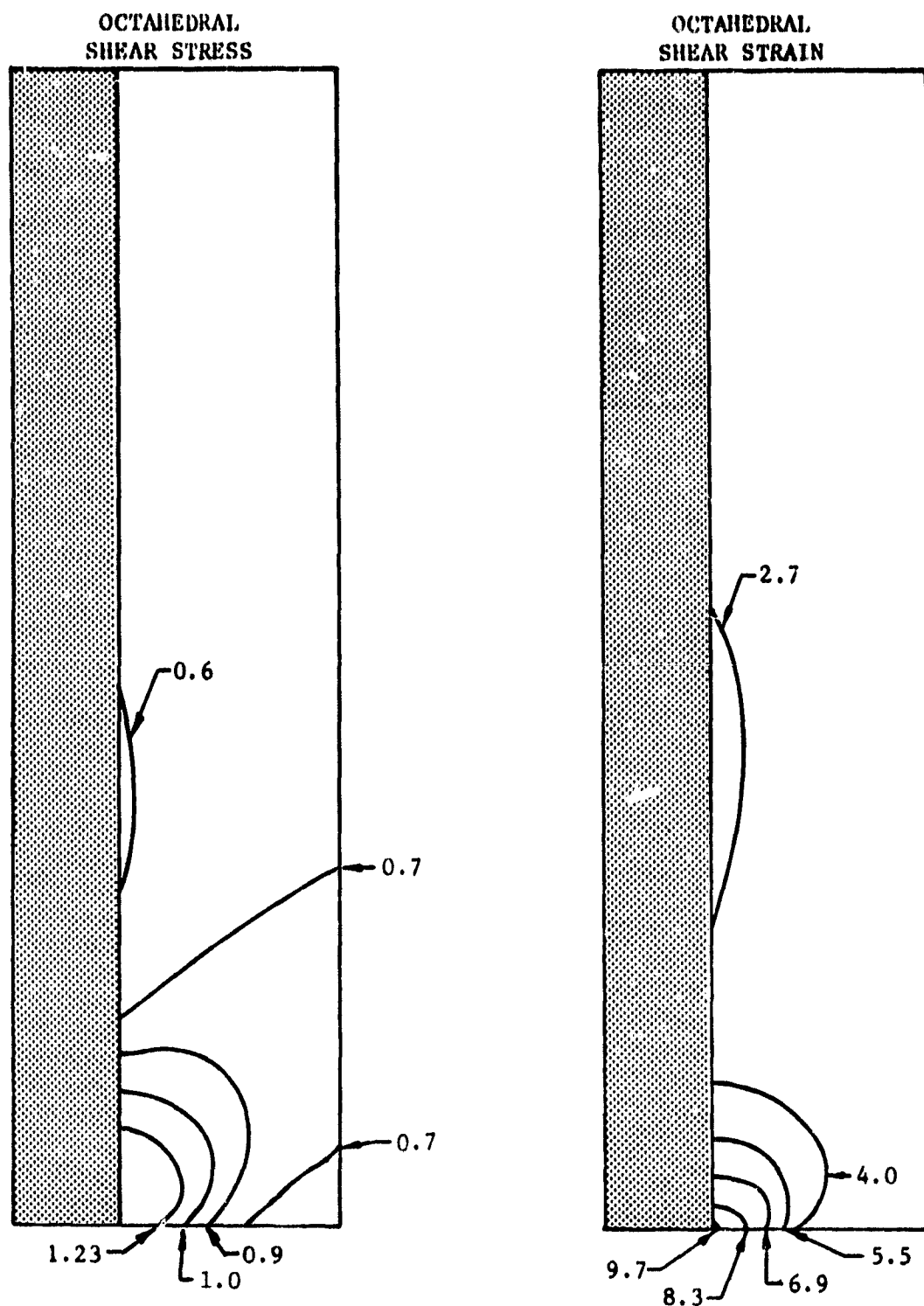


FIGURE 70. Contours of Constant Octahedral Shear Stress (Normalized by Dividing by the Matrix Yield Value of 17 ksi) and Octahedral Shear Strain,  $1\frac{1}{2}$  Maximum Fiber Spacing Model ( $r_f/r_m = 0.330$ ), Average Applied Stress,  $\bar{\sigma}_z = 37.2$  ksi.

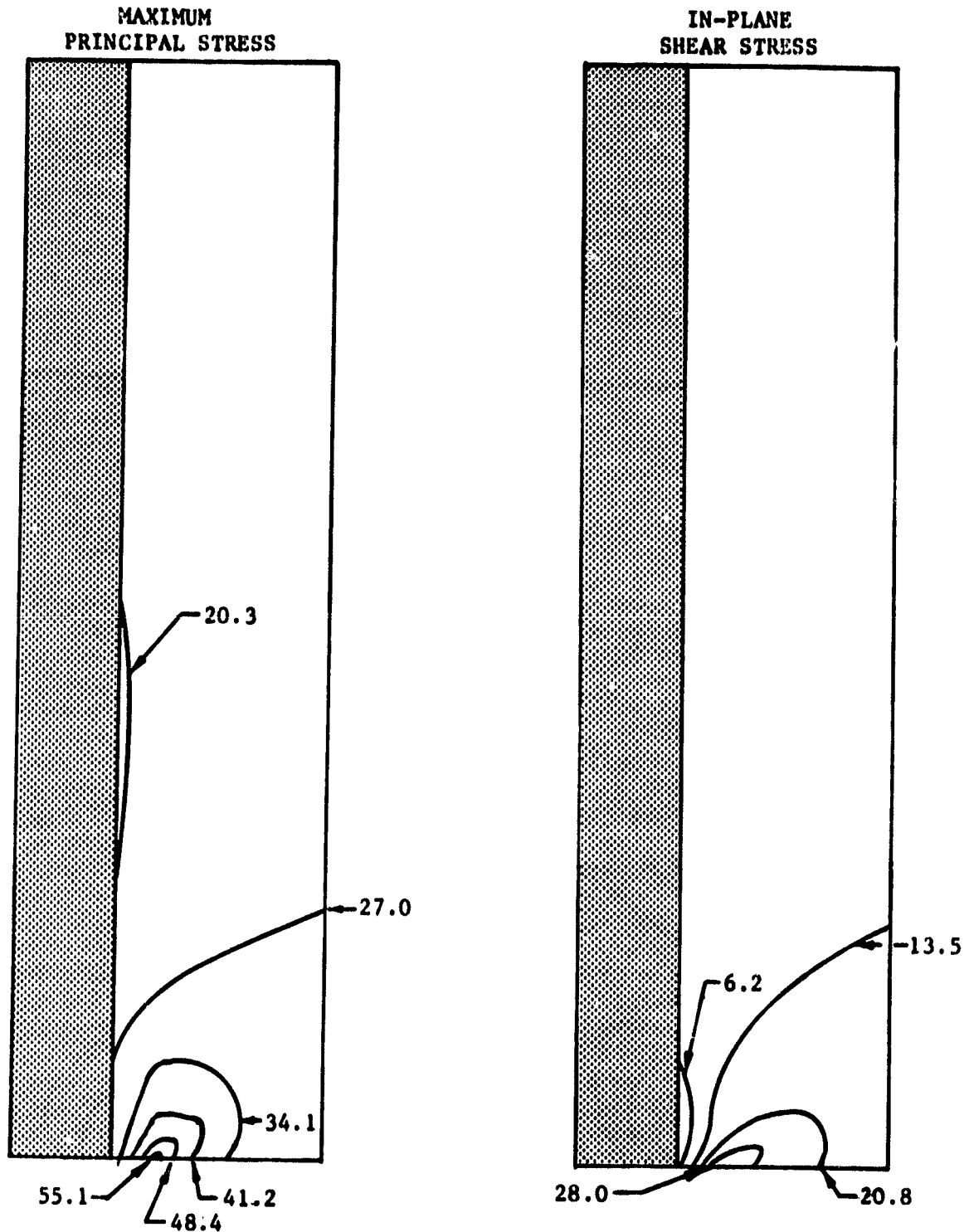


FIGURE 71. Contours of Constant Maximum Principal Stress and In-Plane Shear Stress,  $1\frac{1}{2}$  Maximum Fiber Spacing Model ( $r_f/r_m = 0.330$ ), Average Applied Stress,  $\bar{\sigma}_z = 37.2$  ksi.

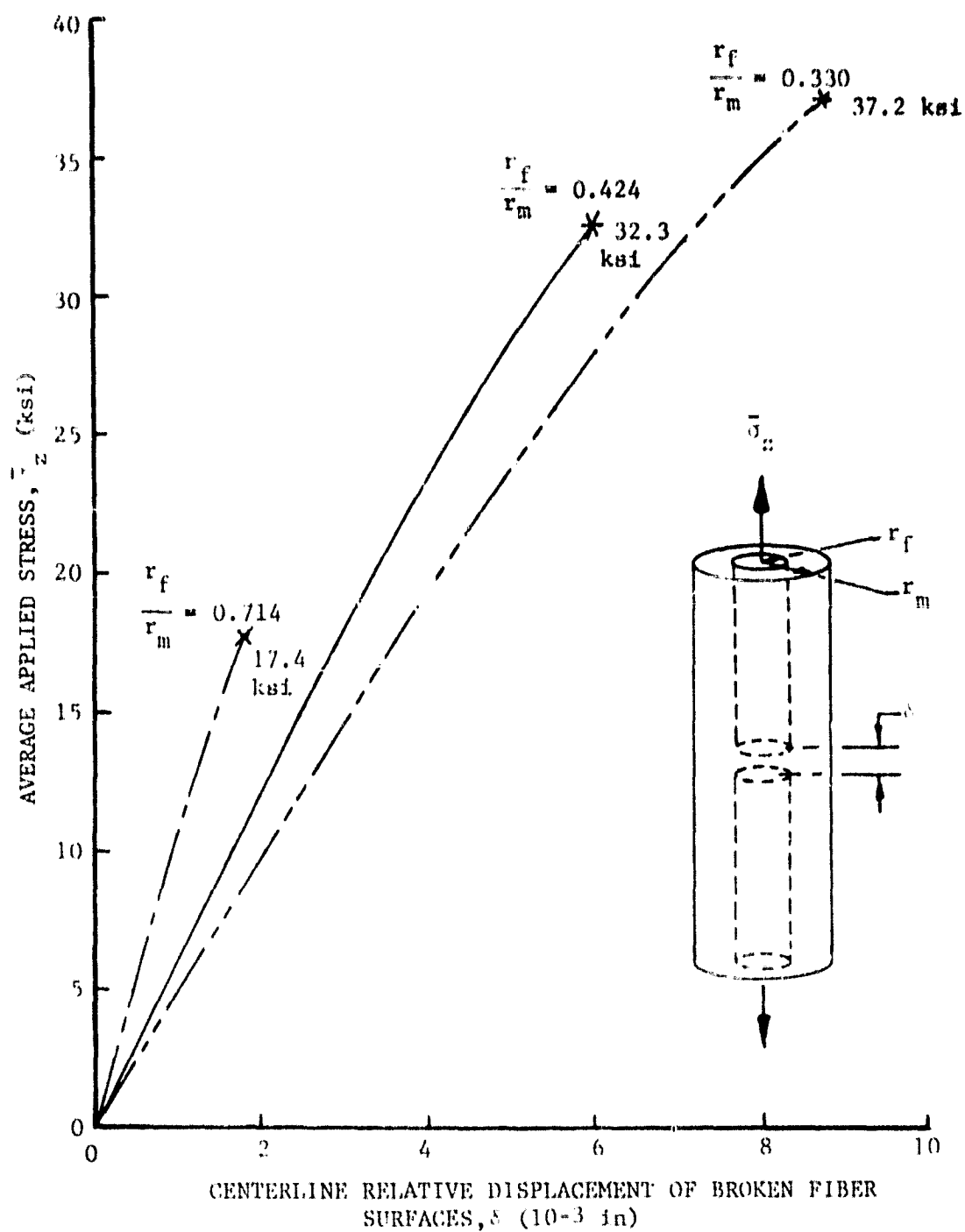


FIGURE 72. Plot of Broken Fiber Surface Displacement versus Applied Stress, Axisymmetric Model.

**SECTION 7**

**CONCLUSIONS AND FUTURE WORK**

At the end of the second year of this continuing investigation for NASA-Lewis, the analytical tools required to perform the title study are now well in hand. Although improvements can, and will, still be made in both the generalized plane strain and axisymmetric analyses and related computer programs, they are presently fully operational. In addition, the three-dimensional finite element analysis, although developed as part of another program [7], has also just become operational. This analysis will also be fully available to the present NASA-Lewis study, as required. Obviously, analysis methods have advanced significantly during the past two years.

The numerical examples presented in this report are intended to demonstrate the capabilities of the analyses, and to provide at least a preliminary indication of the influence of a broken fiber on local stress states, and overall performance of the composite.

To date, only pre-existing fiber breaks have been modeled. It will be relatively straightforward to extend this to the analysis of composites having weak sites distributed arbitrarily along the fibers. The numbers and severity of these weak sites can be established from available experimental data for boron fibers. This will lead to the study of interactions between closely spaced fiber breaks occurring under an applied stress.

In terms of maximizing energy absorption during plastic deformation and subsequent crack propagation, it is anticipated that a detailed study using the generalized plane strain analysis will lead to guidelines for designing boron/aluminum composites with controlled defects fabricated

into the material. This will result in trade-offs between composite stiffness and ultimate strength, and energy absorption during the fracture process. The three-dimensional analysis can be used to confirm the adequacy of the (two-dimensional) generalized plane strain analysis in performing these studies.

Experimental verification of the analytical work already completed, and to be undertaken during the next year, is also required. The axisymmetric analysis was developed primarily with this in mind. It will be relatively simple to fabricate single-fiber composites, i.e., single boron fibers surrounded by a uniform annular sheath of aluminum matrix material. Either a break can then be induced in the fiber before mechanical testing, or fibers known to have statistically weak sites can be used. When these single fiber composites are loaded in axial tension, the change in the gap between ends of the fiber break can be experimentally monitored (using X-rays, an extensometer, etc.). As indicated in Figure 72, these changes are predicted to be relatively large, on the order of 0.002" to 0.010" at failure.

It was noted in Section 6.6 that crack initiation in the single fiber axisymmetric models lead to immediate catastrophic failure of the single-fiber composite. This was in contrast to the results presented in Section 6.4 for the axially loaded, longitudinal section models using the generalized plane strain analysis. There, the many surrounding unbroken fibers were able to absorb the energy released by the crack formation. Both analyses are presently set up to hold a constant average applied stress during the crack propagation and subsequent adjustment increments. Based upon the results of Section 6.6, it would be better to perform the

single-fiber composite experiments under displacement control rather than load control. Then, when plastic deformation, crack initiation, and subsequent crack propagation occurs, the average applied stress will drop, allowing the crack to be arrested. Crack opening displacement measurements can then be made before an additional increment of composite displacement is applied.

Addition of a constant displacement loading scheme to the existing axisymmetric analysis will involve some modifications of the computer program.

In conclusion, analysis methods are now well-established. Use of these analytical tools in performing detailed parametric studies remains to be completed. In conjunction with these analytical studies, experimental verification also remains as an important task.



## REFERENCES

1. D.P. Murphy and D.F. Adams, "Energy Absorption Mechanisms During Crack Propagation in Metal Matrix Composites," Report UWME-DR-901-103-1, Department of Mechanical Engineering, University of Wyoming, October 1979.
2. A.K. Miller and D.F. Adams, "Micromechanical Aspects of the Environmental Behavior of Composite Materials," Report UWME-DR-701-111-1, Department of Mechanical Engineering, University of Wyoming, January 1977.
3. A.K. Miller and D.F. Adams, "Inelastic Finite Element Analysis of a Heterogeneous Medium Exhibiting Temperature and Moisture Dependent Material Properties," Fibre Science and Technology, Volume 13, 1980, pp. 135-153.
4. D.F. Adams, "High-Performance Composite Materials for Vehicle Construction: An Elastoplastic Analysis of Crack Propagation in a Unidirectional Composite," Report R-1070-PR, The Rand Corporation, Santa Monica, California, March 1973.
5. T. Repnau and D.F. Adams, "High-Performance Composite Materials for Vehicle Construction: A Finite Element Computer Program for the Elastoplastic Analysis of Crack Propagation in a Unidirectional Composite," Report R-1392-PR, The Rand Corporation, Santa Monica, California, October 1973.
6. D.F. Adams, "Elastoplastic Crack Propagation in a Transversely Loaded Unidirectional Composite," Journal of Composite Materials, Vol. 8, January 1974, pp. 38-54.
7. M.M. Monib and D.F. Adams, "Three-Dimensional Elastoplastic Finite Element Analysis of Laminated Composites," Report UWME-DR-001-102-1, Department of Mechanical Engineering, University of Wyoming, November 1980.
8. D.F. Adams, "Inelastic Analysis of a Unidirectional Composite Subjected to Transverse Normal Loading," Report RM-6245-PR, The Rand Corporation, Santa Monica, California, May 1970.
9. D.F. Adams, "Inelastic Analysis of a Unidirectional Composite Subjected to Transverse Normal Loading," Journal of Composite Materials, Vol. 4, July 1970, pp. 310-328.
10. T.R. Branca, "Creep of a Unidirectional Metal Matrix Composite Subjected to Axial and Normal Lateral Loads," TAM Report 341, Department of Theoretical and Applied Mechanics, University of Illinois, Urbana, Illinois, June 1971.
11. R.D. Cook, Concepts and Applications of Finite Element Analysis, John Wiley and Sons, Inc., New York, 1974.

12. O.E. Zienkiewicz, The Finite Element Method in Engineering Science, 3rd Edition, McGraw Hill, London, 1977.
13. R.M. Richard and J.R. Blacklock, "Finite Element Analysis of Inelastic Structures," AIAA Journal, Vol. 7, No. 3, March 1969, pp. 432-438.
14. Military Handbook 5A, "Metallic Materials and Elements for Aerospace Vehicle Structures," Department of Defense, Washington, D.C., 1966.
15. J.A. DiCarlo, "Mechanical and Physical Properties of Modern Boron Fibers," NASA Technical Memorandum NASA TM-73882, April 1978.
16. J. Awerbuch and H.T. Hahn, "Crack Tip Damage and Fracture Toughness of Boron/Aluminum Composites," Journal of Composite Materials, Vol. 13, April 1979, pp. 82-107.
17. C.R. Wyle, Advanced Engineering Mathematics, McGraw-Hill Book Company, New York, 1951.

## APPENDIX A

### EVALUATION OF INTEGRAL COEFFICIENTS

#### FOR THE GENERALIZED AXISYMMETRIC ELEMENT STIFFNESS MATRIX

In Section 4.2.2, it was shown that a critical step in forming the exact element stiffness matrix for a toroidal finite element of triangular cross section is the integration of the product of the strain-displacement relationships and the constitutive relationships over the volume of the element, as described by Eq. (20). This operation led to the six integral relationships given in Eq. (24). In this appendix, a procedure for evaluating the three integrals having  $\frac{1}{r}$  terms in their integrands is presented. The three integrals to be evaluated are repeated here, i.e.,

$$\begin{aligned} I &= \int_r \int_z \frac{1}{r} \, dr dz \\ I_5 &= \int_r \int_z \frac{z}{r} \, dr dz \\ I_6 &= \int_r \int_z \frac{z^2}{r} \, dr dz \end{aligned} \tag{A-1}$$

In Figure A-1, a planar section of the element is shown for reference to geometrical considerations in evaluating Equations (A-1).

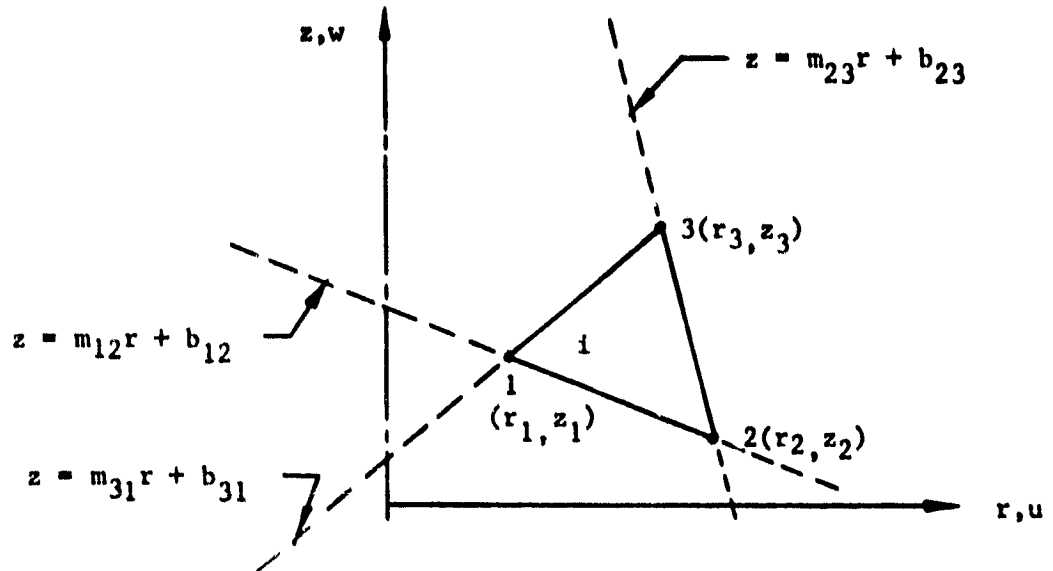


FIGURE A-1. Geometric Definition of the Triangular Element in the  $r$ - $z$  Plane.

As Figure A-1 indicates, the triangle,  $i$ , is defined by the lines bounding its sides, i.e.,  $L_{12}$ ,  $L_{23}$ , and  $L_{31}$ , each of which is described by the equation shown. For example, line  $L_{23}$  is expressed as

$$z = m_{23}r + b_{23} \quad (\text{A-2})$$

where  $m_{23}$  is the slope of  $L_{23}$  and  $b_{23}$  is its  $z$ -intercept, defined as

$$m_{23} = \frac{\Delta z}{\Delta r} = \frac{z_3 - z_2}{r_3 - r_2}$$

$$b_{23} = \frac{(z_2 r_3 - z_3 r_2)}{(r_3 - r_2)} \quad (\text{A-3})$$

The equations for the other two lines and their coefficients can be obtained by a cyclic permutation of the indices of Eqs. (A-2) and (A-3), i.e.,  $1 \rightarrow 2 \rightarrow 3 \rightarrow 1$ . Equations (A-1) can be directly integrated with respect to  $z$  to yield

$$\begin{aligned} I_4 &= \int_r \frac{z}{r} dr \\ I_5 &= \int_r \frac{z^2}{2r} dr \\ I_6 &= \int_r \frac{z^3}{3r} dr \end{aligned} \quad (A-4)$$

Equations (A-2) are substituted into Eqs. (A-4) to give

$$\begin{aligned} I_4 &= \int_{r_1}^{r_3} \frac{1}{r} (m_{31}r + b_{31}) dr + \int_{r_3}^{r_2} \frac{1}{r} (m_{23}r + b_{23}) dr + \int_{r_2}^{r_1} \frac{1}{r} (m_{12}r + b_{12}) dr \\ I_5 &= \int_{r_1}^{r_3} \frac{1}{2r} (m_{31}r + b_{31})^2 dr + \int_{r_3}^{r_2} \frac{1}{2r} (m_{23}r + b_{23})^2 dr + \int_{r_2}^{r_1} \frac{1}{2r} (m_{12}r + b_{12})^2 dr \quad (A-5) \\ I_6 &= \int_{r_1}^{r_3} \frac{1}{3r} (m_{31}r + b_{31})^3 dr + \int_{r_3}^{r_2} \frac{1}{3r} (m_{23}r + b_{23})^3 dr + \int_{r_2}^{r_1} \frac{1}{3r} (m_{12}r + b_{12})^3 dr \end{aligned}$$

Equations (A-5) can now be expanded and integrated term-by-term with respect to  $r$  fairly easily. The details of this operation are, however, quite lengthy, and the results only are presented below. In each case, only the first term is shown, the second two terms being obtained by a cyclic permutation of the indices, as described in Section 4.2.2.

$$I_4 = \sum \frac{1}{c} (b_{12} - b_{31}) \ln r_1 + (m_{12} - m_{31})$$

$$I_5 = \sum \frac{1}{c} \frac{1}{2} (b_{12}^2 - b_{31}^2) \ln r_1 + (m_{12} b_{12} - m_{31} b_{31}) r_1 + \frac{1}{4} (m_{12}^2 - m_{31}^2) r_1^2 \quad (A-6)$$

$$I_6 = \sum \frac{1}{c} \frac{1}{3} (b_{12}^3 - b_{31}^3) \ln r_1 + (m_{12} b_{12}^2 - m_{31} b_{31}^2) r_1 + \frac{1}{2} (m_{12}^2 b_{12} - m_{31}^2 b_{31}) r_1^2 \\ + \frac{1}{9} (m_{12}^3 - m_{31}^3) r_1^3 +$$

The expressions for  $I_4$ ,  $I_5$ ,  $I_6$  derived above are valid for the most general triangular geometries, i.e., when  $r_1$ ,  $r_2$ , and  $r_3$  are distinct and not equal to zero. For certain orientations of the element, Eqs. (A-6) are not valid; these orientations are described and dealt with in Appendix B.

By substituting the expressions for the slopes and  $z$ -intercepts of the various triangle sides into Eqs. (A-6), then collecting and rearranging terms somewhat, the expressions in Eqs. (26) through (28) are obtained.

However, it was found that computer programming of these integrals is easier and more direct when they are left in the form shown above. This is especially true when logical decisions regarding special element geometry are programmed.

## APPENDIX B

### NUMERICAL DIFFICULTIES WITH SPECIAL GEOMETRICAL CONFIGURATIONS OF THE AXISYMMETRIC ELEMENT

The expression for the six integrals required for a full axisymmetric element stiffness matrix, as given in Eqs. (25) through (28), are valid for the most general geometries, i.e., when  $r_1$ ,  $r_2$ , and  $r_3$  are distinct and nonzero. However, there are three situations which require special treatment. These are:

- When one of the node points of the triangle lies on the axis of rotation, i.e.,  $r = 0$ .
- When any two of the node point radii of the triangle are equal but nonzero.
- When any two node point radii are zero.

Each of these three cases are dealt with in the subsections that follow.

#### B.1. One Node Point Radius Equal to Zero

In examining the expressions for  $I_4$ ,  $I_5$ , and  $I_6$  (Section 4.2.2 or Appendix A), it can be seen that logarithmic terms are involved. When a node point is located on the axis of rotation, its corresponding logarithmic term becomes infinite. However, by examining the logarithmic term of interest and its coefficient, which consists of the  $z$ -intercept terms of the two lines converging on the node point in question, it is obvious that the intercept for both of these lines is the same. In other words, the limit of the logarithmic term and its coefficient can be shown to exist by an application of L'Hospital's rule [17], and this limit is



always equal to zero. Accordingly, whenever the argument of a logarithmic term is equal to zero, the term and its coefficient are simply deleted.

### B.2. Two Node Point Radii Equal but Nonzero

When two nodal radii of an element are equal, the element side between them is parallel to the axis of rotation, and the expressions for  $m_{ij}$  and  $b_{ij}$ , the slope and z-intercept of that side, become infinite. For example, if  $r_2 = r_3$ , an examination of Eqs. (A-3) quickly confirm the problem. This singularity is easily removed by considering the form of the integrals in Eqs. (A-5), in which the integrations with respect to  $r$  have yet to be performed. Note that the integrals involving  $m_{23}$  and  $b_{23}$ , the terms in question, also have limits of  $r_2$  and  $r_3$ . Thus, the integral is identically equal to zero and these terms can be omitted. In the implementation of the formulas given by Eqs. (A-6), this objective is accomplished by defining the  $m$  and  $b$  terms of element sides parallel to the  $z$ -axis to be zero, i.e.,

$$\begin{aligned} \text{For } r_i &= r_j, \\ m_{ij} &= b_{ij} = 0 \end{aligned} \tag{B-1}$$

### B.3. Two Node Point Radii Equal to Zero

When two of the element node points, say Node 1 and Node 3, lie on the axis of rotation, as indicated in Figure B-1, we observe

$$\begin{aligned} r_1 &= r_3 = 0 \\ \xi_1 &= \xi_3 = 0 \\ u_1 &= u_3 = 0 \end{aligned} \tag{B-2}$$

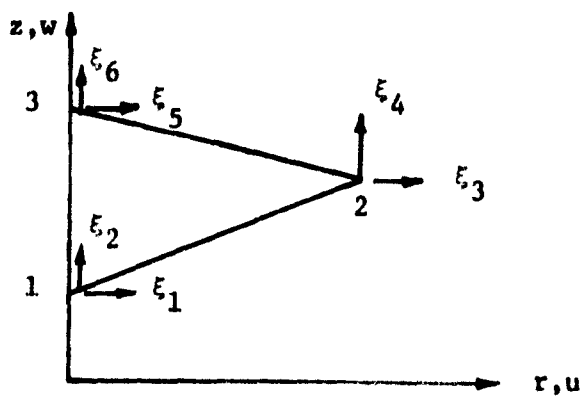


FIGURE B-1. Element Node Point Identification.

When the above relations are substitute into Eq. (13) we have

$$\left\{ \begin{array}{c} u_1 = 0 \\ w_1 \\ u_2 \\ w_2 \\ u_3 = 0 \\ w_3 \end{array} \right\} = \left[ \begin{array}{cccccc} 1 & 0 & z_1 & 0 & 0 & 0 \\ 0 & 0 & 0 & 1 & 0 & z_1 \\ 1 & r_2 & z_2 & 0 & 0 & 0 \\ 0 & 0 & 0 & 1 & r_2 & z_2 \\ 1 & 0 & z_3 & 0 & 0 & 0 \\ 0 & 0 & 0 & 1 & 0 & z_3 \end{array} \right] \left\{ \begin{array}{c} 0 \\ \epsilon_2 \\ 0 \\ \epsilon_4 \\ \epsilon_5 \\ \epsilon_6 \end{array} \right\} \quad (\text{B-3})$$

or

$$\{\delta\}_1 = [T_{00}]\{\epsilon\}_1 \quad (\text{B-4})$$

and the assumed displacement field takes the form

$$\begin{aligned} u &= \epsilon_2 r \\ w &= \epsilon_4 + \epsilon_5 r + \epsilon_6 z \end{aligned} \quad (B-5)$$

Applying the strain-displacement relationships of Eqs. (3) yields

$$\begin{Bmatrix} \epsilon_{rr} \\ \epsilon_{zz} \\ \gamma_{rz} \\ \epsilon_{\theta\theta} \end{Bmatrix} = \begin{bmatrix} 0 & 1 & 0 & 0 & 0 & 0 \\ 0 & 0 & 0 & 0 & 0 & 1 \\ 0 & 0 & 0 & 0 & 1 & 0 \\ 0 & 1 & 0 & 0 & 0 & 0 \end{bmatrix} \begin{Bmatrix} 0 \\ \epsilon_2 \\ 0 \\ \epsilon_4 \\ \epsilon_5 \\ \epsilon_6 \end{Bmatrix} \quad (B-6)$$

or

$$\{\epsilon\}_1 = [C_{00}]\{\xi\}_1$$

where  $[C_{00}]$  is the shape matrix for an element with two node points whose radii are zero. By substituting this shape matrix into Eq. (21) and performing the indicated multiplication and integration, we obtain the element stiffness matrix for this geometry. In the case of an elastic, isotropic material, we have

$$(\bar{k}_{00})_1 = \frac{2\pi E}{(1+\nu)(1-2\nu)} \begin{bmatrix} 0 & 0 & 0 & 0 & 0 & 0 \\ & 2I_1 & 0 & 0 & 0 & 2\nu I_1 \\ & & 0 & 0 & 0 & 0 \\ & & & 0 & 0 & 0 \\ \text{SYNCRATIC} & & & & (\frac{1}{2}-\nu)I_1 & 0 \\ & & & & & (1-\nu)I_1 \end{bmatrix} \quad (B-7)$$

Similarly, for a transversely isotropic material in the elastic range,

$$(\bar{k}_{oo})_1 = \frac{2\pi E}{Q} \begin{bmatrix} 0 & 0 & 0 & 0 & 0 & 0 \\ 0 & 2(1-T+F)I_1 & 0 & 0 & 0 & (1+T+F)I_1 \\ 0 & 0 & 0 & 0 & 0 & 0 \\ 0 & 0 & 0 & 0 & 0 & 0 \\ 0 & 0 & 0 & 0 & 0 & 0 \\ 0 & (1+T+F)I_1 & 0 & 0 & 0 & 0 \\ \text{SYMMETRIC} & & & & & \end{bmatrix} \quad (B-8)$$

where the quantities  $Q$ ,  $T$ , and  $F$  are as defined in Eq. (29). For an isotropic material in the plastic range we have, for two nodal radii equal to zero,

$$(\bar{k}_{oo})_1 = \left(\frac{2\pi E}{1+\nu}\right) \begin{bmatrix} 0 & 0 & 0 & 0 & 0 & 0 \\ 0 & (4A - \frac{2s_{11}s_{11} + s_{11}^2 + s_{22}^2}{B})I_1 & 0 & 0 & 0 & (A+A' - \frac{s_{11}s_{12} + s_{22}s_{11}}{B})I_1 \\ 0 & 0 & 0 & 0 & 0 & 0 \\ 0 & 0 & 0 & 0 & 0 & 0 \\ 0 & 0 & 0 & 0 & 0 & 0 \\ 0 & (A+A' - \frac{s_{11}s_{12} + s_{22}s_{11}}{B})I_1 & 0 & 0 & 0 & 0 \\ \text{SYMMETRIC} & & & & & \end{bmatrix} \quad (B-9)$$

Where  $A$ ,  $A'$ , and  $B$  are defined in Eq. (30).

The special form of the strain-displacement matrix, as given in Eq. (B-6), also requires that the back substitution matrices for each type of material response be re-derived. These are presented below.

For an isotropic material in the elastic range we have,

$$[\bar{B}_{oo}]_1 = \frac{E}{(1+\nu)(1-2\nu)} \begin{bmatrix} 0 & 1 & 0 & 0 & 0 & \nu \\ 0 & 2\nu & 0 & 0 & 0 & (1-\nu) \\ 0 & 0 & 0 & 0 & (\frac{1-2\nu}{2}) & 0 \\ 0 & \nu & 0 & 0 & 0 & \nu \end{bmatrix} \quad (B-10)$$

For the elastic, transversely isotropic case,

$$[\bar{B}_{oo}]_1 = \frac{E}{Q} \begin{bmatrix} 0 & (1-T+F) & 0 & 0 & 0 & (\nu+T) \\ 0 & (\nu+T+F) & 0 & 0 & 0 & (1-T) \\ 0 & 0 & 0 & 0 & \frac{Q}{2(1+\nu)} & 0 \\ 0 & (1-T+F) & 0 & 0 & 0 & F \end{bmatrix} \quad (B-11)$$

where T, F, and Q are as defined in Eq. (29).

For an isotropic material in the plastic range,

$$[\bar{B}_{oo}]_1 = \frac{E}{1+\nu} \begin{bmatrix} 0 & 2A - (\frac{S_{11}^2 + S_{11}S_{33}}{B}) & 0 & 0 & \frac{-S_{11}S_{12}}{B} & A' - \frac{S_{11}S_{22}}{B} \\ 0 & A+A' - (\frac{S_{11}S_{22} + S_{22}S_{33}}{B}) & 0 & 0 & \frac{-S_{22}S_{12}}{B} & A - \frac{S_{22}^2}{B} \\ 0 & -\frac{S_{11}S_{12} - S_{12}S_{33}}{B} & 0 & 0 & (\frac{1}{2} - \frac{S_{12}^2}{B}) & -\frac{S_{22}S_{12}}{B} \\ 0 & 2A - (\frac{S_{11}S_{33} + S_{33}^2}{B}) & 0 & 0 & -\frac{S_{33}S_{12}}{B} & A - \frac{S_{22}S_{33}}{B} \end{bmatrix} \quad (B-12)$$

with A, A', B, and  $S_{ij}$  having the same definitions as presented in Eq. (30).

## APPENDIX C

### LOAD APPLICATION IN THE DISPLACEMENT FORMULATION OF THE FINITE ELEMENT ANALYSIS

A detailed description of the axisymmetric analysis was presented in Section 4. The generalized plane strain analysis was included in the first-year report [1]. Details of the computer programming were presented in Appendix A of that report. Of particular interest, however, is the method of load application.

The present finite element analyses are displacement formulations, which is ideal in terms of accounting for the symmetry boundary conditions associated with the periodic arrays assumed. However, this presents a difficulty in terms of load application, since it is desired to be able to specify applied stress increments rather than applied displacement increments. In early works [4-6,8,9] this problem was handled by solving a series of displacement boundary value problems for each increment, one displacement boundary value problem for each component of loading increment to be applied, viz,  $\bar{\sigma}_x$ ,  $\bar{\sigma}_y$ ,  $\bar{\sigma}_z$ ,  $\Delta T$ ,  $\Delta M$ . These individual solutions were then scaled as required and superimposed to obtain the actual solution for the increment. Since it is the matrix inversion associated with the solution of each boundary value problem which consumes most of the computer time, doing this a number of times within each increment was very inefficient.

Using a method introduced by Branca [10], it is possible to solve for any combination of mechanical ( $\bar{\sigma}_x$ ,  $\bar{\sigma}_y$ ,  $\bar{\sigma}_z$ ) and hygrothermal ( $\Delta T$ ,  $\Delta M$ ) loadings in one step. This technique was incorporated into the basic micromechanics analysis when it was first formulated by Miller and Adams [2].

It continues to be used in the present program versions described in this report, having been refined and improved a number of times. A brief description of this "Branca" technique, as used in the present program, will be included here, for reference.

The application of mechanical tractions to the finite element model is considerably simplified by taking advantage of the rearrangement of the global stiffness matrix  $[K]$ , and the total force vector,  $\{F\}$ , using the method of Branca [10]. The displacement boundary conditions for the repeating unit finite element model were specified in order to maintain continuity of the material continuum while satisfying symmetry requirements. Specifically, referring for example to Figure 6, displacements in the x-direction of node points along the right-hand vertical boundary must be uniform. Likewise, displacements in the y-direction of the upper horizontal boundary must be uniform, and the displacements of all node points in the z-axis direction must be uniform (the generalized plane strain condition). When the overall force-displacement equation of the system is considered, i.e.,

$$\{F\} = [K] \{\delta\} \quad (C-1)$$

one can see that all of the boundary node points involved in mechanical loading will have identical displacements with respect to the direction of the load application. These identical displacements allow combining of certain terms in the global stiffness matrix that result in the replacement of the applied forces on boundary nodes by zeroes, in the manner described by Branca [10]. Successive modification of the global stiffness matrix for each boundary node point displacement results in the following form of Eq. (C-1) for the simultaneous application of uniform values of

$\sigma_x$ ,  $\sigma_y$ , and  $\sigma_z$  for an array of  $n$  nodal points

$$\begin{Bmatrix} 0 \\ 0 \\ 0 \\ \cdot \\ \cdot \\ \cdot \\ \bar{F}_x \\ \bar{F}_y \\ \bar{F}_z \end{Bmatrix} = \begin{bmatrix} k_{11} & k_{12} & k_{13} & \dots & k_{1(2n+1)} \\ & k_{22} & k_{23} & \dots & \\ & & k_{33} & & \\ & & & - & \\ & & & & - \\ & & & & & - \\ & & & & & & - \\ & & & & & & & - \\ \text{symmetric} & & & & & & & & - \end{bmatrix} \begin{Bmatrix} \delta_1 \\ \delta_2 \\ \delta_3 \\ \cdot \\ \cdot \\ \cdot \\ \delta_{2n-1} \\ \delta_{2n} \\ \delta_{2n+1} \end{Bmatrix} \quad (C-2)$$

where  $\bar{F}_x$ ,  $\bar{F}_y$ , and  $\bar{F}_z$  are the total applied loads in the  $x$ ,  $y$ , and  $z$  directions, and are defined, for a unit thickness model, as

$$\begin{aligned} \bar{F}_x &= \sigma_x b \\ \bar{F}_y &= \sigma_y a \\ \bar{F}_z &= \sigma_z ab \end{aligned} \quad (C-3)$$

where  $a$  and  $b$  are the lengths of the region of analysis (e.g., Figure 6) in the  $x$  and  $y$  directions, respectively. Modification of the global stiffness matrix is accomplished by summing the stiffness coefficients of unknown but equal boundary displacements throughout the system of equations. This results in a set of three equations, representing the forces along the three moving boundaries of the model, which are placed in the last three



columns of the global stiffness matrix, outside of the bandwidth of a normal stiffness matrix. Another summation is now performed on the coefficients in these three equations corresponding to equation numbers representing loaded boundary nodes. These coefficients are all added to the terms in the last three rows of the three outside columns, which now represent the total applied loads in the x, y, and z directions. The system of linear, simultaneous equations that results from this process involves a stiffness matrix that is no longer symmetric, and whose bandwidth has been violated. To further complicate matters, the banded portion of this stiffness matrix must be stored in rectangular form, as described by Zienkiewicz [12], to minimize the core storage requirements of the system of equations. The coefficients for the summation of force equations are stored along side the rectangularized, upper triangular portion of the stiffness matrix.

This system of equations is solved using a highly specialized form of Gaussian elimination in which the stiffness matrix and the load vector must be further modified. This solution technique requires a great deal more bookkeeping than is the case for more conventional applications of the Gaussian elimination technique. The important advantage of this procedure, however, is that it allows the simultaneous application of external tractions in all three coordinate directions, and the application of thermal or moisture loads in a single step.